The influence of water percolation on flow of light non aqueous phase liquids in soil

The influence of water percolation on flow of light non aqueous phase liquids in soil

Annemieke Marsman

Abstract

Marsman, A., 2002, **The influence of water percolation on flow of light non aqueous phase liquids in soil**, Doctoral Thesis, Wageningen University, Wageningen, The Netherlands.

In this thesis the physical behavior of Light Non-Aqueous Phase Liquids (LNAPL) at the capillary fringe, is studied with multiphase flow models. Phenomena like a fluctuating water table or percolation of (infiltration) water have a large impact on this behavior. Both the geometry and the mobility of the LNAPL lens are affected. These two physical phenomena mentioned imply downwards and upwards water flow through the LNAPL lens. Different techniques were used in this investigation. Numerical calculations show that fluctuations of the phreatic groundwater level result in retardation of the horizontal migration of the LNAPL lens over the groundwater level. An expression is derived which quantifies the part of the simulated time during which the LNAPL can actually flow. This expression is implemented in an existing analytical solution that describes horizontal LNAPL migration, to enable that the effect of a fluctuating water level can be calculated analytically. Laboratory experiments are performed which verify these results. The effect of water flow through an LNAPL lens also affects the mobility of LNAPL. Numerical results show that both for upwards and for downwards water invasion of a lens, the mobility of the LNAPL has increased significantly. To obtain more qualitative insight on the pore scale, percolation theory is used. Percolation theory is applied to this problem and the appropriate series of drainage and imbibition processes are calculated to simulate the water percolation. The accompanying relative permeabilities show that the mobility increases after water percolation. Qualitative insight on the pore scale shows that the LNAPL is displaced to a larger amount of pore radii which advances the mobility of the LNAPL. This observation is in agreement with the numerical results.

Keywords: multi-phase flow, entrapment, numerical modeling, similarity solution, horizontal migration, percolation theory, relative permeability.

Contents

Chapter 1

General introduction

1.1 Background

During the previous century, soil in the Netherlands has become increasingly polluted by NAPL's through uncareful use of the soil and through ignorance. NAPL's (Non-Aqueous Phase Liquids) are organic fluids that are only slightly miscible with water. As a comprehensive term they may be referred to as 'oil'. These organic fluids form a serious threat to e.g. our drinking water supplies. To prevent health risks for humans and damage to nature, the contaminated soils should be remediated. To illustrate the hazards of this type of contamination: one liter of oil can significantly affect the quality of 100.000 liters of water, i.e. because of health reasons this water cannot be used as drinking water for humans.

Two types of oil can be distinguished: oil that is less denser than water and that will accumulate on the groundwater level. This type of oil is called LNAPL, where the 'L' stands for 'lighter' than water. The other type of oil is denser than water so that it may percolate much deeper into the soil layers through the groundwater. This type of oil is called DNAPL, where the 'D' stands for 'denser' than water. New techniques were developed to clean up these types of contamination, where the soil is not excavated to clean it up. A few examples of such of in-situ techniques are: 1. pump and treat: contaminated groundwater is pumped out of the soil, cleaned and possibly returned into the soil 2. air sparging: injection of air into the saturated zone, which both may enhance microbial degradation and removes volatile contaminants in the flowing gas phase. 3. steam injection: steam decreases the viscosity of oil contamination and therefore increases the mobility so that pump and treat will be more efficient, furthermore, the interfacial tension can decrease and oil volatilization increases, which

will enhance the efficiency of air sparging. At this moment many in-situ techniques are available. For an overview we refer to Hamby [12] who gave a well readable account about these techniques.

Until now, the knowledge about the physical behavior of NAPL's as a free phase in soil is very limited. The simple situation, where oil floats above a static water level, has been explored during the last decades and we are now capable of understanding and modeling this situation quite well. In reality, however, the water balances change as a function of time due to: seasonal changes, intermittent pumping or heavy rainfall. Such changes have a large impact on the behavior of NAPL. Both the geometry of a NAPL plume as its distribution in the pores is affected. An oil contaminant can be entrapped by water. This means that droplets of oil become surrounded by water which renders the oil as a liquid to be immobile. Whereas the mobile fraction of the oil may be removed by classical pumping approaches, this is not possible for the remaining entrapped oil. Otherwise these droplets can still form a threat to the environment by dissolution in the groundwater and by vaporization. If oil has become entrapped, it may be removed by pumping up groundwater, because it will contain dissolved oil. However, both dissolution rates and solubility of oil are usually such, that this way of removing entrapped oil is slow, inefficient and costly. Hence, either alternative in-situ remediation approaches or methods for the reduction of oil entrapment are needed. In both cases, a good anticipation of the entrapment mechanisms and the quantities of oil involved are essential. The objective in this thesis is to obtain more insight in oil entrapment and specifically, the effects that physical conditions have on the quantity of entrapped oil.

1.2 Problem description

This thesis is focussed on one type of oil contamination: LNAPL. If LNAPL is spilled at the ground surface, it will flow into the unsaturated zone and, after which, due to gravitational and capillary forces, it will accumulate in the form of a lens above the groundwater table, under reserve that the oil release is sufficiently large to reach the groundwater table (see Figure 1.1).

When a fluid or gas enters a porous medium, it depends on the interfacial tension, which pores and which part of these pores will be entered by this fluid/gas. We can distinguish different behavior for different soil types and fluid/gas types, which are classified by the so called wettability of the
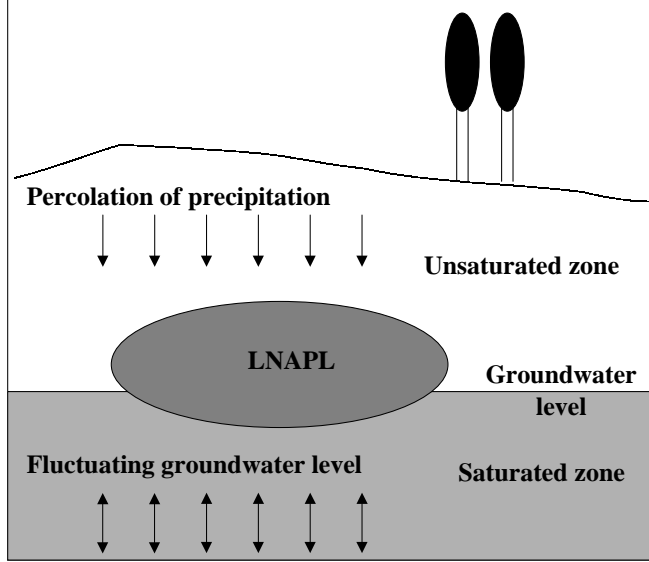
Figure 1.1: The multiphase system that is considered. The arrows represent main water flow directions.

phases. Wettability describes the preferential spreading of one fluid over solid surfaces in a two-fluid system. Whereas the wetting fluid will tend to coat the surface of grains and occupy smaller pores in porous media, the nonwetting fluid will tend to be restricted to the largest pores. We assume that this affinity of the three phases in our problem (water, oil and gas) to enter in soil pores of the porous medium decreases in the following order: water is the wetting phase, oil is the intermediate wetting phase and gas is the non-wetting phase. Because of the assumption that oil is the non-wetting phase compared to the water phase, oil will enter the largest pores and water will coat the surface of the grains. Consequently, the oil lens will spread above the groundwater table until it loses its mobility and the oil becomes entrapped into the water phase i.e. blobs of oil are enclosed by water.

The multiphase flow process, where water, oil and gas flow through the soil, is affected by oil entrapment and the physical conditions affecting entrapment. These conditions can be for example a fluctuating groundwater level caused by seasonal changes or pumping. Also the percolation of infiltrating water through an oil lens affects entrapment. For instance, Lenhard

et al. [28], Van Geel and Sykes [48], Kaluarachchi and Parker [18] and Pantazidou and Sitar [33] already showed the large impact of a fluctuating water level on the behavior of LNAPL: both the geometry and the amount of oil entrapment are affected. We focus on these physical conditions to understand their effects on the entrapment of oil into the water phase. A fluctuating groundwater level and percolating water can be interpreted by water infiltrating into the oil lens from two opposite sides. This is shown in Figure 1.1, where the situation is represented in a schematic way. The saturated zone consists of water filled pores. The unsaturated zone consist of water and gas. The LNAPL lens consists of oil, water and gas, where the LNAPL saturation is so large that the LNAPL is mobile. The groundwater level is represented as a sudden transition between the saturated and unsaturated zone. In reality, the saturated zone consist of a zone below the groundwater level and of a capillary fringe (which also consists of pores filled with water) that is formed above the water phase through capillary forces. The oil will float on the capillary fringe. The arrows in Figure 1.1 represent water invasion, either upwards as a fluctuating groundwater level, or downwards as percolation of precipitation. Infiltrating water will entrap the oil phase into the water phase in the form of isolated blobs. In case of a fluctuating groundwater level, water periodically invades and leaves the oil lens. A similar process holds for the percolation of precipitation: water enters the upper surface and flows through the subsurface until the oil lens is reached. Water invades the oil lens, oil becomes entrapped in the water phase and subsequently due to gravitational forces water leaves the oil lens. The questions that arise for these two types of water infiltration are:

- How does the mobility of the LNAPL change during the water infiltration?

- What happens when the water leaves the oil lens?

- What happens to the geometry of the lens?

In this thesis, we use different techniques to find an answer to these questions. A numerical model, an analytical solution in the form of the similarity solution, an analytical solution in the form of percolation theory and a laboratory experiment will be used to obtain more insight into this problem. In the next sections, these techniques will be introduced briefly.

1.3   Numerical model

To analyze the above described situations, multi-phase flow models are necessary. Petroleum reservoir codes to simulate the flow of water, oil and gas were already developed over 30 years ago. These codes can be used for environmental problems as well. Multiphase flow models for oil reservoirs, where water and oil flow simultaneously, have been investigated thoroughly. In the unsaturated zone, however, the gas phase (air) should be taken into account, and this additional phase makes the flow processes much more complex. Abriola and Pinder [1] developed such a multiphase flow model, where hysteresis was ignored. Kaluarachchi and Parker [18] showed that disregarding hysteresis results in significant errors in predicted fluid distributions. Subsequently Lenhard and Parker [25], [26], [24], [30] and Parker and Lenhard [34], [35], [36] incorporated hysteretic constitutive relations. Although we model a three phase system including water, oil and air, we assume that air is so mobile that the air pressure is approximately constant. The flow equations for two phases (water and oil) describe the flow phenomena sufficiently since our main interest is the flow behavior of oil. Therefore, the air entrapment and the effect it has on the relative water and oil permeability are neglected. This assumption is incorporated in the so called Richard's equation. Furthermore, Kaluarachchi and Parker [18] derived a simplified model of fluid entrapment by restricting hysteresis to entrapment of oil by water.

White, Oostrom and Lenhard [51] [29] developed a code to predict environmental restoration studies: STOMP (Subsurface Transport Over Multiple Phases). This is a three-dimensional, three-phase, compositional engineering simulator for modeling contaminant migration and remediation technologies for the cleanup of subsurface sites contaminated with organic compounds. The code is based on the Richard's equation and on the constitutive relations developed by Lenhard and Parker. The initial version of the code included the hysteretic relations developed by Lenhard and Parker [25] and later they included the simplified model for fluid entrapment developed by Kaluarachchi and Parker [18]. Flow and transport are solved numerically using an integrated-volume finite-difference scheme to discretize the governing equations. A comparison was made with experimental results by Lenhard et al [29] to verify the numerical results. It appeared that there is a good agreement between measured and predicted fluid contents. The capillary pressure-saturation relationships can be chosen from different empirical relations. Throughout this research we use either the relationship

based on the Van Genuchten capillary pressure-saturation relationship [49] or the relationship based on the Brooks-Corey capillary pressure-saturation relationship [6]. The main difference between these two methods is the concept of entry pressure, that is restricted to the Brooks-Corey relationship.

We use STOMP to calculate the effects of water infiltration on LNAPL numerically. An advantage of numerical calculations is that relatively few assumptions have to be made and the problem is mathematically well defined so that all aspects of multiphase flow can be kept under consideration. Disadvantages are the sometimes large calculation times (depending on the type of computer) and the complexity of the model, which makes it difficult to obtain qualitative insight into the problem without thorough parameter variation analyses. Furthermore, in some cases, the numerical calculations do not converge to a solution, so that the problem can not be solved.

1.4   Similarity solution

Numerical computer simulations require a lot of computational efforts and are often too complex to comprehend the processes that lead to a particular result. Analytical solutions can be very useful to do the same calculations with minor efforts, to obtain insight into the accompanying processes and to verify the numerical calculations for more constrained situations. To our knowledge, no 2-D analytical solution for three phase flow in porous media including oil entrapment is available for the problem represented in Figure 1.1. Van Dijke and Van der Zee [44] developed an analytical solution for the situation of a static groundwater level. Oil lens distribution, where capillary forces and oil entrapment are included was found to behave in a self-similar way. This means that the spatial distributions of its properties at various moments of time can be obtained from one another by a similarity transformation (see for example Barenblatt [2] and Hulshof and Vazquez [17]). The similarity solution consists of one part that represents the similarity profile and of one part that represents the changes in the behavior of the solution in time.

Numerical solutions for one case at two moments in time are used to derive parameters for the analytical solution. The profile of this numerical solution is used to explore the similarity solution to a larger time scale and to various parameter values. Comparison with numerical calculations showed that this similarity solution provides a good estimation for oil redistribution, where oil entrapment is included. We manipulate the similarity

solution used by Van Dijke and Van der Zee [44] in such a way, that a fluctuating groundwater level (see Figure 1.1) can be incorporated.

The main advantages of this method are the simplified calculations and consequently the small computational effort. A disadvantage of this analytical solution is that numerical calculations are still necessary to derive parameters.

1.5 Percolation theory

To approach the infiltration problem in a qualitative way, percolation theory can be used to gain more qualitative insight on the pore scale. Broadbent and Hammersly first published in 1957 the mathematical concept of percolation theory. They associated the spread of a fluid in a porous medium with the flow of coffee in a percolator, which explains the name percolation process. The theory pertains to network models that consist of bonds and nodes. We focus solely on the bonds and we assume that the nodes are just zero-dimensional markers. The bonds of the network are either *occupied*, which means that the bond is open to flow, or the bonds are vacant, which means that they are closed to flow. Pore bonds are called connected if there is a path between them of occupied bonds, i.e. if a fluid enters the model, it will start at one pore at the boundary of the model and from there it can flow into pores that are connected to this occupied pore and so on: a path of occupied bonds will be formed. The collection of connected pores surrounded by vacant bonds, is called a cluster (see Figure 1.2).

The transition of a macroscopically disconnected structure, where there are only single occupied pores that are not connected to a cluster, to a connected structure is characterized by the percolation threshold. The percolation threshold is the concentration where for the first time a percolating cluster is formed.

Percolation theory in general is well reviewed by Stauffer et al. [41], Kirkpatrick [19], Sahimi [39] [38] and Heiba [13]. The first random percolation model for two-phase flow in porous media was suggested by Larson et al. [23][22]. Heiba [13][14][15] further developed these ideas and applied them to the calculation of relative permeabilities. Furthermore, Heiba distinguished between the fraction of the pores that is *allowed* to a phase, and the fraction that is actually occupied by this phase. This means that a pore bond is enterable for a fluid concerning the thickness of the pore bond
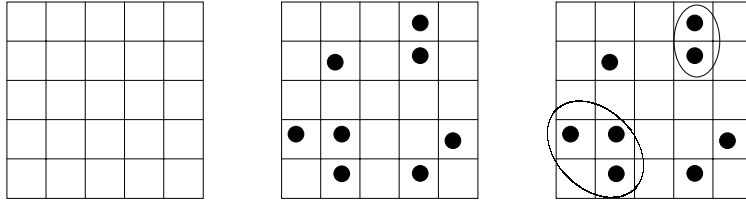
Figure 1.2: Definition of percolation and its clusters. The first figure shows parts of a square lattice, in the second figure some squares are occupied with big dots, in the last figure the 'clusters', groups of neighboring occupied squares, are encircled except when the 'cluster' consists of a single square.

and concerning the pressure of the fluid: this is called allowed. However, if a pore is not connected to a cluster containing this fluid, the pore bond will not be occupied by this fluid, even though it is allowed. This is called: the pore bond is not *accessible*. A three phase flow system was already proposed by Heiba [13] but limited to two specific cases where oil is always the shielding phase between water and gas.

We expand Heiba's ideas for three phase to a system which initially consists of water and gas. Oil will enter the system and a succession of drainage and imbibition processes will be imposed to obtain the complete range of compositions of a three phase system. Furthermore, we apply this theory to the mentioned water infiltration problem (Figure 1.1), to obtain more insight into the phenomena that take place during water infiltration into an oil lens.

One of the advantages of percolation theory is that it is a very straightforward method that uses a minor amount of computation time. Furthermore, it gives qualitative insight into the problem. Especially for this problem, where the quantitative phenomena are well known from numerical calculations while the physical meanings of the results are unknown, this theory gives a surplus value to the results. The assumption made that the sites of the network can be neglected so that the system consists of nodes solely, deviates from real soil. Moreover, percolation theory calculates average relative permeabilities and cannot be used as a quantitative tool.

1.6 Laboratory experiment

To verify theories that are developed for numerical and analytical purposes, it is very useful to perform an experiment in the laboratory. Experiments can establish whether the main phenomena have been accurately accounted for and whether the assumptions made are acceptable. In earlier work researchers performed experiments to investigate the behavior of LNAPL and to verify recently developed numerical codes. Lenhard et al. [27] used a one-dimensional column experiment to study a succession of drainage processes. They concluded that the model they developed [25], where hysteresis and fluid entrapment for three fluid phases are included, gives a good approach. Host-Madsen and Jensen [16] affirmed this approach by performing capillary pressure-saturation experiments. Eckberg and Sunada [8] performed an experiment where oil is introduced at the top of a vertical soil column containing water. The static fluid distribution was compared to the calculated distribution based on the Brooks-Corey [6] capillary pressure-saturation relations. They concluded that the water saturation at static conditions in a three-phase system was a function of the two-phase water-oil capillary pressure-saturation relation. Carey et al. [7] investigated the importance of hysteresis on the distribution of oil for a column that was infiltrated first by water, followed by oil and then water again. They concluded that the water infiltration could be modeled reasonably. The oil infiltration, however, resulted in less than satisfactory results because of the neglected hysteresis effects. Lenhard et al. [29] modeled a one-dimensional laboratory experiment in which oil infiltrates into a variably saturated sand column. Subsequently fluctuations of the water level are introduced. They clearly showed the importance of hysteresis in a dynamic multiphase flow system. Pantazidou and Citar [33] showed the same for a two-dimensional experiment with a fluctuating water table. Van Geel and Sykes [46] [47] [48] also performed a two-dimensional experiment where the water pressure at the base of the experimental box was increased and decreased to simulate fluctuating water table conditions. A comparison of their experimental data to the model results illustrates once more the effects and importance of fluid entrapment and saturation hysteresis.

In this thesis, we performed a two-dimensional experiment (see Figure 1.3) where oil floats above the capillary fringe. Fluctuations of the water level are incorporated and we quantify the retardation in horizontal migration. Disadvantages of a laboratory experiment are the restrictions in scale and time. The main advantage of such a laboratory experiment is
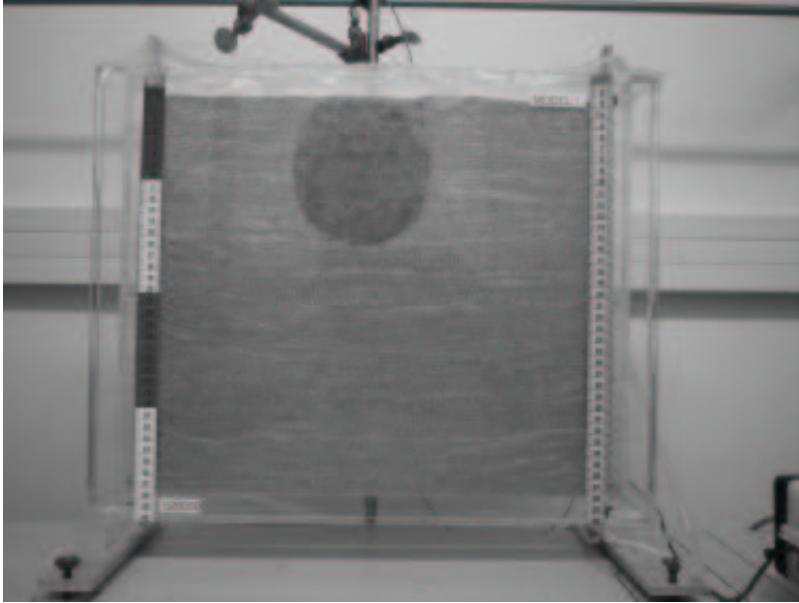
Figure 1.3: Set up of the 2-D laboratory experiment.

that no assumptions are made and all processes involved in a three phase
flow system will actually take place. Furthermore, an experiment can give
insight in the justification of assumptions and simplifications made in nu-
merical/analytical calculations.

1.7   Outline

In Chapter 2 of this thesis we investigate numerically the effects of rising
and lowering of the water level on oil entrapment and on the horizontal
oil spreading. We analyze the effects quantitatively and we developed an
equation for the effect on the geometry of the oil lens. This equation can
be incorporated into the similarity solution for oil lens redistribution to
account for a fluctuating groundwater level.

Chapter 3 describes a laboratory experiment where both the numerical
and the analytical (similarity solution) results obtained in Chapter 1 are
compared with the experiment.

In Chapter 4 we introduce percolation theory and we show how it can
be used for a three-phase system such as an LNAPL lens that floats at the

capillary fringe. Subsequently, we simulate a succession of imbibition and drainage processes to obtain the complete range of compositions of a three phase system.

In Chapter 5 we use percolation theory for a three phase system to obtain more qualitative insight into more complex processes that occur during water infiltration into an oil lens. The results are compared with numerical calculations.

Chapter 2

The effects of a fluctuating groundwater level on the spreading of LNAPL*

2.1   Introduction

Contamination of aquifers by hydrocarbons is a serious problem because the contaminants slowly infiltrate into the groundwater and adversely affect groundwater quality. We consider Light Non Aqueous Phase Liquids (LNAPL) that are less dense than water and accumulate as a lens above the phreatic surface. Knowledge of the geometrical distribution of LNAPL below the ground surface is essential to effectively remediate a contaminated site by pumping or to investigate the possibilities of biodegradation. Correspondingly, it is important to investigate the horizontal migration of the LNAPL lens and the quantity and location of entrapped LNAPL. Therefore we focus on the migration and the entrapped quantity. This is a multiphase flow problem that involves the three phases air, LNAPL and water. Henceforth we use the term oil as a comprehensive term for LNAPLs.

To model this flow problem Parker and Lenhard [34] and Lenhard and Parker [25] introduced saturation-pressure relationships which account for hysteresis and fluid entrapment in porous media containing up to three immiscible fluid phases. Later Lenhard et al. [30] and Kaluarachchi and Parker [18] derived a simplified model of fluid entrapment by restricting hysteresis to entrapment of oil by water. They found that their results were almost identical to the full model where hysteresis was also included. White, Oostrom and Lenhard [51] used the formulation of Lenhard et al. [25] for fluid entrapment to develop a three-dimensional, three-phase, com-

positional engineering simulator for modeling contaminant migration and remediation technologies. Later they also included the possibility to use the simplified model for fluid entrapment. We use this simulator for our calculations.

Additionally, approximate analytical solutions can be very helpful to reduce computation times and to verify numerical solutions. Van Dijke and Van der Zee [44] developed an analytical solution for oil lens redistribution by assuming that the oil lens is at vertical equilibrium and that water and oil flow are segregated. This reduces the multi-phase flow problem to a single equation for oil flow. Van Dijke and Van der Zee [44] compared this solution with a numerical model that accounts for the saturation-pressure relations from Parker and Lenhard [34] and the entrapment approximation from Kaluarachchi and Parker [18]. It appears that this analytical solution provides a good approximation of the free oil distribution.

We assume that an oil lens migrates through the unsaturated zone until it reaches the capillary fringe where it will spread laterally above the saturated zone. Most previous studies assume that the groundwater level is static, i.e., at a fixed level. However, in reality the location of the groundwater level and capillary fringe may vary as a function of time as a result of seasonal changes. The redistribution of the oil lens as a result of the groundwater level fluctuations may affect the migration process. Lenhard et al. [28] concluded from experiments with groundwater level fluctuations that oil and air were entrapped during water imbibition. Additionally, Van Geel and Sykes [48] experimentally and numerically showed the importance of fluid entrapment in a variably saturated medium during fluctuation of the groundwater level by comparison of the non-hysteretic and hysteretic model results and the experimental data. Kaluarachchi and Parker [18] concluded from numerical experiments that fluid entrapment remarkably reduces the horizontal migration since the trapped oil volume is immobile. Pantazidou and Sitar [33] showed experimentally that fluctuations of the phreatic surface result in trapping of oil below the groundwater level. These features will remarkably disturb the predictions of the dimensions of an oil lens and therefor the remediation. Until now the effect of fluctuations on the horizontal migration rate has not been investigated quantitatively.

In this work, we have investigated quantitatively the changes in the amount of oil entrapped in the water phase and the changes in horizontal migration caused by rising or lowering of the groundwater level. Furthermore we have investigated how these changes in entrapment and migration

are related to each other. For this purpose, we used the model developed by White, Oostrom and Lenhard [51]. In particular we considered the relation between the height of rising and lowering of the groundwater level and the changes in horizontal migration. The aim of this work is to expand the already known analytical solutions for oil redistribution above the groundwater level (Van Dijke and Van der Zee, [44]) to a more complex situation where the groundwater level fluctuates as a result of seasonal changes. The results of our numerical investigation were used to perform this adaptation.

2.2 Model

2.2.1 General equations

We consider a two-dimensional isotropic and homogeneous vertical cross-section of the soil. The basic equations that describe a three-phase model (water, oil and air) are the mass balance equations, Darcy's Law and the constitutive relations. We assume that air has such a high mobility that the air pressure is approximately constant and that the equations for two phases describe the flow sufficiently. And therefore, we will neglect air entrapment and the effect it has on the relative water and oil permeability. The mass balance equations for water and oil in a 2-D model are:

$$\phi\frac{\partial S_i}{\partial T} + \frac{\partial U_i}{\partial X} + \frac{\partial V_i}{\partial Z} = 0, \quad i = w, o \tag{2.1}$$

where the subscript i denotes either the water (w) or the oil (o) phase. S_i is the effective phase saturation, U_i and V_i are respectively the horizontal and vertical phase velocities. T is time and X and Z are respectively the horizontal and vertical coordinates, and ϕ is the porosity. The velocities follow from Darcy's Law, which is given by:

$$U_i = -\frac{Kk_{ri}}{\mu_i}\frac{\partial P_i}{\partial X} \tag{2.2}$$

$$V_i = -\frac{Kk_{ri}}{\mu_i}(\frac{\partial P_i}{\partial Z} + \rho_i g), \quad i = w, o \tag{2.3}$$

where K is the absolute permeability, k_{ri} is the relative phase permeability, and μ_i is the phase viscosity. P is the phase pressure, ρ_i is the phase density, and g the gravity acceleration. Combination of Equations (2.1), (2.2) and (2.3) yields the Richards equation:

$$\phi\frac{\partial S_i}{\partial T}\text{-}\frac{\partial}{\partial X}(\frac{Kk_{ri}}{\mu_i}\frac{\partial P_i}{\partial X})\text{-}\frac{\partial}{\partial Z}(\frac{Kk_{ri}}{\mu_i}\frac{\partial P_i}{\partial Z})\text{-}\rho_i g\frac{\partial}{\partial Z}(\frac{Kk_{ri}}{\mu_i}) = 0, \quad i = w, o \quad (2.4)$$

The constitutive relations are defined by Parker and Lenhard [34]:

$$
\begin{aligned}
S_w + S_o &= S_t \\
S_t + S_a &= 1 \\
S_w + S_{ot} &= S_{wa} \\
S_{of} + S_{ot} &= S_o \\
P_{ow} &= P_o\text{-}P_w \\
P_{ao} &= \text{-}P_o
\end{aligned}
$$

where S_t is the total liquid saturation and S_a is the air saturation. S_{wa} is the apparent water saturation, S_{ot} is the trapped oil saturation and S_{of} is the free oil saturation. P_{ow} is the oil-water capillary pressure and P_{ao} is the air-oil capillary pressure which is identical to $\text{-}P_o$ since we assume P_a to be zero.

To describe entrapment of oil, a linearized equation is used according to Kaluarachchi and Parker [18] that can be easily implemented in numerical multiphase flow codes:

$$S_{ot} = min[(\frac{1\text{-}S_w^{min}}{1 + F_L(1\text{-}S_w^{min})}\text{-}\frac{1\text{-}S_{wa}}{1 + F_L(1\text{-}S_{wa})}), S_o] \qquad (2.5)$$

$$F_L = \frac{1}{S_{or}^{max}}\text{-}1 \qquad (2.6)$$

where S_{ot} is the trapped oil saturation and S_w^{min} is the minimum water saturation. F_L is Land's factor, where S_{or}^{max} is the maximum residual oil saturation. Equation (2.5) prevents that the trapped oil saturation becomes larger than the oil saturation.

We use the dimensionless variables for the oil phase as defined by Van Dijke Van der Zee [44]:

$$z = \frac{\alpha\beta_{ow}Z}{1\text{-}D}, \quad x = \frac{(1\text{-}D)X}{V_1\alpha\beta_{ow}}, \quad t = \frac{K\rho_o g(1\text{-}D)T}{\mu_o V_1\alpha\beta_{ow}}, \quad p_o = \frac{\alpha\beta_{ow}P_o}{\rho_o g(1\text{-}D)} \quad (2.7)$$

i.e. the characteristic lengths and time are:

$$Z_c = \frac{1\text{-}D}{\alpha\beta_{ow}}, \quad X_c = \frac{V_1\alpha\beta_{ow}}{(1\text{-}D)}, \quad T_c = \frac{\mu_o V_1 \alpha\beta_{ow}}{K\rho_o g(1\text{-}D)}, \quad P_c = \frac{\rho_o g(1\text{-}D)}{\alpha\beta_{ow}} \quad (2.8)$$

where $D = \frac{\beta_{ow}\Delta\rho}{\beta_{ao}\rho_o}$ is an indication of the thickness of the lens and V_1 is the initial oil volume or oil surface since we consider a two-dimensional problem ($V_1 = \phi \int_{-\infty}^{\infty} \int_{0}^{\infty} S_o(X,Z)dXdZ$). Equation (2.4) expressed in dimensionless variables becomes :

$$\phi\frac{\partial S_o}{\partial t}\text{-}\frac{(1\text{-}D)^2}{V_1(\alpha\beta_{ow})^2}\frac{\partial}{\partial x}(k_{ro}\frac{\partial p_o}{\partial x})\text{-}\frac{V_1(\alpha\beta_{ow})^2}{(1\text{-}D)^2}\frac{\partial}{\partial z}k_{ro}(\frac{\partial p_o}{\partial z}+1) = 0 \quad (2.9)$$

2.2.2 Retention functions

Different retention functions that relate saturation and pressure have been developed. The most commonly used retention functions are those given by Van Genuchten [49] and by Brooks-Corey [6]. The function suggested by Van Genuchten assumes that the wetting fluid drains from a porous medium whenever the capillary pressure is greater than zero. The Brooks-Corey function, however, assumes that the wetting fluid does not drain until a critical capillary pressure, i.e. the non-wetting fluid entry pressure, is exceeded.

The retention function defined by Van Genuchten [49] and extended to three phases by Parker, Lenhard and Kuppusamy [36] is given by:

$$S_{wa} = \begin{cases} 1 & if\ P_w > 0\ and\ P_o < P_w \\ (1 + (\frac{\alpha\beta_{ow}}{\rho_w g}\,P_{ow})^n)^{\text{-}m} & if\ \begin{cases} 0 < P_w < P_o\ or \\ P_w < 0\ and\ P_o > \frac{1}{\beta_{ao}}P_w \end{cases} \\ (1 + (\frac{\text{-}\alpha}{\rho_w g}\,P_w)^n)^{\text{-}m} & if\ P_o < \frac{1}{\beta_{ao}}P_w < 0 \end{cases} \quad (2.10)$$

$$S_t = \begin{cases} 1 & if\ P_o > 0\ or\ P_w > 0 \\ (1 + (\frac{\alpha\beta_{ao}}{\rho_w g}\,P_{ao})^n)^{\text{-}m} & if\ \frac{1}{\beta_{ao}}P_w < P_o < 0 \\ S_{wa} & if\ P_o < \frac{1}{\beta_{ao}}P_w < 0 \end{cases} \quad (2.11)$$

where α and n are parameters, $m = 1 - \frac{1}{n}$, β_{ow} is the oil-water surface tension and β_{ao} is the air-oil surface tension. We use VG to denote the Van Genuchten equations. The Brooks-Corey retention function is given by:

$$S_{wa} = \begin{cases} 1 & if\ \beta_{ow}P_{ow} \le P_e\rho_w g \\ (\frac{\beta_{ow}P_{ow}}{P_e\rho_w g})^{-\lambda} & if\ \beta_{ow}P_{ow} > P_e\rho_w g \end{cases} \qquad (2.12)$$

and

$$S_t = \begin{cases} 1 & if\ \beta_{ao}P_{ao} \le P_e\rho_w g \\ (\frac{\beta_{ao}P_{ao}}{P_e\rho_w g})^{-\lambda} & if\ \beta_{ao}P_{ao} > P_e\rho_w g \end{cases} \qquad (2.13)$$

where P_e is the entry pressure for the capillary pressure and λ is a parameter. We use BC to denote the Brooks-Corey equations.

2.2.3   Entrapment

From previous studies (Lenhard, Oostrom and White [29] , Van Geel and Sykes [48], Kaluarachchi and Parker [18], Pantazidou and Sitar [33]), we know that rising and lowering of the groundwater level causes respectively entrapment of the oil in the water phase and mobilization of the oil phase. Kaluarachchi and Parker [18] noticed that oil entrapment caused by the fluctuating groundwater level markedly reduces the lateral migration. To investigate the influence of fluctuations on lateral migration in more detail, it is important to determine the amount of entrapped oil in the water phase quantitatively. It is logical to suspect that the amount of entrapped oil depends on the changes in the depth of the groundwater level. Therefore we relate the total change in depth of the fluctuating groundwater level during one fluctuation to the amount of entrapment. Figure 2.1 represents the domain with the situation that we are modeling, where we restrict the calculations to the right part of the domain for symmetry reasons. Since we have chosen to simulate the fluctuations by changing the water pressure at the bottom of the domain ($Z = 0$, see Figure 2.1) as a sinusoidal function, we will call the total change in depth of the fluctuating groundwater level the amplitude (A) of the fluctuation. The amplitude A together with the angular velocity of the sinusoidal function (ϖ) are the resolving parameters for the determination of the lateral migration.

We assume vertical hydrostatic pressure distributions:

$$\begin{align} P_o(X, Z, T) &= P_o(X, 0, T) - \rho_o g Z & (2.14) \\ P_w(X, Z, T) &= P_w(X, 0, T) - \rho_w g Z & (2.15) \\ P_{ow}(X, Z, T) &= \Delta\rho g Z + P_o(X, 0, T) - P_w(X, 0, T) & (2.16) \end{align}$$
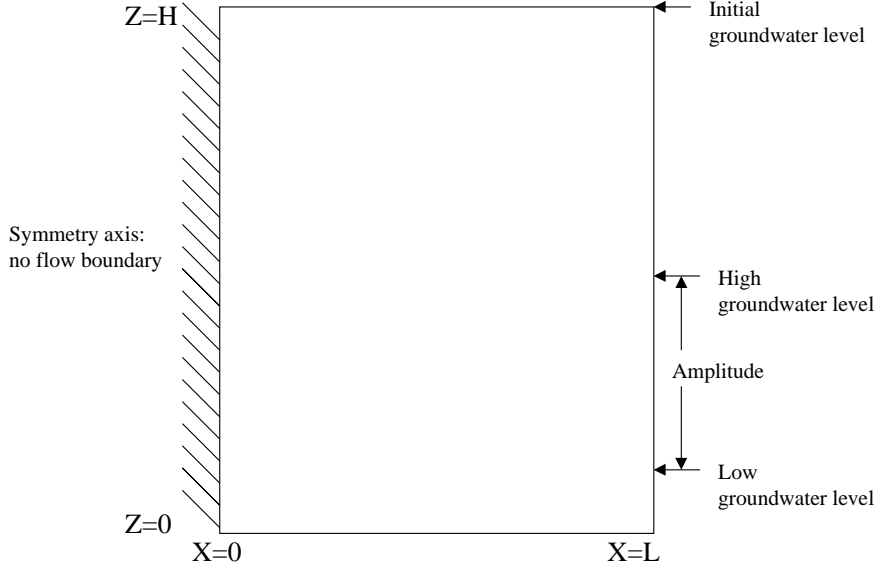
Figure 2.1: 2-D model with boundary conditions.

where $P_o(X, 0, T)$ and $P_w(X, 0, T)$ are respectively the oil pressure and the water pressure at the bottom of the domain where $Z = 0$. $\Delta \rho = \rho_w - \rho_o$. The fluctuations of the groundwater level are accomplished by imposing a time dependent function $P_w(X, 0, T)$ in the form of a sine function. To determine the change in $P_w(X, 0, T)$ for which the oil is completely entrapped in the water phase we relate the change in $P_w(X, 0, T)$ to the initial value for $P_o(X, 0, 0)$ by a factor f. We determine the depth where no mobile oil is present and where consequently the oil pressure is lower or equal to zero. Since the water level should reach this depth for complete entrapment the capillary pressure is negative. The conditions for complete entrapment of oil in the water phase are:

$$
\begin{align}
P_w(X, 0, T) &= P_o(X, 0, 0) \cdot f \tag{2.17} \\
P_o(X, Z, 0) &\leq 0 \tag{2.18} \\
P_{ow}(X, Z, 0) &\leq 0 \tag{2.19}
\end{align}
$$

Substitution in Equations (2.14) and (2.16) results in:

Property	Value
Air-water scaling factor β_{aw}	1.00
Air-NAPL scaling factor β_{ao}	2.25
NAPL-water scaling factor β_{ow}	1.80
Intrinsic permeability K	2.14×10^{-11} [m^2]
Porosity ϕ	0.4
NAPL density ρ	830 [kg/m^3]
NAPL viscosity μ	2.046×10^{-3} [Pa s]
Length of column	0.7 [m]

Table 2.1: Parameters used in the computations.

$$f \geq \frac{\rho_w}{\rho_o} \qquad (2.20)$$

for complete entrapment i.e.

$$P_w(X, 0, T) \geq \frac{\rho_w}{\rho_o} P_o(X, 0, 0) \qquad (2.21)$$

The accompanying water head is:

$$h_w = \frac{P_o(X, 0, 0)}{\rho_o g} \qquad (2.22)$$

We assume that the ratio between the chosen amplitude and this specific water head has a linear relation with the entrapped oil ratio ($A \sim \frac{S_{ot}}{S_o}$). With this relation it is possible to relate the relative quantity of entrapment and the amplitude of the fluctuating groundwater level:

$$\frac{S_{ot}}{S_o} = \begin{cases} \frac{A\rho_o g}{P_o(X,0,0)} & if \ A \leq \frac{P_o(X,0,0)}{\rho_o g} \\ 1 & if \ A > \frac{P_o(X,0,0)}{\rho_o g} \end{cases} \qquad (2.23)$$

Later we use Equation (2.23) to analyze the effects of A on the distribution of the oil lens.

## 2.3   Numerical methods

2.3.1   1-D

To simulate the infiltration and redistribution of the oil under fluctuating groundwater level conditions, we first perform a one-dimensional three-

phase numerical calculation and compare the results with experimental data. This experiment was performed by Lenhard et al. [29] in a homogeneous sand column and, since it is very similar to our fluctuating groundwater level problem, it is appropriate to use it for our purposes. The numerical model is based on the mixed form of the Richards Equation (2.4), where we consider X to be very small to simulate a one-dimensional model. The governing flow equations are solved numerically by following an integrated finite-difference method. Spatial discretization of the computational domain with the integrated finite-difference method is limited to orthogonal grid systems. The algebraic forms of the nonlinear governing equations are solved with a multivariable residual-based Newton-Raphson iteration technique. The parameter values that are used in this experiment are given in Table 2.1. We use an orthogonal Cartesian domain of height 0.7 m, discretized by 71 nodes, and of width 0.06 m, discretized by 1 nodal point. The initial time step is 10 s and the maximum allowable timestep is 10 min.

At the base ($Z = 0$) of the domain, a water pressure is prescribed that ascertains that the complete domain only contains water, i.e. the initial groundwater level is located at the upper boundary of the domain (0.70 m). The initial oil pressures are set equal to the water pressures, which is the critical oil pressure for water saturated conditions (White, Oostrom and Lenhard, [51]). The critical oil pressure in general is the pressure that agrees with the situation where no free oil is present, i.e. $S_{wa} = S_t$. Furthermore, the initial lowering of the groundwater level is simulated by a step-wise linearly declining Dirichlet boundary condition for aqueous pressure on the base of the domain so that a lower groundwater level is achieved of 0.07 m:

$$P_w(X, 0, T_i) = \max[(0.7\rho_w g \text{-} i \cdot 0.05\rho_w g), 0.07\rho_w g] \qquad (2.24)$$

In this equation for the water pressure the accompanying heads are the initial water head of 0.70 m, the lower groundwater level of 0.07 m and the decrease of the head in steps of 0.05 m. Infiltration of the oil into the domain from the top is modeled by a Neumann boundary condition on the upper surface by implementing a flux on the upper surface of the domain. Two fluctuations of the groundwater level are simulated by changes in the water pressure on the lower boundary surface. These fluctuations are modeled as linear changes in the water-pressure-head on the lower boundary surface. The first rise in the groundwater level elevation caused by these boundary conditions changed the water pressure head from 0.07 m to 42 cm at $T =$
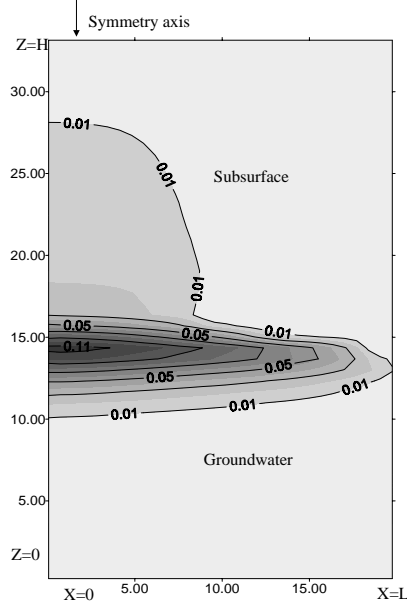
Figure 2.2: 2-D redistribution of an LNAPL lens above the groundwater level.

17.4 h from the start of the experiment until $T = 19.4$ h. The lowering changes the water pressure head from 0.42 m to 0.17 m (from $T = 19.4$ h until $T = 21.1$ h). The second rise in the groundwater level elevation changes the water pressure head from 0.17 m to 0.52 m (from $T = 21.1$ h until $T = 25$ h).

To investigate which retention function is suitable for our problem we compare this experiment in which the groundwater level was fluctuated with numerical simulation results based on either the BC or the VG function (see Section 2.2.2). Lenhard et al. compared their experimental data with a simulation based only on the VG retention function. They explained the main discrepancy between the simulated and measured data at the bottom of their model by pointing out that the BC relations which assume that wetting fluid will not drain until a critical capillary pressure, i.e. the entry pressure, is exceeded (Lenhard, Oostrom and White, [29]*)*.

2.3.2   2-D

We expand the one-dimensional fluctuating water level problem to a two-dimensional problem, namely a vertical cross-section of the soil. The oil
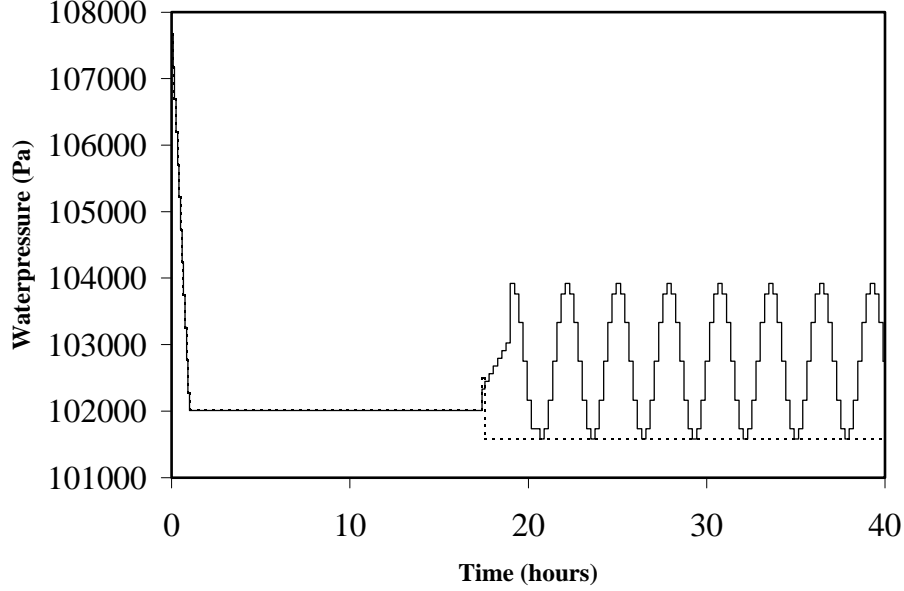
Figure 2.3: Water pressure at the bottom of the sandbox as a function of time, where the solid line represents the water pressure in the fluctuation case and the dashed line represents the water pressure in the reference case.

accumulates at the groundwater level in the form of a lens. Due to gravity and capillary forces, the oil lens spreads out further along the groundwater level with increasing time. This is shown in Figure 2.2. The distribution depends on water, oil and air pressures and the pore size distribution. At locations within the lens where the water saturation increases, part of the oil becomes entrapped as discrete drops become enclosed by water. Entrapment implies immobilized oil, hence it adversely influences the velocity of the horizontal migration of the lens.

The model parameters we used are the same as for the one-dimensional situation (see Table 2.1), except for the horizontal dimension that is chosen to be 2 m, discretized over 40 nodes. The initial conditions for this porous medium are as follows: we have a 2-D domain homogeneously filled with sand. At the bottom of the domain $(X, 0, T)$ a water pressure is imposed that ascertains that the complete domain is filled with water. This is shown in Figure 2.3 at $T = 0$ h. Hence the groundwater level is located at the upper boundary of the domain (0.70 m). The initial oil pressures are set equal to the initial water pressures, which is the critical oil pressure for sat-

urated aqueous-phase conditions (White, Oostrom and Lenhard, [51]*).* The boundary conditions are: zero flux Neumann conditions at the left boundary of the domain to simulate a vertical symmetry axis. Furthermore, the initial lowering of the groundwater level is simulated by a step-wise linearly declining Dirichlet boundary condition for water pressure at the bottom of the domain (see Figure 2.3 from $T = 0$ h until $T = 1$ h) so that a groundwater level of 0.07 m is achieved in agreement with the experiment (Lenhard, Oostrom and White*,* [29]*).* Infiltration of 70 ml of oil into the domain from the top is modeled by a Neumann boundary condition on top surface by imposing a flux on the top of the symmetry axis and the nearest 3 horizontal nodal points from $T = 12.2$ h until $T = 12.3$ h. The oil accumulates above the groundwater level until $T = 17.4$ h. From this moment where the oil is situated above the groundwater level, we distinguish two different situations: one where the groundwater level remains stable at 0.025 m from the bottom of the domain (see the dashed line in Figure 2.3). This situation is referred to as the reference case to compare with the effects of another more complex model. For the other situation, after the accumulation of the oil on the groundwater, the groundwater level fluctuates due to varying the water pressure at the bottom of the domain. This pressure is a sinusoidal function of time such that the groundwater level varies between 0.025 m and 0.25 m (see the solid line in Figure 2.3). The situation that concerns the fluctuations is referred to as the fluctuation case.

2.4 Results

2.4.1 Numerical results

To assess which one of the retention functions is the most appropriate for our case, we test both functions by comparing numerical calculations based on either BC or VG with experimental data that were obtained from Lenhard (Lenhard and Parker [25]; Lenhard, Johnson and Parker [28]; Lenhard, Oostrom and White [29]; Lenhard, Parker and Kaluarachchi [31]). These data were measured during a one-dimensional three-phase flow experiment in which the groundwater level fluctuated two times. The water and oil content have been measured during 25 h from the start at six elevations.

The fluctuations in the results in Figure 2.4 indicate the fluctuations of the groundwater level. At $T = 12.5$ h the oil was applied to the upper boundary which results in an increase of S_o and a slight decrease of S_w in
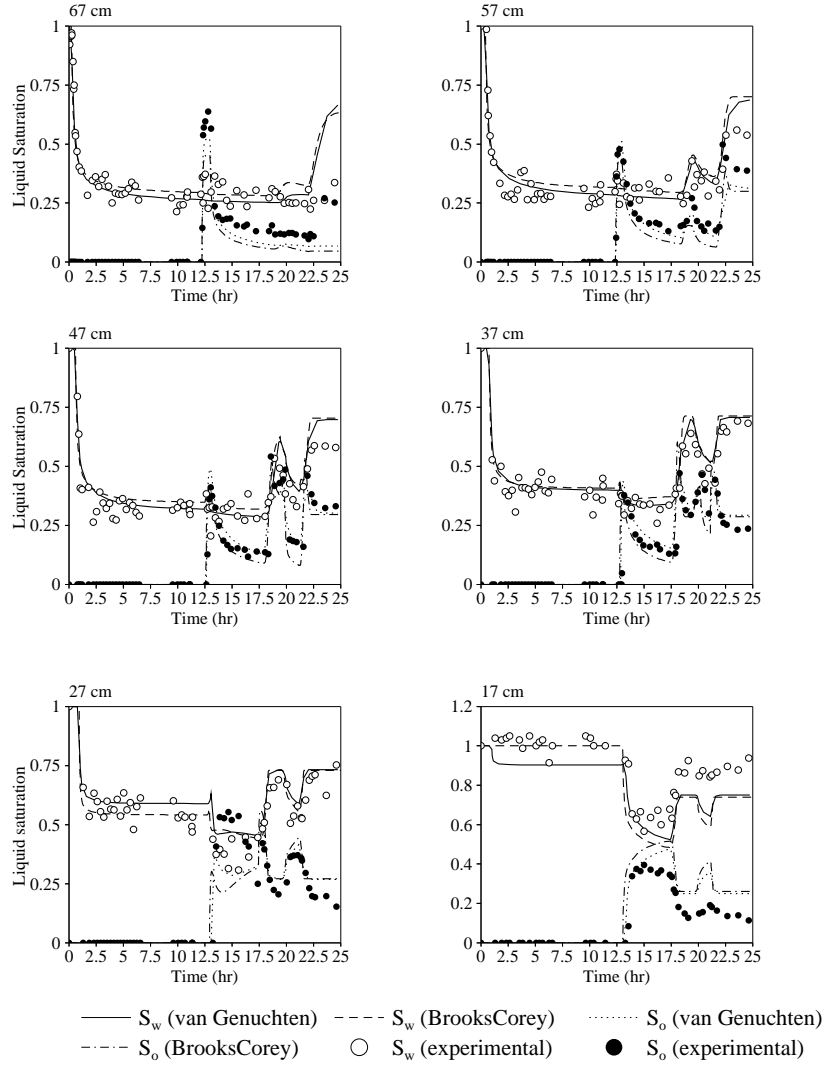
Figure 2.4: Numerically calculated fluid saturations using the Van Genuchten and Brooks-Corey retention function versus experimentally measured fluid saturations. Every graph represents a depth (top left corner) in the domain i.e. 67-, 57-, 47-, 37-, 27-, and 17-cm position. The different lines in the graphs represent the water saturation (solid line) and the oil saturation (dotted line) calculated by the van Genuchten function and the water saturation (dashed line) and oil saturation (dash-dotted line) calculated by the Brooks-Corey function. The dots indicate the experimental water saturation and oil saturation.

Depth [cm]	σ_w^{VG}	σ_o^{VG}	σ_w^{BC}	σ_o^{BC}
17	0.125	8.676e-2	0.145	0.137
27	7.093e-2	9.730e-2	7.295e-2	0.126
37	5.650e-2	8.263e-2	5.547e-2	0.103
47	6.923e-2	7.082e-2	7.098e-2	8.073e-2
57	6.123e-2	4.245e-2	6.949e-2	6.713e-2
67	8.451e-2	6.025e-2	8.670e-2	7.767e-2

Table 2.2: Standard deviations between the measured water and oil satura-tions, VG numerically calculated water and oil saturations and BC numerically calculated water and oil saturations.

the lower part of the domain. The oil moves downwards which results in a decrease of S_o in the upper areas. At $T = 17.5$ h and at $T = 21.1$ h the water table was raised which results in fluctuations of both S_w and S_o. For a more detailed description of the experimental and simulation results, see Lenhard et al. [28] and Lenhard et al. [29]. They particularly noted that air was entrapped during oil imbibition, which is shown in Figure 2.4 at 67 cm where the largest total saturation of water and oil is 0.96 after oil imbibition at $T = 12.5$ h. Oil and air are entrapped during water imbibition since the oil-water capillary pressure head was measured to be < 0 at the 47-cm position which indicates that the oil and air phase present at 47-cm should be discontinuous blobs. Since the air entrapment is small, compared to the oil entrapment, we assume the air entrapment to be zero.

Comparison of the experimental and numerical data show that the VG function gives better results in the upper area of the domain, while at the lowest depth the BC function is more accurate. This is shown in Figure 2.4. At the 67-cm and 57-cm position we see that especially the oil saturation is better approximated by VG while the water saturation does not give a clear indication which function provides a better fit. At the 47-cm, 37-cm and 27-cm position both the water and oil saturation do not clearly show which function fits better. However at the 17-cm position the oil saturation is better approximated by VG while BC fits the water saturation during the two-phase (water and air) segment from $T = 0$h until $T = 12.5$ h much better than VG. This better accuracy at small depths is caused by the entry pressure that needs to be exceeded before drainage takes place, which is accounted for by the BC function but not by the VG function. For a more detailed comparison, we calculated the standard deviation σ ($\sigma^2 = \int_{-\infty}^{\infty} (x\text{-}X)^2 dx$, where x is the mean value and X is the true value of

case	n	α [m^{-1}]	V_1 [m^2]	S_{or}^{max}	S_{min}	β_{ow}
1	3.16	1	6.9e-4	0.395	0.20	1.8
2	3.16	6	6.9e-4	0.395	0.20	1.8
3	2.00	1	6.9e-4	0.395	0.20	1.8
4	4.00	1	6.9e-4	0.395	0.20	1.8
5	3.16	1	3.4e-4	0.395	0.20	1.8
6	3.16	1	1.4e-3	0.395	0.20	1.8
7	3.16	1	6.9e-4	0.195	0.20	1.8
8	3.16	1	6.9e-4	0.595	0.20	1.8
9	3.16	1	6.9e-4	0.395	0.00	1.8
10	3.16	1	6.9e-4	0.395	0.60	1.8
11	3.16	1	6.9e-4	0.395	0.20	1.125
12	3.16	1	6.9e-4	0.395	0.20	2.25

Table 2.3: Parameters and characteristic lengths and times used in the computations. Case 1 is identical to the parameters described in Table 2.1

the quantity) between both the VG and BC function and the experimental data at different depths (see Table 2.2). Since the VG function gives for all depths the best average results for the complete domain and since the numerical calculations converge much faster to a solution for this function, we chose to use this function for further calculations.

We also consider a two-dimensional problem where we distinguish between a reference case where the oil accumulates above a stationary groundwater level and between a fluctuation case where the groundwater level fluctuates as a function of time. A typical computation time varies between a few minutes and a few days depending on the chosen parameters. Especially the BC retention function results in large computation times. The results of the reference case where the parameters described in Table 2.1 (case 1 in Table 2.3) are used, are shown in Figure 2.5.a, where we see the redistribution of the oil in terms of the vertically integrated free oil saturations (w_f) and in terms of the vertically integrated trapped oil saturations (w_t), at two dimensionless moments in time t_1 and t_2:

$$w_f(t_i) \;=\; \phi \int S_{of}(t)dz \qquad (2.25)$$

$$w_t(t_i) \;=\; \phi \int S_{ot}(t)dz \qquad (2.26)$$
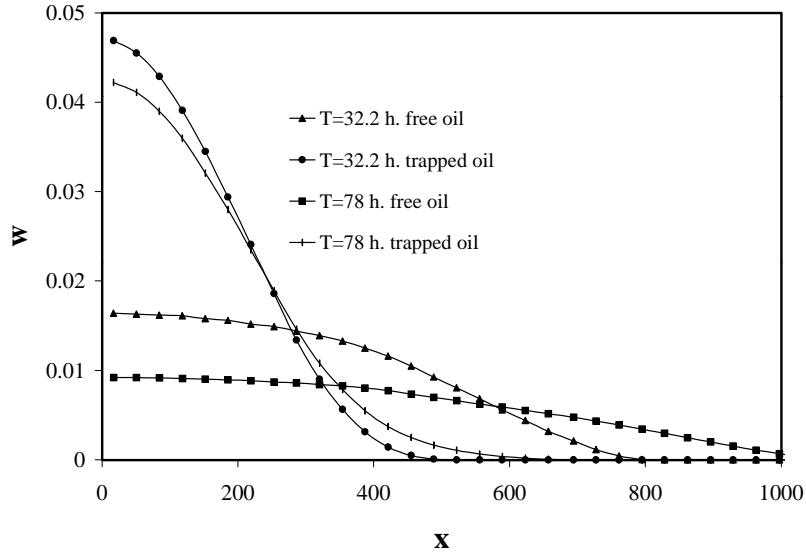
(a)
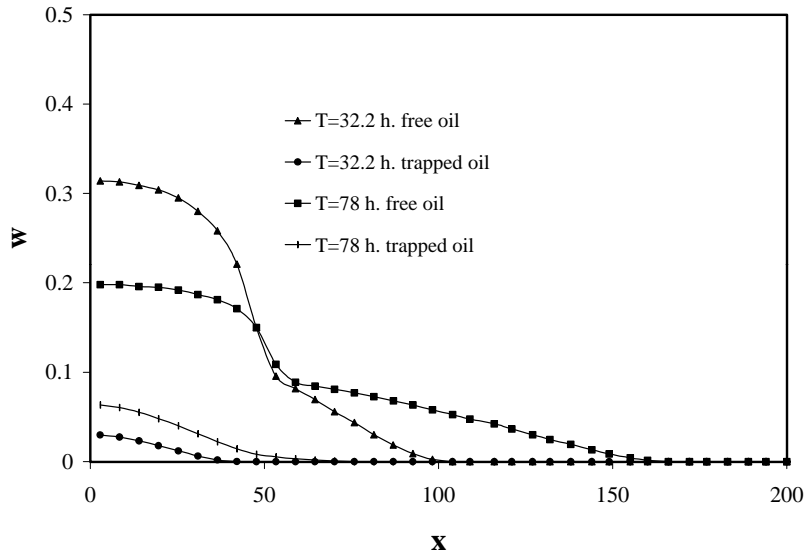
(b)

Figure 2.5: Reference situation. Free and trapped oil volumes per unit lateral area for (a) case 1 with $\alpha = 1m^{-1}$ and (b) for case 2 with $\alpha = 6m^{-1}$, at two times (note the differences in scale).

We integrate vertically because we want to emphasize the effect of the fluctuations on the horizontal migration and therefore we want to exclude the vertical redistribution.

To evaluate the effect of the VG parameter α, two cases were considered, namely Case 1 ($\alpha = 1m^{-1}$) and Case 2 ($\alpha = 6m^{-1}$). The results are presented in Figures 2.5.a and 2.5.b for the situation where no water table fluctuations were simulated, and in Figures 2.6.a and 2.6.b for the situation where fluctuations were considered. It is clear that for Case 1 the horizontal migration is faster than for Case 2 while for Case 2 w_f is larger per unit lateral area. We see that α has a large impact on the horizontal migration of the oil. In the reference case we see that when $\alpha = 1m^{-1}$ there is a higher degree of horizontal movement compared to the situation where $\alpha = 6m^{-1}$. Figure 2.7 shows that Case 1 ($\alpha = 1m^{-1}$) is fine sand and therefore has a rather steep capillary pressure-saturation curve, which means that the water saturation in the capillary fringe (zone directly above the saturated zone) is higher than for Case 2 ($\alpha = 6m^{-1}$) which is coarse sand and produces a flatter capillary pressure curve (see Equation (2.10)). Due to the higher water saturation in the capillary fringe, vertical downwards movement of oil is retarded in Case 1. As a consequence, the oil moves laterally, so that the total contact area between oil and water is larger. The oil phase eventually breaks up into blobs of entrapped oil, which are immobilized by capillary forces. If we compare Figures 2.5.a and 2.6.a to examine the effect of the fluctuations, we see for α equal to $1m^{-1}$ that after 10 fluctuations ($T = 32.2$ h) horizontal migration of the mobile phase has been retarded. In the middle of the lens (the symmetry axis) the amount of mobile oil is larger than in the reference case. After 21 fluctuations ($T = 78$ h) these effects are even more profound. The same is shown in Figures 2.5.b and 2.6.b for $\alpha = 6m^{-1}$, i.e. fluctuations cause a retardation in the horizontal migration. The amount of mobile oil in the middle of the lens however is approximately the same in the fluctuation case and the reference case. A comparison of Figures 2.5.a and 2.6.a with 2.5.b and 2.6.b indicates that there is a difference in the amount of entrapment at the symmetry axis. Retardation in horizontal migration varies with α-values.

The development of w_f during a fluctuation is as follows: when the groundwater level rises, the oil phase is entrapped (or immobilized); as the water table falls, oil becomes mobile again. The effects of the fluctuations on w_f are shown in Figure 2.6.a and 2.6.b. The results of the fluctuation case are calculated at the moments in time when the groundwater level is
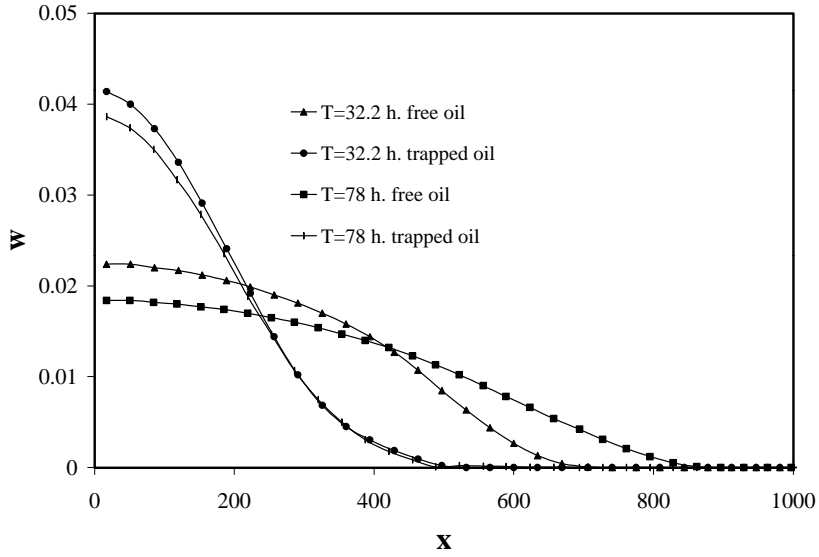
(a)
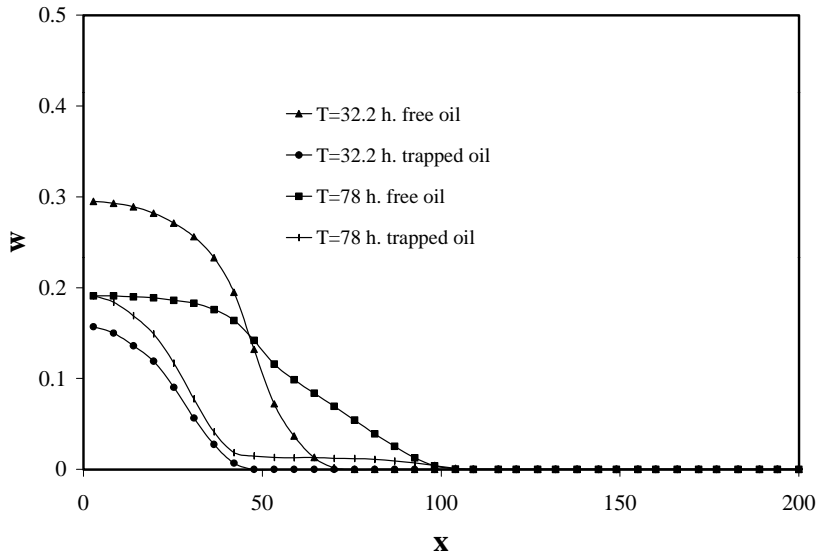
(b)

Figure 2.6: Profiles situations with fluctuations included: w_f as function of unit lateral area at two times for (a) case 1 where $\alpha = 1m^{-1}$ and (b) case 2 where $\alpha = 6m^{-1}$ (note the differences in scale).
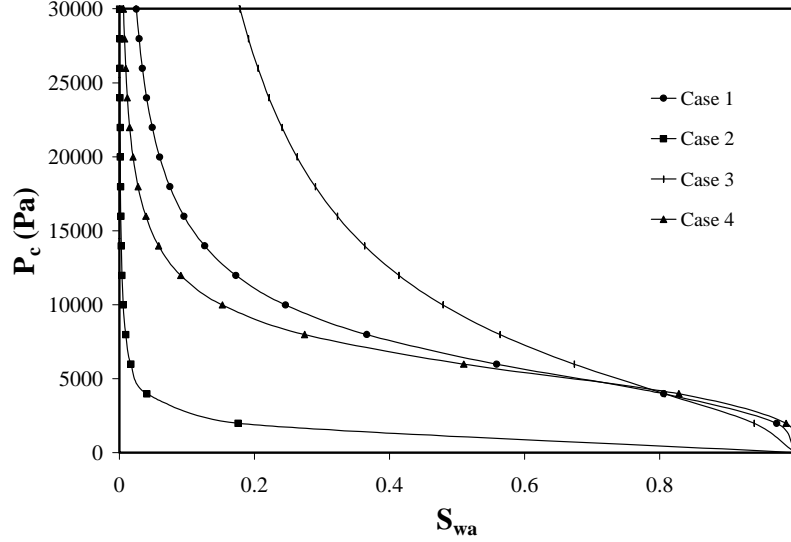
Figure 2.7: Apparent water saturation-capillary pressure relations using the Van Genuchten retention relation for Case 1, 2, 3 and 4.

at its lowest position which coincides with the groundwater level in the reference case. That moment seems to be the most straight forward choice for a comparison with the reference case. We see that the horizontal migration in the fluctuation case is smaller ($x = 700$ until $x = 850$ for Case 1 and $x = 70$ until $x = 100$ for Case 2) than in the reference case ($x = 800$ until $x = 1000$ for Case 1 and $x = 100$ until $r = 160$ for Case 2) from $T = 32.2$ h until $T = 78$ h. Comparison between the fluctuation case and the reference case reveals that the horizontal migration of the lens is impeded in the fluctuation case and that the amount of mobile oil decreases slower in the fluctuation case. During the raise of groundwater, the oil is entrapped into the water phase, i.e. the oil becomes immobile. As it is not able to migrate in the horizontal direction, the horizontal migration is retarded. In the reference case the oil migrates through the unsaturated zone until it reaches the capillary fringe where it migrates horizontally above the saturated zone. During this horizontal migration part of the oil gets entrapped into the water phase. Since the horizontal migration of the oil in time is related to the entrapment in time, retardation of horizontal migration in the fluctuation case means that also the entrapment of oil in the water phase is retarded in time.

To show the effect of redistribution on the amount of mobile oil we calculate the total amount of free oil v_f at a certain moment in time T_i for the reference case and for the fluctuation case:

$$v_f(t_i) = \int w_f dx \qquad (2.27)$$

We calculate at $T_1 = 32.2$ h, $v_f(T_1) \approx 7.1$ and at $T_2 = 78$ h, $v_f(T_2) \approx 6.1$ where the initial total oil volume per unit width v_t is 15.8. The dimensionless free oil volumes per unit width in a fluctuating case are: $v_f(T_1) \approx 9.2$ and $v_f(T_2) \approx 9.1$ again with v_t is 15.8. This means that the total amount of mobile oil in the reference case decreases faster than in the fluctuation case. During the rising of the groundwater level, imbibition occurs and the oil becomes entrapped. This entrapment is reversed during the lowering of the groundwater level (drainage) to the original position when the oil becomes mobile again. Only during the periods when the oil is mobile, the oil can migrate and becomes entrapped because of the larger contact area between water and oil. This process is not reversible and is the same process as the entrapment process that occurs continuous in the reference case. The discontinuity in the migration of the fluctuation case results in a retardation in horizontal migration and in a larger amount of mobile oil.

To show the effect of varying parameter values on the amount of mobile oil we compute the volume of free oil and the maximum horizontal distance that is covered by the oil lens for the different parameters that are presented in Table 2.3. Since we are looking at the amount of entrapment, we decided to vary the parameters that influence the entrapment (Equations (2.5) and (2.10)), namely α, n, V_1, $S_{or}^{\max}$, $S_{\min}$ and β_{ow}.

We vary the parameter n in Cases 3 and 4 and present the results in Figure 2.8.a at $T = 32.2$ h. At previous moments in time the same features are visible

and at later moments in time the oil lens will reach the boundary. As has been mentioned, n has a large influence on the migration rate, which increases if n decreases. In the fluctuation case we see that the horizontal migration is retarded and the amount of mobile oil on the symmetry axis is larger. If we change the initial oil volume, a few features are seen: the horizontal migration is retarded and the amount of mobile oil on the symmetry axis is larger in the fluctuation case compared with the reference case (Figure 2.8.b. (Cases 5 and 6)). Since we have used $\alpha = 1m^{-1}$ in Cases 5 and 6, it is logical that the same features appear as in Figure 2.6.a and 2.6.b. The same is done for $S_{or}^{\max}$ (Figure 2.8.c (Cases 7 and 8)), $S_{\min}$

n

(a)

v

(b)

(c)

(d)

β$_{ow}$

(e)
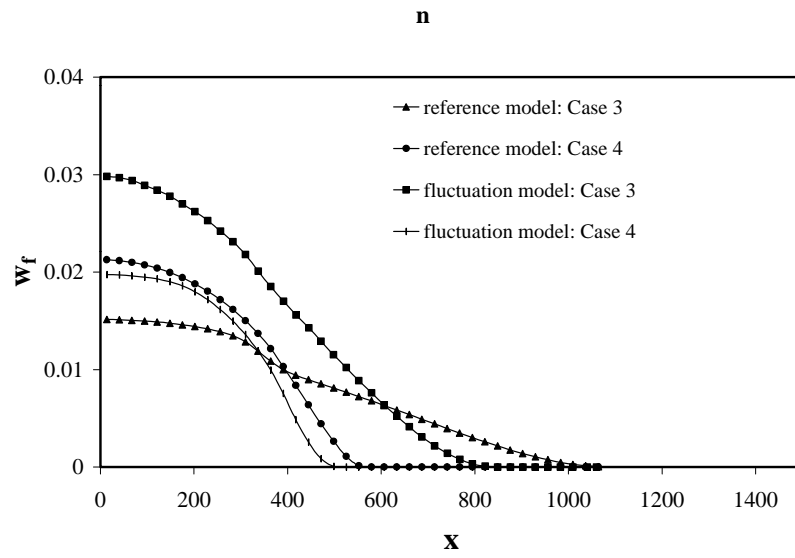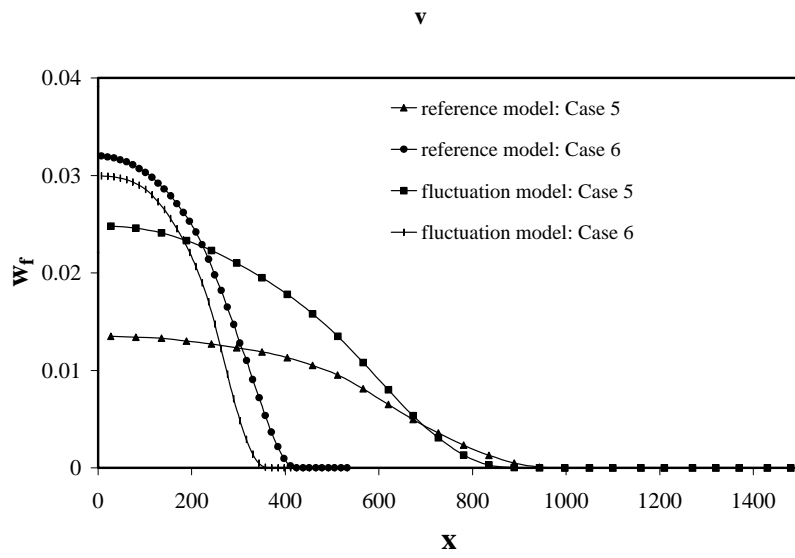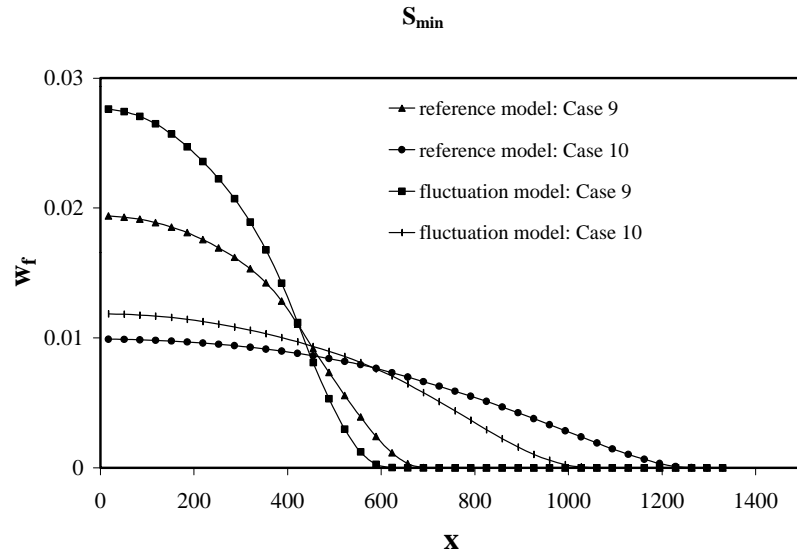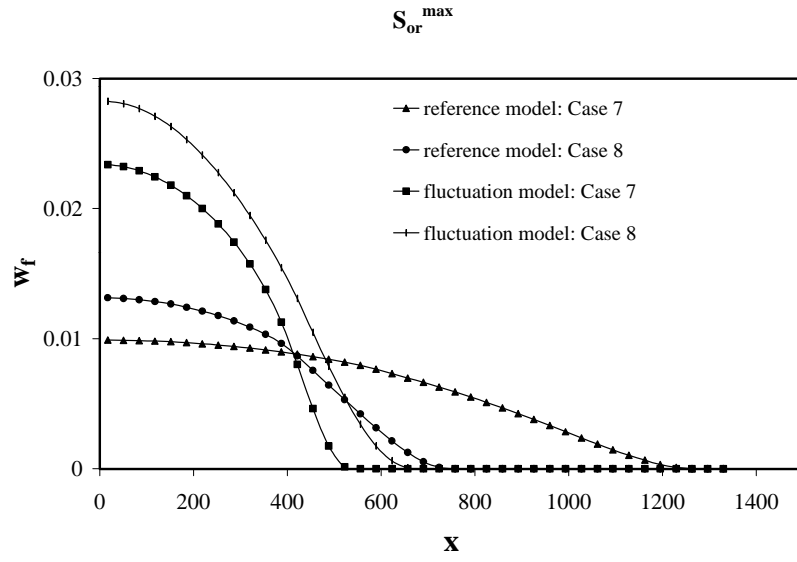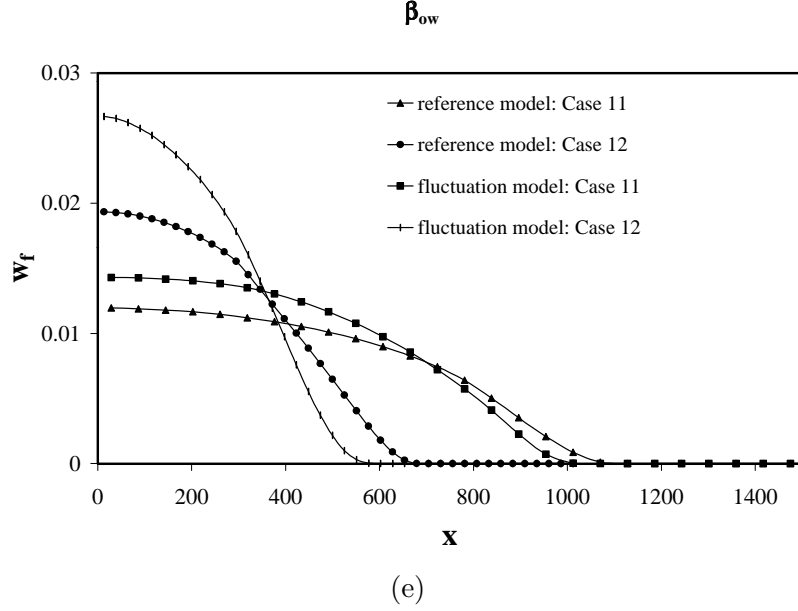
Figure 2.8: Parameter variation for free oil at $T = 32.2h$.: a. Case 3 and 4. b. Case 5 and 6. c. Case 7 and 8. d. Case 9 and 10. e. Case 11 and 12.

(Figure 2.8.d (Cases 9 and 10)) and β_{ow} (Figure 2.8.e (Cases 11 and 12). Comparing the reference case with the fluctuation case we see for all cases with different values for α, n, V_1, S_{or}^{max}, S_{min} and β_{ow} that retardation of migration and retardation in the amount of entrapment takes place in the fluctuation cases.

To account for the amount of entrapment quantitatively, we first studied this phenomenon in relation to the groundwater level numerically. We looked at the difference in the amount of mobile oil between the reference case and the fluctuation case at certain x-coordinates. Since w_f diminishes from the middle of the lens to the borders, we scale this difference to the amount of mobile oil in the reference case ($\frac{w_f - w_{f,f}}{w}$), where w_f and $w_{f,f}$ are respectively the free oil volume in the reference and in the fluctuation case. This means that if this value is 1, the oil in the fluctuation case is entrapped and if it is 0, all oil in the fluctuation case is mobile. To show that this scaled difference behaves sinusoidal, we implement the scaled groundwater fluctuation. It can be seen in Figure 2.9 that the amount of mobile oil has a relation with the groundwater level during the complete fluctuation. We can use this information to develop an analytical method to predict the
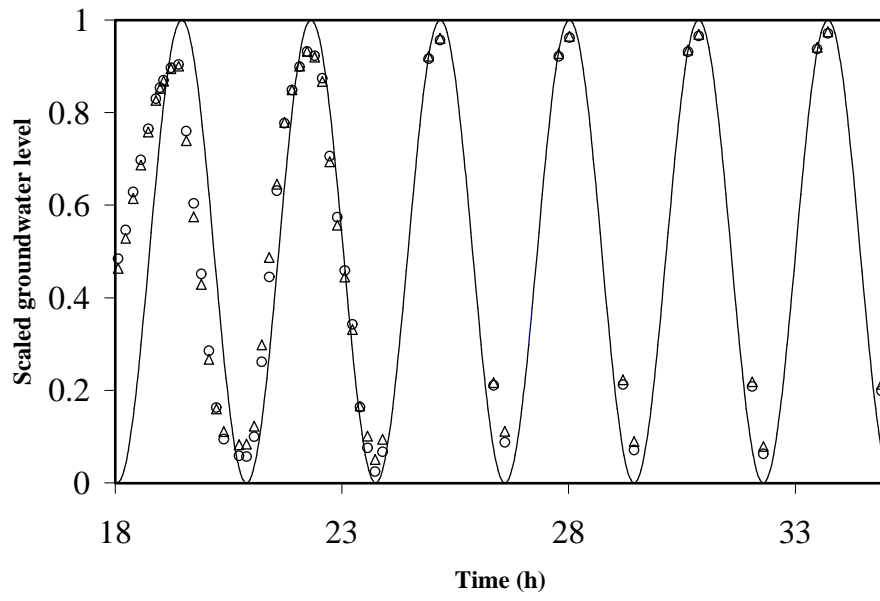
Figure 2.9: The relative amount of entrapment compared with the scaled groundwater level. The ∘ represents $\frac{w_f - w_{f,f}}{w_f}$ near the symmetry axis, △ represents $\frac{w_f - w_{f,f}}{w_f}$ 25 cm from the symmetry axis and the solid line represents the scaled groundwater level.

horizontal migration.

2.4.2 Analytical approximation

As has been mentioned, it may require considerable computational effort (CPU time, memory demand) to compute some of the cases. Furthermore, if the main phenomena to be studied concerns vertically averaged properties in view of their robustness, much of the numerical model details are not really necessary. Hence we assess in this section whether recent analytical results are able to capture the main observed trends with minor computational efforts. Van Dijke and Van der Zee developed a 2-D semi-analytical solution for oil redistribution with entrapment. This solution takes the form of the similarity solution (Van Dijke and Van der Zee [44]) for a vertical cross-section of the soil. Similarity solutions can be used for a phenomenon that is self-similar which means that the spatial distributions of its properties at various moments of time can be obtained from one another by a similarity transformation.

Van Dijke and Van der Zee assumed that the oil lens is at vertical equilibrium so that consequently the vertical component in Equation (2.9) may be omitted and the vertical capillary pressure distributions (P_{ao} en P_{ow}) are approximately hydrostatic. With $f = \frac{\rho_w}{\rho_o}$ (see Equation (2.20)) and $P_o(X, 0, T) = \rho_o g Z_{ao}$, where we assume $Z = 0$ at the bottom of the domain:

$$P_{ow}(X, Z, T) = \Delta\rho g(Z_{ow}\text{-}Z) \qquad (2.28)$$

$$P_{ao}(X, Z, T) = \rho_o g(Z_{ao}\text{-}Z) \qquad (2.29)$$

where Z_{ow} is the level above which oil is present and Z_{ao} is the level above which air is present. Substitution of the dimensionless variables in Equation (2.7) in Equations (2.28) and (2.29) results in:

$$p_o = z\text{-}z_{ao} \qquad (2.30)$$

If we substitute this in the Richard's Equation (2.9) and if we neglect the vertical flow velocity, the Richard's equation for the oil phase becomes:

$$\phi\frac{\partial S_o}{\partial t}\text{-}\frac{(1\text{-}D)^2}{V_1(\alpha\beta_{ow})^2}\frac{\partial}{\partial x}(k_{ro}\frac{\partial z_{ao}}{\partial x}) = 0 \qquad (2.31)$$

Because vertical pressure distributions are hydrostatic, we further reduce Equation (2.31) by vertical integration, which requires evaluation of:

$$w_f = \phi \int S_{of}dz \quad and \quad \overline{k} = \int k_{ro}(S_{wa}, S_t)dz \qquad (2.32)$$

where $w_f(x,t)$ represents the free oil volume per unit lateral area and $\overline{k}(x,t)$ the vertically integrated relative permeability. z_{ao} and $\overline{k}$ in Equation (2.31) are rewritten in terms of w_f:

$$z_{ao} = \lambda_1 w_f^{\frac{1}{n+1}} \quad and \quad \overline{k} = \lambda_2 w_f^{\frac{5n-2}{2(n+1)}} \qquad (2.33)$$

where λ_1 and λ_2 are constants. The vertically integrated time derivative of Equation (2.31) can be written as:

$$\frac{\partial w_o}{\partial t} = \begin{cases} \frac{\partial w_f}{\partial t} & if \quad \frac{\partial w_f}{\partial t} \geq 0 \\ \frac{\partial w_f}{\partial t}(1\text{-}c_t) & if \quad \frac{\partial w_f}{\partial t} < 0 \end{cases} \qquad (2.34)$$

This yields for Equation (2.31) :

$$F(\frac{\partial w_f}{\partial t}) = \gamma \frac{\partial}{\partial x}(w_f^q \frac{\partial w_f}{\partial x}) \qquad (2.35)$$

where

$$p = \frac{1}{1\text{-}c_t}, \quad p \geq 1 \qquad (2.36)$$

$$\gamma = \frac{(1\text{-}D)^2 p \lambda_1 \lambda_2}{(\alpha \beta_{ow})^2 V_1(n+1)} \qquad (2.37)$$

$$q = \frac{3n\text{-}2}{2(n+1)} \qquad (2.38)$$

$$F(y) = \begin{cases} py & if \quad y \geq 0 \\ y & if \quad y < 0 \end{cases} \qquad (2.39)$$

and c_t is the trapping constant. Equation (2.35) is the modified porous medium equation, that according to Hulshof and Vazquez [17] admits a similarity solution of the form:

$$w_{fa}(x,\overline{t}) = \overline{t}^\mu h(x\nu^{\frac{1}{2}}\overline{t}^\nu) \qquad (2.40)$$

$$\overline{t} = \gamma \cdot (t\text{-}t_0) \qquad (2.41)$$
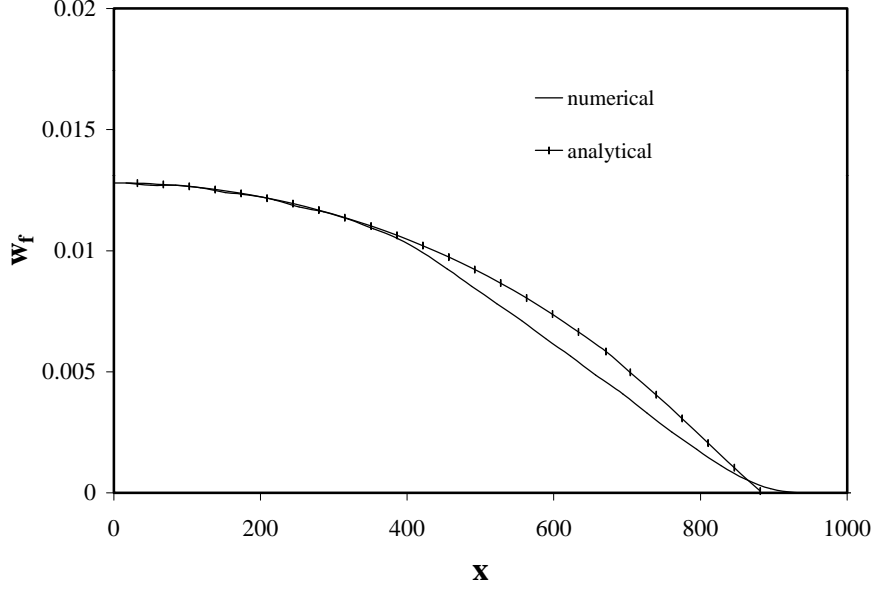
Figure 2.10: Numerical and analytical free oil volumes per unit lateral area (w_{of}) at t is 15533.8.

where w_{fa} is the analytically calculated free oil volume per unit lateral area, x is the dimensionless horizontal coordinate and $\bar{t}$ the time. h is the similarity profile, μ and ν are powers that are determined by the decrease of the total free oil volume and the free oil volume in the middle of the lens (Van Dijke and Van der Zee [44]), γ is a dimensionless parameter defined by Equation (2.37) in the nonlinear diffusion equation and t_0 represents the time at which the solution becomes singular. For more detailed information about the assumptions made and the derivation of the similarity solution we refer to Van Dijke and Van der Zee [44]. The similarity solution is initially not applicable; however, shortly after the start of the simulations the similarity solution provides a good approximation (Van Dijke and Van der Zee [44]). The initial conditions do not have the similarity shape of w_{fa}, however for increasing times the shape of w_f converges reasonably fast to the shape of w_{fa}. The similarity solution contains a part that represents the shape of the w_{fa} curve (h) and it contains a part that represents the changes in the behavior of the solution in time ($\bar{t}$), i.e. the multiplicator of h.

After comparison of the similarity solution with numerical calculations, it appeared to provide a good approximation of the computed horizontal extension of the lens and the fraction of mobile oil. This is shown in Figure 2.10 at an arbitrarily chosen moment in time. For a more detailed description of this solution we refer to Van Dijke and Van der Zee [44], who show that this solution is applicable for a wide range of time and different parameter values.

Since the similarity solution (Equations (2.40) and (2.41)) is based on vertical flow equilibrium, we account for a fluctuating groundwater level by mathematically manipulating the similarity solution. Since the fluctuating groundwater level has an effect solely on the changes of the solution in time and not on the shape of the solution, it is logical that we have to concentrate on $\bar{t}$. In view of the earlier results this means that we determine the retardation in time of horizontal migration for the fluctuation case. Additionally we investigate how the retardation in time can be predicted so that $\bar{t}$ can be manipulated in such a way that the fluctuation case can be simulated analytically. The assumption of vertical flow equilibrium is not in conflict with a vertical dynamic situation as in the fluctuation case, because we only focus on the situations where the groundwater level has returned to its original lower level and on the retardation in the horizontal dimension.

We consider the retardation in horizontal migration for the case where the lowest groundwater level is almost at the bottom of the domain and the highest level is at $z = \frac{P_w(X,0,0)}{\rho_o g}$ (see Equation (2.21)). When the groundwater level rises, oil becomes entrapped and is prevented from migration. Figure 2.9 shows the scaled groundwater level as a function of time. As mentioned before, it is clear from Figure 2.9 that the amount of mobile oil in time has a relation with the scaled groundwater level in time. During the period when the scaled groundwater level is zero, the same amount of mobile oil is present as in the reference case and during this period it can migrate horizontally as fast as in the reference case. However, when the scaled groundwater level is one, the total amount of oil is entrapped in the fluctuation case and it can not migrate horizontally during this period. This means that the oil can migrate during the period when the scaled groundwater level is zero. Since the fluctuation of the groundwater level is not a block function, we assume that integration of the scaled groundwater level in time represents that part of the actual simulated time in which the oil cannot spread horizontally. This integration should satisfy the time
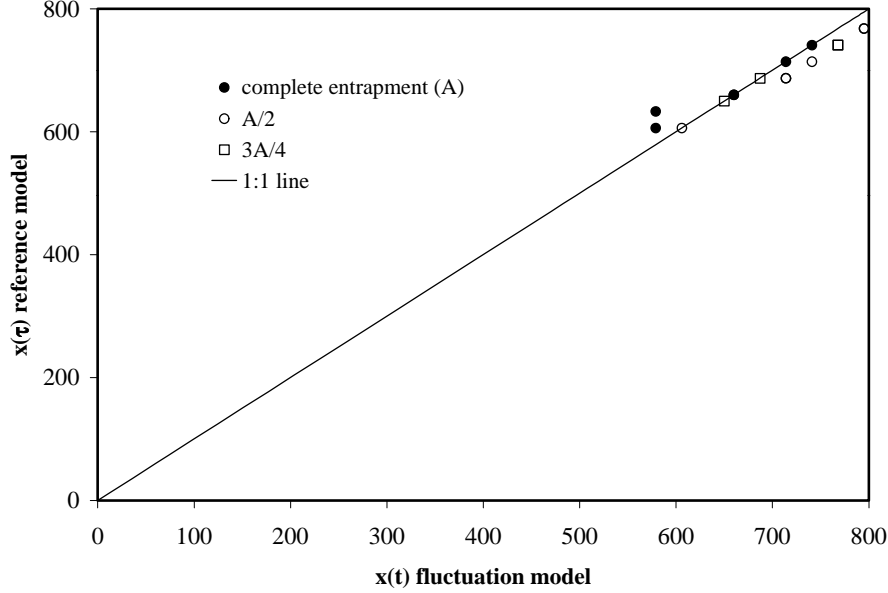
Figure 2.11: The horizontal spreading measured in the fluctuation model at time t plotted against the horizontal spreading measured in the reference model at time τ. The open circles represent a fluctuation where the amplitude causes complete entrapment ($A = \frac{P_o(0)}{\rho_o g}$) at different moments in time, the filled circles represent a fluctuation with half this amplitude ($A = \frac{P_o(0)}{2\rho_o g}$) at different moments in time and the squares represent a fluctuation with 0.75 times this amplitude ($A = \frac{3P_o(0)}{4\rho_o g}$) at different moments in time.

that the oil does not migrate in the case that the fluctuation amplitude results in total oil entrapment at its highest position. For smaller amplitudes where the oil does not become completely entrapped, the integration must be corrected by the relative quantity of entrapment that goes with the fluctuation amplitude. For this purpose we use Equation (2.23) (see Section 2.2.3) where we assume a linear relation between the amplitude of the fluctuation and the amount of entrapment. The time that the oil does migrate horizontally is called flow time (τ) and is related to the simulated time by substraction the time that the oil is not able to migrate:

$$\tau = t - \frac{0.5A\rho_o g}{P_o(X,0,0)} \int_0^t (1 + \cos \varpi t) dt \qquad (2.42)$$

where A is the amplitude of the fluctuation. This means that since we
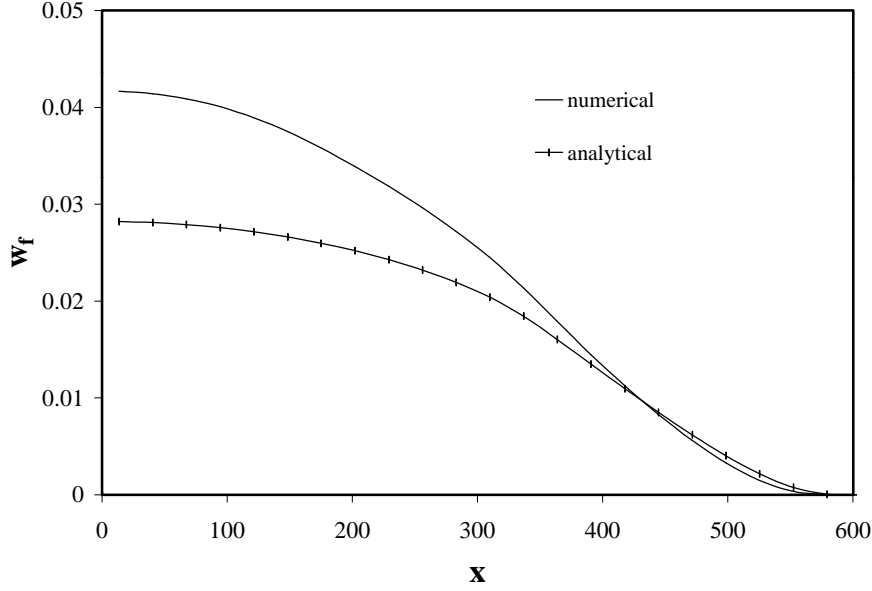
Figure 2.12: Numerical and analytical solution for fluctuation model: free oil volume per unit lateral area for case 1 at t is 10776.8.

have chosen in this situation to use a sinusoidal fluctuation and since $A = \frac{P_o(X,0,0)}{\rho_o g}$, oil can spread only half of the time:

$$\tau = t\text{-} \int_{t_1}^{t} (0.5 + 0.5 \cos \varpi t) dt \qquad (2.43)$$

where t_1 is the point in time where the fluctuations begin. This flow time can be substituted in t in Equation (2.41). To test this approximation, we compare the fluctuation case at a certain time t and the reference case at the flow time τ. The maximum migration which is defined by the x-coordinate where w_f becomes zero is calculated numerically at the simulated time in the fluctuation case and analytically at τ in the similarity solution and these values are plotted against each other. In Figure 2.11 we see that the flow time approximation fits rather well for different amplitudes of the fluctuation at different moments in time. The deviations all have the same values and are identical to the size of one grid cell which is very small, i.e. the deviations are caused by the numerical grid and shall become smaller by decreasing the grid.

τ (Equation (2.43)) can be substituted for t in Equation (2.41) to obtain

the correct horizontal migration analytically. The result is shown in Figure 2.12 where we can see that the horizontal migration is approximately the same for the analytical and numerical solutions at a certain moment in time, i.e. both the solutions show that the oil has reached $x \approx 570$. From Figure 2.11 we can conclude that this solution is applicable for a wide range of time. Conversely it is clear from this figure that the amount of dimensionless free oil in the middle of the lens is much smaller for the analytical solution. This means that the flow time approximation (Equation (2.43)) can not be used to predict the retardation in the decrease in mobile oil and it is solely applicable for predicting the horizontal migration (see Figure 2.11). The reason for that is that approximately the total volume of oil becomes mobile after lowering of the groundwater level, i.e. the total volume of free oil is decreasing very slowly and there is no relation between the volume of free oil and the integration of the relative groundwater level. We suggest that this should be implemented in the similarity solution by manipulation of the mathematically determined similarity powers μ and ν, since these powers are determined by the decrease of the total free oil volume and the decrease of the free oil volume in the middle of the lens. The advantage of this analytical method to predict the horizontal migration is less computing time compared to the numerical calculations and it is a verification of the numerical results.

The approximation can be adapted to homogeneous situations with different values for the parameters, in a very simple way. Since the similarity solution is a semi-analytical solution, based on two numerical measurements of w_f, we test whether different cases could be calculated by just adapting the dimensionless variables or if for each case a new similarity solution should be developed based on new numerical calculations. The parameters that are used to determine the dimensionless variables are shown in Equation (2.7). From the definitions, we see that it is possible that changes in parameters cancel each other, e.g. K and μ_o so that there is no change in the dimensionless variable. Furthermore other changes in parameter values will affect the dimensionless variables (Equation (2.7)) which can easily be implemented in the similarity solution. We tested the assumptions that changes in parameters can cancel each other and that changes in parameter values solely result in a change in a dimensionless parameter value by comparing numerical and analytical results and the results show the same agreement between numerical and analytical solutions as in Figure 2.12. Since we use the numerically calculated free oil profile to

develop the semi-analytical solution, the choices for the retention function and the relative permeability function will not influence the applicability of the semi-analytical solution. The entrapment function however (Equation (2.5)) will influence the solution and adaptions should be made in case of a different entrapment function. This means that the horizontal migration can be predicted by one similarity solution for situations based on various parameter values.

In reality a fluctuating groundwater level will behave in a more complex way than a simple sinusoidal function. Considering the different amplitudes and the different parameter values, we expect that other fluctuation functions than a sinusoidal function can also be incorporated in Equation 2.42. The basic idea of the flow time is to integrate the fluctuation function to achieve the time that the oil can actually flow and it should be investigated whether this flow time depends on the type of fluctuation function or not. Furthermore, in reality the soil is mostly not homogeneous. Since we have seen that different parameter values for α, n, V_1, $S_{or}^{\max}$, $S_{\min}$ and β_{ow} all result in retardation of horizontal migration (see Section 2.4.1), we assume that a fluctuating groundwater level in a heterogeneous medium with horizontal layers, where these parameter values will vary through the layers, will also result in retardation of horizontal migration. Equation (2.42) should be adapted for a heterogeneous medium in such a way, that the time that the oil is not able to migrate is calculated for each layer. Furthermore the oil will become entrapped since the interfaces between the layers form a capillary resistance. This phenomena should also be taken into account.

2.5   Conclusion

From a numerical study of the differences between a situation where oil redistribution above the groundwater level is investigated and the same situation where fluctuations of the groundwater level are included, the following can be concluded. During rising and lowering of the groundwater level the oil becomes respectively entrapped and mobile again. As long as the oil is entrapped horizontal migration of the oil lens is impeded and therefore the migration is retarded compared to the case without fluctuations. The extent of the retardation depends on the amplitude of the fluctuation. We found a criterion which the amplitude must fulfill to yield complete entrapment of the oil phase into the water phase. In accordance with this criterion we derived an equation for the retardation and for pro-

viding a flow time for the reference situation where the solution coincides with the fluctuation case at the simulated time.

An analytical solution for oil redistribution above the groundwater level was already available in the form of the similarity solution that describes the free oil volume per unit lateral area. This similarity solution consists of a part that represents the shape of the solution and a part that represents the development in time. We manipulated the part that represents the development in time by using the flow time instead of the simulated time to simulate the fluctuation case. It appeared that this analytical solution gives a very good approximation of the horizontal migration. This way it is possible in a relative simple and fast way to calculate the horizontal migration of an oil lens above a groundwater level that fluctuates in time for different situations.

Notation

A	the amplitude of the fluctuation
c_t	trapping constant
D	parameter determining finiteness of lens thickness
f	multiplicator of $P_o(0,0)$ to obtain $P_w(0,0)$
F	trapping function
F_L	Land's factor
g	gravity [m s^{-2}]
h	similarity profile
h_w	waterhead [m]
K	absolute permeability [m^2]
k_{ri}	phase i relative permeability
$\bar{k}$	vertically integrated oil relative permeability
n	van Genuchten parameter
p	trapping constant in function F
P_e	entry pressure for the capillary pressure [Pa]
P_i	phase i pressure [Pa]
P_c	characteristic pressure [Pa]
P_{ik}	phases i, k capillary pressure [Pa]
q	power in coefficient of diffusion equation
$X(x)$	(dimensionless) horizontal coordinate [m]
X_c	characteristic horizontal length [m]
S_i	phase i saturation

S_{of}	free oil saturation
S_{ot}	trapped oil saturation
S_{or}^{max}	maximum residual oil saturation
S_t	total fluid saturation
S_{wa}	apparent water saturation
S_w^{min}	minimum water saturation
$T(t)$	(dimensionless) time [h]
T_c	characteristic time [h]
t_0	starting time of similarity solution
t_1	starting time of the fluctuations
$\bar{t}$	time in similarity solution
U_i	phase i horizontal flow velocity [m s^{-1}]
V_i	phase i vertical flow velocity [m s^{-1}]
V_1	initial oil volume in 2-D [m^2]
v_f	dimensionless free oil volume
v_t	dimensionless total oil volume
w_f	dimensionless free oil volume per unit lateral area [m]
w_t	dimensionless trapped oil volume per unit lateral area [m]
$Z(z)$	(dimensionless) vertical coordinate [m]
$Z_{ao}(z_{ao})$	(dimensionless) elevation beyond which air is present [m]
Z_c	characteristic vertical length [m]
$Z_{ow}(z_{ow})$	(dimensionless) elevation beyond which oil is present [m]
α	van Genuchten parameter [m^{-1}]
$\beta_{ao},\ \beta_{ow}$	ratios of air-oil and oil-water to air-water surface tensions
γ	dimensionless parameter in nonlinear diffusion equation
λ	Brooks-Corey parameter
$\lambda_1,\ \lambda_2$	constants in power law approximations of z_{ao} and $\bar{k}$
$\mu,\ \nu$	powers in similarity solution
μ_i	phase i viscosity [Pa s]
ρ_i	phase i density [kg m^{-3}]
σ	standard deviation
τ	part of the actual simulated time in which the LNAPL can spread horizontally (flow time)
ϕ	porosity
ω	angular velocity of the fluctuation

Chapter 3

Comparison of experiments and modeling: the influence of a fluctuating groundwater level on the migration of an LNAPL lens*

3.1 Introduction

The contamination of groundwater by Light Non Aqueous Phase Liquids (LNAPL) as a result of improper disposal practices, spills and leaking storage facilities, poses a serious threat to drinking water resources. In this chapter we consider LNAPLs which are less dense than water and may accumulate as a lens above the phreatic surface. Knowledge of the distribution of LNAPLs in the soil environment is essential in order to effectively remediate a contaminated site. Correspondingly, it is important to investigate the horizontal migration of the oil lens and the quantity and location of trapped oil. This is a multiphase flow problem that involves the three phases air, oil and water. Henceforth we use the term oil as a comprehensive term for LNAPLs.

To model this flow problem Parker and Lenhard [34] and Lenhard and Parker [25] introduced saturation-pressure relationships which account for hysteresis and fluid entrapment in porous media containing up to three immiscible fluid phases. Later, Lenhard et al. [30] and Kaluarachchi and Parker [18] derived a simplified model of fluid entrapment by restricting hysteresis to entrapment of oil by water. They found that their results were almost identical to the full model where hysteresis was also included. White et al. [51] used the same formulation to develop a three-dimensional, three-

phase, compositional engineering simulator for modeling LNAPL migration and remediation technologies. Later they also included the possibility to use the simplified model for fluid entrapment. We use this simulator for our numerical calculations.

An oil plume migrates through the unsaturated zone until it reaches the capillary fringe where the oil will spread laterally above the saturated zone. Seasonal changes, intermittent pumping or heavy rainfall will change the depth of both the groundwater level and the capillary fringe. The groundwater level will fluctuate vertically as a function of time. Earlier numerical experiments on oil entrapment and a fluctuating groundwater level were done by Kaluarachchi and Parker [18]. Their results showed that fluid entrapment markedly reduces the lateral migration since much of the oil volume is trapped and thus immobile. Lenhard et al. [28] concluded from experiments that to predict the movement of oil in the subsurface, where the water table elevation may fluctuate, constitutive relations among fluid saturations and pressures need to account for nonwetting fluid entrapment. The same conclusion was made by Pantazidou and Sitar [33], who performed two-dimensional experiments. Van Geel and Sykes [48] showed numerically and experimentally fluid entrapment during fluctuation of the groundwater level. They focussed on the importance of a hysteretic model. The effect of fluctuations was investigated in Chapter 2 more quantitatively. We showed numerically that fluctuations of the groundwater level results in retardation in the horizontal migration of the oil lens. This retardation is a function of the amplitude of the fluctuation. Additionally, we found a semi-analytical solution that predicts the retardation as a function of the amplitude. Although the agreement between analytical and numerical calculations was good, only a test with experimental results can establish whether the main phenomena have been accurately accounted for.

Since this semi-analytical solution in Chapter 2 is verified by numerical calculations solely, we performed laboratory experiments to verify the results more extensively. Reported experimental data were not sufficient for this goal, since no earlier research used a reference experiment, with a stagnant groundwater level. This chapter presents the comparison between experimental results and model results concerning an oil spill in a laboratory chamber and the effects of a fluctuating groundwater level on the entrapment of the oil. The oil spill was numerically modeled using the same code as in Chapter 2 is used, i.e. the code developed by White et al.[51]. The aim of this work is to verify whether earlier numerical and

analytical solutions are adequate to predict the retardation in horizontal migration caused by a fluctuating groundwater level. In contrast to the earlier experimental works on a fluctuating groundwater level [29][33][48], we quantify the retardation in migration, which will contribute significantly to the knowledge of the geometrical distribution of the oil lens.

3.2 Theory

3.2.1 Governing equations

The governing equations for the flow of water, oil and air in a three-phase system are the mass balance equations:

$$\phi\frac{\partial S_i}{\partial T} + \frac{\partial U_i}{\partial X} + \frac{\partial V_i}{\partial Z} = 0, \quad i = w, o \tag{3.1}$$

and Darcy's Law:

$$U_i = -\frac{Kk_{ri}}{\mu_i}\frac{\partial P_i}{\partial X} \tag{3.2}$$

$$V_i = -\frac{Kk_{ri}}{\mu_i}(\frac{\partial P_i}{\partial Z} + \rho_i g), \quad i = w, o \tag{3.3}$$

where the subscript i denotes either the water (w) or the oil (o) phase. The equations for the air phase are omitted since the air phase is assumed to be a passive phase i.e. the porespace that is not filled with oil or water, is filled with air. S_i is the effective phase saturation, U_i and V_i are respectively the horizontal and vertical phase velocities. T is time and X and Z are respectively the horizontal and vertical coordinates, and ϕ is the porosity. K is the absolute permeability, k_{ri} is the relative phase permeability, and μ_i is the phase viscosity. P is the phase pressure, ρ_i is the phase density, and g the gravity acceleration. Combination of equations (3.1), (3.2) and (3.3) yields the Richards equation:

$$\phi\frac{\partial S_i}{\partial T} - \frac{\partial}{\partial X}(\frac{Kk_{ri}}{\mu_i}\frac{\partial P_i}{\partial X}) - \frac{\partial}{\partial Z}(\frac{Kk_{ri}}{\mu_i}\frac{\partial P_i}{\partial Z}) - \rho_i g\frac{\partial}{\partial Z}(\frac{Kk_{ri}}{\mu_i}) = 0, \quad i = w, o \tag{3.4}$$

The constitutive relations are as defined by Parker and Lenhard [34]:

$$
\begin{aligned}
S_w + S_o &= S_t \\
S_t + S_a &= 1 \\
S_w + S_{ot} &= S_{wa} \\
S_{of} + S_{ot} &= S_o \\
P_{ow} &= P_o\text{-}P_w \\
P_{ao} &= \text{-}P_o
\end{aligned}
\tag{3.5}
$$

where S_t is the total liquid saturation and S_a is the air saturation. S_{wa} is the apparent water saturation, S_{ot} is the trapped oil saturation and S_{of} is the free oil saturation. P_{ow} is the oil-water capillary pressure and P_{ao} is the air-oil capillary pressure which is identical to -P_o since we assume the atmospheric pressure (P_a) to be constantly zero.

To describe entrapment of oil, a linearized equation is used according to Kaluarachchi and Parker [18] that can be easily implemented in numerical multiphase flow codes :

$$
S_{ot} = min[(\frac{1\text{-}S_w^{min}}{1 + F_L(1\text{-}S_w^{min})} - \frac{1\text{-}S_{wa}}{1 + F_L(1\text{-}S_{wa})}), S_o]
\tag{3.6}
$$

$$
F_L = \frac{1}{S_{or}^{max}}\text{-}1
\tag{3.7}
$$

where S_{ot} is the trapped oil saturation and S_w^{min} is the minimum water saturation. F_L is Land's factor, where S_{or}^{max} is the maximum residual oil saturation. Equation (3.6) prevents that the trapped oil saturation becomes larger than the oil saturation.

The capillary pressure-saturation relationships based on the Van Genuchten capillary pressure-saturation relationship[49] and extended to three phases by Parker, Lenhard and Kuppusamy [36] are given by:

$$
S_{wa} = \begin{cases}
1 & if\ P_w > 0\ and\ P_o < P_w & (a) \\
(1 + (\frac{\alpha\beta_{ow}}{\rho_w g}\,P_{ow})^n)^{\text{-}m} & if \begin{cases} 0 < P_w < P_o\ or \\ P_w < 0\ and\ P_o > \frac{1}{\beta_{ao}}P_w \end{cases} & (b) \\
(1 + (\frac{\text{-}\alpha}{\rho_w g}\,P_w)^n)^{\text{-}m} & if\ P_o < \frac{1}{\beta_{ao}}P_w < 0 & (c)
\end{cases}
\tag{3.8}
$$

$$S_t = \begin{cases} 1 & if \ P_o > 0 \ or \ P_w > 0 \quad (a) \\ (1 + (\frac{\alpha\beta_{ao}}{\rho_w g} P_{ao})^n)^{-m} & if \ \frac{1}{\beta_{ao}}P_w < P_o < 0 \quad (b) \\ S_{wa} & if \ P_o < \frac{1}{\beta_{ao}}P_w < 0, \quad (c) \end{cases} \quad (3.9)$$

where α and n are parameters, $m = 1\text{-}\frac{1}{n}$, β_{ow} is the oil-water surface tension and β_{ao} is the air-oil surface tension.

The relative permeability functions that are used are according to Lenhard and Parker [24]:

$$k_{rw} = S_w^{\frac{1}{2}}(1\text{-}(1\text{-}S_w^{\frac{n}{n-1}})^{1\text{-}\frac{1}{n}})^2 \quad (3.10)$$

$$k_{ro} = (S_t\text{-}S_{wa})^{\frac{1}{2}}((1\text{-}S_{wa}^{\frac{n}{n-1}})^{1\text{-}\frac{1}{n}}\text{-}(1\text{-}S_t^{\frac{n}{n-1}})^{1\text{-}\frac{1}{n}})^2 \quad (3.11)$$

3.2.2 Similarity solution

It may require considerable computational efforts to calculate the equations numerically. Therefore Van Dijke and Van der Zee developed a two-dimensional semi-analytical solution for oil redistribution with entrapment, based on vertical flow equilibrium. Their semi-analytical solution assumes the form of a similarity solution, i.e., a function of a transformed variable $\eta = x\nu^{\frac{1}{2}}\bar{t}^{\nu}$.

For the derivation of the semi-analytical solution, Equation (3.4) is solved after dimensionless transformation according to the following characteristic lengths and times:

$$Z_c = \frac{1\text{-}D}{\alpha\beta_{ow}}, \quad X_c = \frac{V_1\alpha\beta_{ow}}{(1\text{-}D)}, \quad T_c = \frac{\mu_o V_1\alpha\beta_{ow}}{K\rho_o g(1\text{-}D)}, \quad P_c = \frac{\rho_o g(1\text{-}D)}{\alpha\beta_{ow}}$$
$$(3.12)$$

where $D = \frac{\beta_{ow}\Delta\rho}{\beta_{ao}\rho_o}$ is an indication of the thickness of the lens and V_1 is the initial oil volume or oil surface since we concern a two-dimensional problem ($V_1 = \phi\int_{-\infty}^{\infty}\int_0^{\infty} S_o(X,Z)dXdZ$). This results in the following dimensionless variables:

$$z = \frac{\alpha\beta_{ow}}{1\text{-}D}Z, \quad x = \frac{(1\text{-}D)}{V_1\alpha\beta_{ow}}X, \quad t = \frac{K\rho_o g(1\text{-}D)}{\mu_o V_1\alpha\beta_{ow}}T, \quad p_o = \frac{\alpha\beta_{ow}}{\rho_o g(1\text{-}D)}P_o \quad (3.13)$$

Equation (3.4) expressed in dimensionless variables becomes :

$$\phi\frac{\partial S_o}{\partial t}\text{-}\frac{(1\text{-}D)^2}{V_1(\alpha\beta_{ow})^2}\frac{\partial}{\partial x}(k_{ro}\frac{\partial p_o}{\partial x})\text{-}\frac{V_1(\alpha\beta_{ow})^2}{(1\text{-}D)^2}\frac{\partial}{\partial z}k_{ro}(\frac{\partial p_o}{\partial z}+1)=0 \qquad (3.14)$$

Furthermore we assume that vertical flow velocities are negligible as the result of a balance of vertical capillary and gravitational forces, i.e. we assume that the oil lens is at vertical equilibrium so that consequently the vertical component in Equation (3.14) can be averaged vertically and the vertical capillary pressure distributions are hydrostatic. Hydrostatic pressure distributions result in [44]:

$$
\begin{aligned}
P_{ow}(X,Z,T) &= \Delta\rho g(Z_{ow}\text{-}Z) & (3.15) \\
P_{ao}(X,Z,T) &= \rho_o g(Z_{ao}\text{-}Z) & (3.16)
\end{aligned}
$$

where Z_{ow} is the level above which oil is present and Z_{ao} is the level above which air is present. Substitution of the dimensionless variables in Equation (3.12) in Equations (3.15) and (3.16) results in:

$$p_o = z\text{-}z_{ao} \qquad (3.17)$$

If we substitute this in Equation (3.14) and if we neglect the vertical flow velocity, the Richard's equation for the oil phase becomes:

$$\phi\frac{\partial S_o}{\partial t}\text{-}\frac{(1\text{-}D)^2}{V_1(\alpha\beta_{ow})^2}\frac{\partial}{\partial x}(k_{ro}\frac{\partial z_{ao}}{\partial x})=0 \qquad (3.18)$$

This particular solution takes the form of the similarity solution [44] for a vertical cross-section of the soil:

$$w_f(x,\overline{t}) = \overline{t}^{-\mu}h(x\nu^{\frac{1}{2}}\overline{t}^{\nu}) \qquad (3.19)$$

$$\overline{t} = \gamma\cdot(t\text{-}t_0) \qquad (3.20)$$

where w_f is the analytically calculated free oil volume per unit lateral area ($w_f = \phi\int S_{of}dz$), x is the dimensionless horizontal coordinate. h is the similarity profile that describes the shape of the solution that remains constant, μ and ν are similarity powers that are related to the numerical decrease of the total free oil volume and the free oil volume in the middle of the lens [44]. The exact derivation of μ and ν is out of the scope of this

study. γ is a dimensionless parameter and t_0 represents the time at which the solution becomes unique. t is the dimensionless time in the model. This similarity solution consists of a part that represents the shape of the solution (h) and a part that represents the development in time ($\bar{t}$).

In Chapter 2 this similarity solution is manipulated in such a way that it accounts for the retardation in horizontal spreading caused by a fluctuating groundwater level that causes temporal entrapment. We assumed a linear relation between the amplitude of the fluctuation and the amount of entrapment. The vertical flow equilibrium assumption is not in conflict with this vertical dynamic situation caused by the fluctuations, since we focussed on the situation where the groundwater level has returned to its original constant lower level solely. Their approach involved substitution of a flow time τ for the time t, where the flow time is the time the oil does migrate horizontally:

$$\tau = t \text{-} \frac{0.5 A \rho_o g}{P_o(0,0)} \int_0^t (1 + \cos \omega t) dt \qquad (3.21)$$

where A is the amplitude of the fluctuation, ρ_o is the oil density, g is gravity and $P_o(0,0)$ is the oil pressure at $t = 0$ and $x = 0$. ω is the angular velocity of the fluctuation. In Chapter 2 it is assumed that integration of the scaled groundwater level in time ($0.5 \int_o^t (1 + \cos \omega t) dt$) represents that part of the actual simulated time in which the oil can not spread horizontally. In other words: we scale the time in such a way, that during the time the oil is entrapped, τ evolves slower than t. This integration should satisfy the time that the oil does not migrate in the case that the fluctuation amplitude results in total entrapment at its highest position ($A = \frac{P_o(X,0,0)}{\rho_o g}$). For smaller amplitudes where the oil does not become completely entrapped, the integration must be corrected by the relative quantity of entrapment that goes with the fluctuation amplitude ($\frac{A \rho_o g}{P_o(0,0)}$). This approximation was tested for situations with different values for the parameters by comparison with numerical calculations. It appeared that this semi-analytical solution gives a very good approximation of the retardation in horizontal migration.

3.3 Method

3.3.1 Experimental setup

In the laboratory, oil was spilled in a plexiglass chamber, 40 cm in horizontal length, 40 cm in height and 2.5 cm in horizontal depth at a temperature of
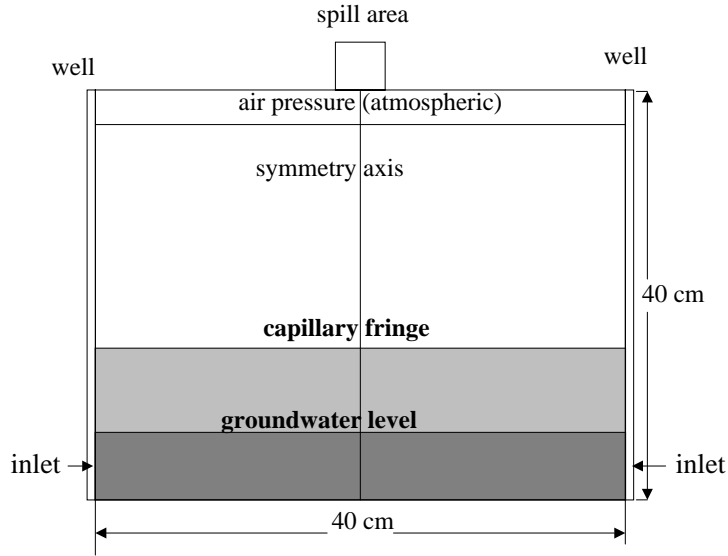
Figure 3.1: Setup and boundary conditions.

18° C. This chamber has vertical wells at each side that control the changes in the water head during the experiment (Figure 3.1).

The chamber was filled up until 35 cm with materials composed of artificially crushed white silica sands (AWK, Hirschau, D) with grain size distribution in the range 0.25-0.50 mm. Then the chamber was water filled and sand was added through a funnel until it reached 35 cm height. Water was drained from the model, until the sand contains constant residual water after 2 hours. Yellow dyed (Fluresceine) tap water was added to the well on the right hand side until a stable groundwater table was achieved of 10 cm from the bottom of the box. Water was pumped through the sand to create steady state conditions. After 2 hours the pumping stopped and red dyed (Sudan IV) oil was introduced in the center of the model via a plastic tube that was connected to a peristaltic pump. A total amount of 15 ml oil (Jetfuel A-1, Statoil, Norway) was added to the packed sand with a constant infiltration rate of 3 ml/min. The density of this oil is 0.8 g/cm^3 and the viscosity is 0.019 Pa s.

After the oil was introduced in the center of the box at the top of the sand pack, the oil plume development was studied through digital imaging

taken at given intervals. After 360 Min the oil had reached the capillary fringe of 8-9 cm above the groundwater table, and the oil started to spread laterally on top of the capillary fringe. The fluctuations as described were now introduced.

The fluctuations in water level were induced by pumping dyed tap water in or out through the wells of the chamber. At first water was pumped into the model to increase the water table from 10 cm to 12 cm. Next, water was slowly pumped out of the model during a period of 12 hours until the groundwater level was at 2 cm, the pump was instantly reversed and water was pumped into the model during the next 12 hours. One complete cycle where the water table is set to fluctuate between 12 cm and 2 cm was thus completed in 24 hours. The experiment continued until the oil started to flow out of the experimental domain. In addition, a reference experiment was performed without fluctuations.

Digital pictures were taken 5 Min, 60 Min, 360 Min after oil introduction, and then every 12 hours during the fluctuations. They were taken both at the lower and upper position of the complete cycle of the fluctuation.

3.3.2 Measurement and analysis of hydraulic parameters

In order to define the hydraulic parameters of the sand types used in the experiment, we performed multi step outflow analyses using an inverse modeling approach developed by Van Dam et al. [43]. This experiment is performed independently of the fluctuation experiment but in the same plexiglass chamber. The multi step outflow analysis is a variant of the one-step outflow method in which the inverse modeling approach was originally developed by Kool et al.[20]. In the multi step outflow experiment they performed, a soil sample is placed in a pressure cell on top of a saturated ceramic plate which has a relative large hydraulic conductivity and a high entree pressure for air. The soil sample is initially saturated with water (the wetting fluid), introduced through the ceramic plate at the bottom. From above the pneumatic air pressure is increased stepwise and water outflow through the plate is measured. The inverse model [43] solves the Richards equation for unsaturated flow in porous media for the given boundary conditions. The used hydraulic functions were the Van Genuchten function and the Mualem function [49].

We applied a similar procedure for the plexiglass chamber as is described in section 3.3.1. Instead of increasing the air pressure we decreased the water pressure stepwise and measured the outflowing water. Initially the
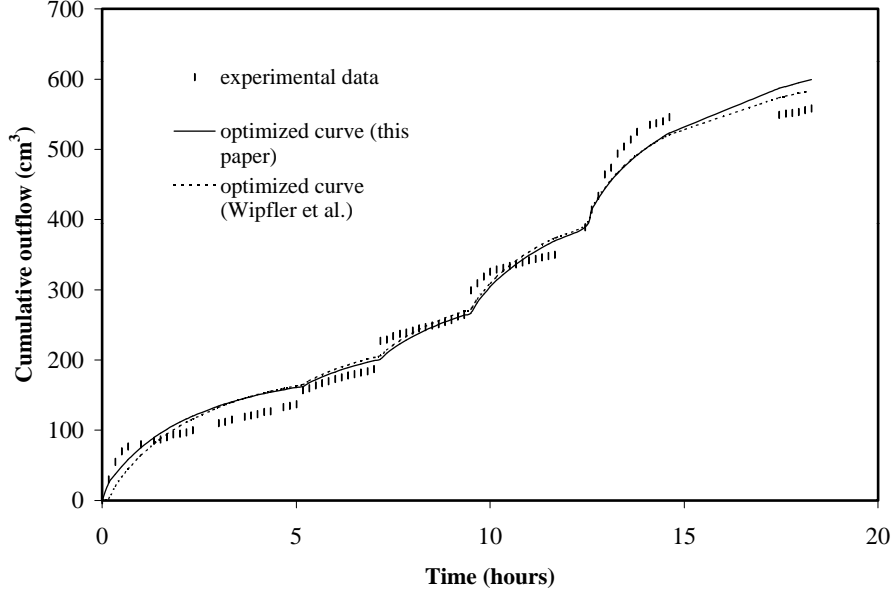
Figure 3.2: Cumulative water outflow as a function of time.

sand filled plexiglass chamber was completely water saturated. Next the water pressure head was decreased stepwise in 5 or 6 steps. One experiment took approximately 15 hours. The results are shown in Figure 3.2, where cumulative outflow is plotted as a function of time. As the bottom of the column was continuously completely water saturated, no ceramic plate was needed (a ceramic plate is normally used to prevent air entry, since it has a high entry pressure for air). Measuring the outflow at near saturation gives less accurate results as it introduces non-uniform flow [43]. However, the advantage of this variant is that the same packing technique is used for determination of the hydraulic parameters as for the main experiments. The optimized hydraulic functions are applied in the inverse model. From the total volume of water that could be introduced in the sand box (resp. 1160 ml and 1090 ml) we calculated the porosity to be $\phi = 0.55$.

In addition, we performed experiments to determine the vertical conductivity. If we rewrite Darcy's Law (3.3) for water expressed in hydraulic heads:

$$Q_w = K_{hc} G \frac{dH}{dZ} \tag{3.22}$$

	fine sand
$S_w^{\min}$	0.08 ± 0.04
n	3.1 ± 0.4

Table 3.1: The hydraulic parameters calculated by inverse modeling.

where Q_w is the flux of water out of the model, K_{hc} is the hydraulic conductivity, G is the flux area and H is the hydraulic head. This experiment was conducted in the same plexiglass chamber where the hydraulic head on top of the sand was kept constant and where the volume of water out of the model was measured as a function of time. The hydraulic conductivity was 0.05 cm/s $\pm$ 0.007. The inverse model optimizes for 2 parameters: the residual water saturation, $S_w^{\min}$, and the van Genuchten parameter n. The results are shown in Table 3.1. Wipfler et al. [53] optimized in similar work using the same experimental data for 3 parameters: $S_w^{\min}$(=0.19), α (=8.0 m^{-1}) and n (=3.9). Since these parameter values did not simulate the 2-D experimental results satisfactorily, we chose to fix $\alpha = 7.0m^{-1}$ to obtain a larger capillary fringe. According to the good approximation in Figure 3.2 for both this paper and for the optimized curve obtained by Wipfler et al., this means that the method developed by Van Dam [43] does not give a unique optimization.

3.3.3 Numerical setup

The multiphase flow code STOMP developed by White et al. [51] was used to model the two-dimensional laboratory experiment. This code is based on the equations described in Section 3.2. The governing flow and transport equations are in this case solved numerically by following an integrated finite-difference method. Spatial discretization of the computational domain with the integrated finite-difference method is limited to orthogonal grid systems. The algebraic forms of the nonlinear governing equations are solved with a multi-variable residual-based Newton-Raphson iteration technique.

The parameters used in this experiment are described in Table 3.2. The surface tensions were measured in the laboratory. We used an orthogonal Cartesian domain of height 35 cm, discretized by 72 nodes, and of width 20 cm, discretized by 80 nodes. For symmetry reasons we only model half the domain and therefore the left boundary presents the vertical symmetry axis. The initial time step was 10 s and the maximum allowable timestep

Property	Value
Irreducible water saturation S_m	0.08
Genuchten parameter α	7.0 m^{-1}
Genuchten parameter n	3.1
Air-water scaling factor β_{aw}	1.0
Air-NAPL scaling factor β_{ao}	2.28
NAPL-water scaling factor β_{ow}	1.78
Intrinsic permeability K	1.9×10^{-11} [m^2]
Porosity ϕ	0.55
NAPL density ρ	800 [kg/m^3]
NAPL viscosity μ	2.046×10^{-3} [Pa s]
Length of sandbox	0.35 [m]
Width of sandbox	0.40 [m]

Table 3.2: Parameters used in the computations.

was 10 min.

The initial conditions for this experiment are as follows: the 2-D domain is homogeneously filled with sand (see Figure 3.1). At the bottom of the domain a water pressure is applied that results in a completely water saturated domain. The initial oil pressure at the bottom of the domain is equal to the water pressure so that an imaginary amount of oil is situated above the domain. The boundary conditions are: 1. Zero flux Neumann conditions at the left boundary of the domain in view of the vertical symmetry axis. 2. Lowering of the groundwater level was simulated by a step-wise linearly declining Dirichlet boundary condition for water pressure at the bottom of the domain to accomplish a groundwater level of 16 cm (see Figure 3.3 from $T = 0$ h until $T = 0.5$ h). 3. A flux on the top of the symmetry axis and the 3 nearest nodal points in the horizontal direction are the Neumann boundary condition that describes the oil infiltration of 7.5 ml from $T = 12.2$ h until $T = 12.3$ h.

Due to gravity and capillary forces the oil spreads along the groundwater level. Here we distinguish between two different situations: one where the groundwater level remains stable at 16 cm from the bottom of the domain (see the dashed line in Figure 3.3). This situation is referred to as the reference case to compare with the effects of the more complex fluctuation model. The fluctuations of the groundwater level are simulated by changing the water pressure at the bottom of the domain and the resulting height of
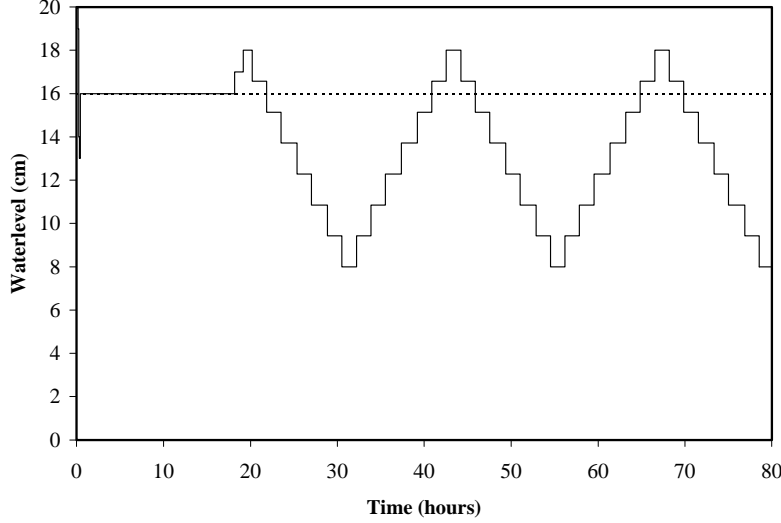
Figure 3.3: Water level from the bottom of the sandbox as a function of time, where the solid line represents the waterlevel in the fluctuation model and the dashed line represents the waterlevel in the reference model.

the groundwater level is shown in Figure 3.3. The situation that concerns the fluctuations is referred to as the fluctuation case.

The height of the water level for the numerical simulations is chosen to be 16 cm instead of the 10 cm that is used in the experiment. This was done to account for the heterogeneities that occur in the experiment. In the experiments, these heterogeneities were apparent as layers of slightly different textures and coloring. The thickness of such layers vary from millimeters to centimeters. These heterogeneities form a capillary barrier for the water phase causing water to accumulate above these capillary barriers. This was shown by e.g. Wipfler et al. [53] and Ross [37]. Consequently the water level in the two wells (see Figure 3.1) does not give the correct indication for the total water saturation in the chamber. Visually the capillary fringe was found to be centimeters higher than expected solely from the applied water pressure at the bottom and therefore we have chosen to increase the water level for the numerical experiment. In view of both the visual inspection of the experiments and the outcome of trial simulations, the waterlevel was taken to be 16 cm in the numerical approach. An

time	exp. fluct. case	num. fluct. case	exp. ref. case	num. ref. case
(hours)	depth (cm) oil front			
12.3	29	29.1		
13.2	21.8	24.5		
18.2	20.8	19.2		
20.2	18.3	19.2		
32.2	16.1	14.6	18.6	18.2
44.2	16.1	14.6	18.6	18.2
67.2	15.8	11.9	18.6	18.2
	width (cm) oil front			
20.2	7.8	7.3		
32.2	9.4	7.9	12.7	10.0
44.2	9.4	7.9	14.0	11.7
67.2	8.6	8.0	16.5	13.1

Table 3.3: The geometry of the oil lens in the different cases.

alternative approach, where either the heterogeneities or anisotropy were accounted for was disregarded as computationally more involved as well as equally arbitrary in view of the lack of an adequate parameterization.

3.4 Results

3.4.1 Experimental results

The experimental results for the fluctuation case are shown in Figure 3.4.a and 3.5.a. Figure 3.4.a represents the oil front at time $T = 12.3$ h and at $T = 13.2$ h. This oil front is determined by the boundary where the red dye in the oil is visible. The oil front has not yet reached the groundwater level which is situated at $Z = 10$ cm and no fluctuations are incorporated at this point in time. The depth that is reached by the oil front is approximately 29 cm at $T = 12.3$ h and 21.8 cm at $T = 13.2$ h from the bottom of the chamber. This is also shown in Table 3.3, where the maximum depth and maximum width of the oil lens for these calculations are shown.

In Figure 3.5.a the oil front is shown at $T = 18.2$ h, at $T = 20.2$ h, at $T = 32.2$ h, at $T = 44.2$ h and at $T = 67.2$ h, where the oil lens is floating above the groundwater level at approximately 20.8 cm, 18.3 cm, 16.1 cm, 16.1 cm and 15.8 cm from the bottom. The groundwater level is situated
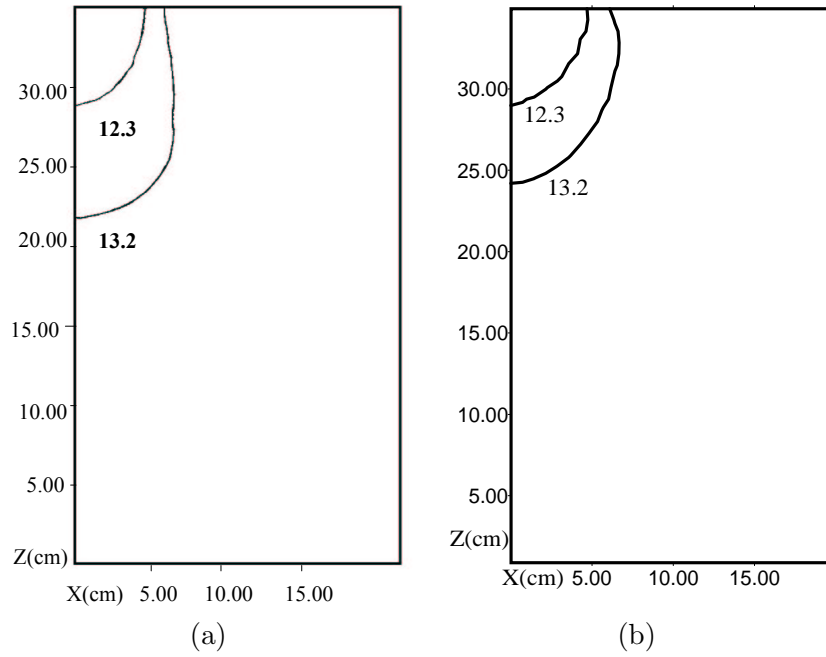
Figure 3.4: Fluctuation Case: the oil front at times T=12.3 h and T=13.2 h The oil front is defined by $S_o = 0.02$ (numerical) and visually (experiment). The groundwater level is not yet reached. (a) experimental results and (b) numerical results.
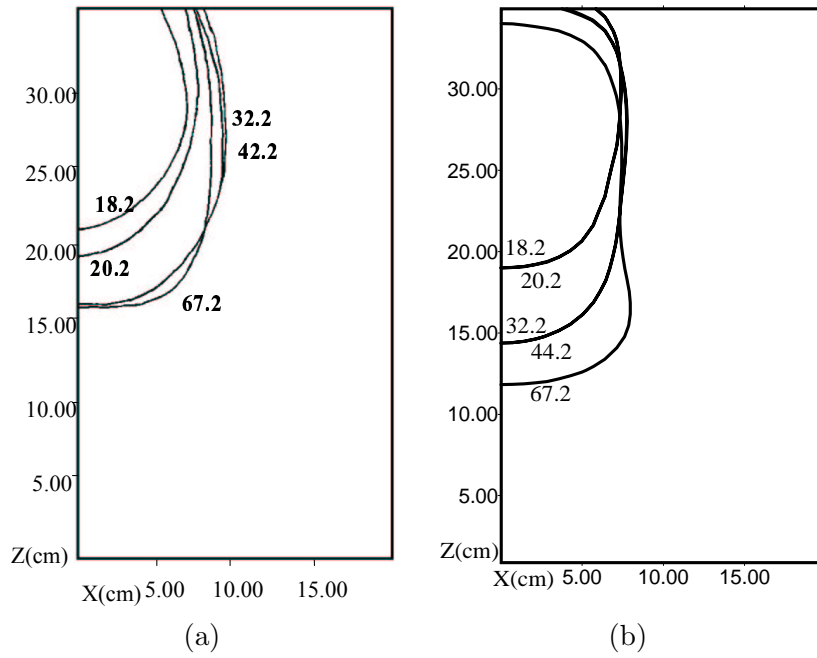
Figure 3.5: Fluctuation case: the oil front at T=18.2 h, T=20.2 h, T=13.2 h, T=44.2 h and T=67.2 h. (a) experimental results and (b) numerical results.
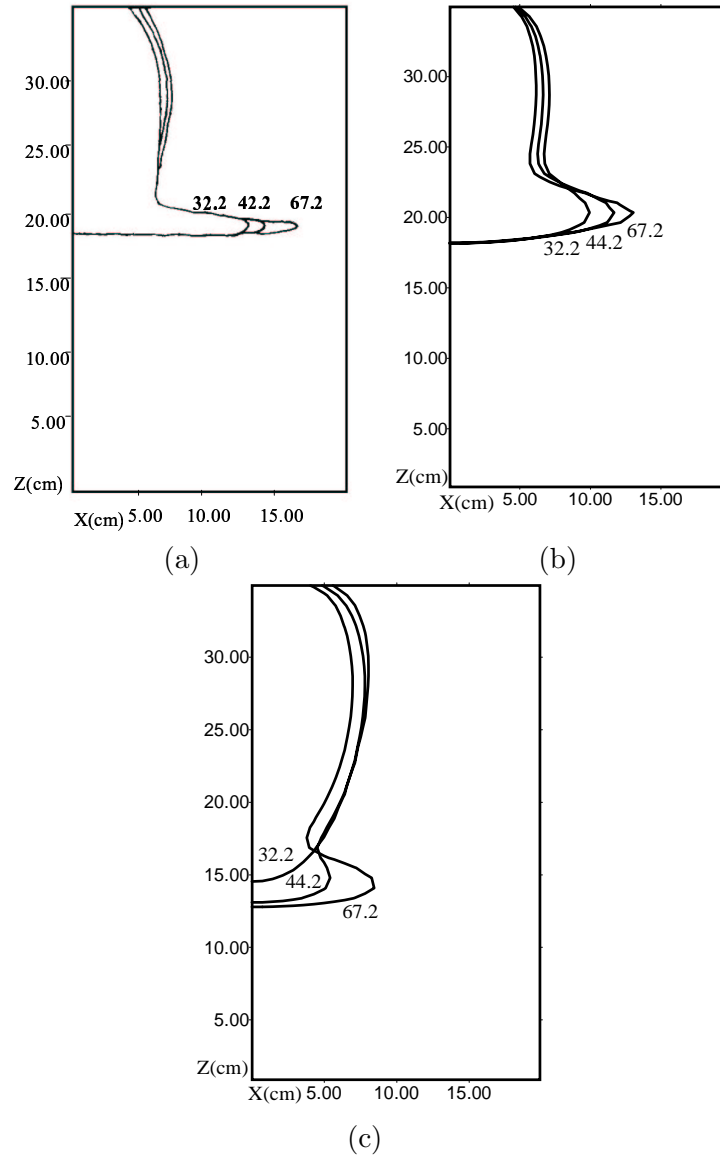
Figure 3.6: Reference case: the oil front at T=32.2 h, T=42.2 h and T=67.2 h. (a) experimental results (b) numerical results with increased waterlevel (c) original numerical results.

at respectively $Z = 10$ cm, $Z = 12$ cm, $Z = 2$ cm, $Z = 12$ cm and at $Z = 11.5$ cm (Figure 3.3). From Figure 3.3 it is known that from $T = 20.2$ h, the fluctuations are incorporated which means that the contour line at $T = 18.2$ h is derived from the stable situation previous to the fluctuations. The maximum width of the oil lens (at $T = 44.2$ h) is 9.4 cm, measured perpendicular to the symmetry axis.

Figure 3.6.a shows the oil front for the reference case, where the groundwater level remains at $Z = 10$ cm, solely at the moments in time $T = 32.2$ h, at $T = 44.2$ h and at $T = 67.2$ h, since the development of the oil lens in the reference case and the fluctuation case is identical before the fluctuations are incorporated, i.e. before $T = 20.2$ h. A number of experiments showed the reproducibility of this experiment before the water level is reached. The maximum depth that is reached by the oil front is 18.6 cm. The maximum spreading in the horizontal direction is 16.5 cm.

3.4.2   Numerical results

We again considered the two-dimensional problem where we distinguish between a reference case where the oil accumulates above a stationary groundwater level and between a fluctuation case where the groundwater level fluctuates as a function of time. In Figure 3.4.b and Figure 3.5.b, the results for the fluctuation case are shown, where again the parameter values described in Table 3.2 are used. We again resolved the oil front which is determined by an oil saturation contour line of 0.02. During the first 20.2 h the results are the same as in the reference case. The depth reached by the oil front at $T = 12.3$ h and $T = 13.2$ h (Figure 3.5.b) are respectively approximately 29.1 cm and 24.5 cm from the bottom of the model. In Figure 3.5.b the oil front has reached respectively 19.2 cm, 14.6 cm, and 11.9 cm at $T = 18.2$ h, $T = 32.2$ h and $T = 67.2$ h. The oil front does not spread as a lens on top of the capillary fringe. The results of the reference case where the parameters described in Table 3.2 are used, are shown in Figure 3.6.b, where we see the redistribution of oil above the groundwater level. The results before $T = 18.2$ h are not shown for the reference case, since they are the same as for the fluctuation case, which indicates reproducibility. After 20 h, the oil has reached the groundwater level ($\pm$ 0.16 m) and migrates horizontally after that moment. The maximum depth of the oil lens is 18.2 cm from the bottom of the model and the maximum horizontal spreading is 13.1 cm. Figure 3.6.c shows the result if the water level was not increased from 10 cm to 16 cm.

3.5 Discussion

Comparison of the experimental and numerical results (Figure 3.4-3.6 and Table 3.3) leads to the following: Comparison between Figure 3.4.a and Figure 3.4.b and between Figure 3.6.a and Figure 3.6.b are used to assess whether the variables chosen in the numerical code are correct or not. The reasonable good agreement between Figure 3.4.a and Figure 3.4.b and the good agreement between Figure 3.6.a and Figure 3.6.b confirms that correct parameter values are used (see Table 3.2). The good results show that the Van Dam approximation [43] does not give a unique solution since we have optimized for 2 parameters only and achieve comparable results (see Figure 3.2) as Wipfler et al. [53]. As is apparent from the discrepancies between the optimized curves and the experimental data of Figure 3.2, the inverse model [43] does not fit well enough to capture the strong curves of the data. The detail that may have been missed this way could well be responsible for smaller discrepancies between numerical and experimental results (for instance the oil thickness in Figure 3.6). Hence, we conclude that for the present purpose of a detailed comparison of experimental and numerical three phase flow, the parameterization is still a weak point if standard methods are used.

The water level in the numerical experiment was increased by 6 cm to account for the small heterogeneities that occur in the experimental set up. This shows the large impact of spatial variability of hydraulic properties, as the porous medium was not designed to be heterogeneous. Apparently it is difficult to establish a homogeneous model in the laboratory and even more difficult to find a homogeneous field site. This is in agreement with results from Essaid et al. [9], who measured distributions of oil at a field site in Minnesota, USA. They concluded that the LNAPL redistribution could not be numerically reproduced without including heterogeneities, fluid entrapment, saturation hysteresis and water table fluctuations. Furthermore Glass et al. [11] performed a laboratory 2-D homogeneous experiment and they also mentioned that heterogeneity is almost inevitable.

It may be worthwhile to observe that trial simulations that combine different combinations of parameter values from the realistic ranges of S_w^{min}, α, and n did not explain the shallow depth of the oil lens of Figure 3.6(a). Among others for this reason, the groundwater level was adjusted in the simulations. After this adjustment, the results are in close agreement except for some deviations. The most important deviations are the penetration depth in Figure 3.5.a and 3.5.b, and the thickness of the accumulating lens

in Figure 3.6.a and 3.6.b. There can be several reasons for these discrepancies: the oil lens front geometry is defined by visually inspecting where the red dye is not visible to the human eye anymore. In the numerical approach the $S_o = 0.02$ contour was used to define this front. Furthermore, the numerical model assumes that there is no residual oil in the unsaturated zone, which is in contradiction with experimental observations (Wipfler and van der Zee [52]). The discrepancies are probably caused also by the heterogeneity in the experimental set up that made adjustment of the groundwater level necessary.

The development of the oil lens during a fluctuation is as follows: rising of the groundwater level causes entrapment of the oil phase in the water phase(i.e. discrete drops of oil become enclosed by water) which results in immobilization of the oil phase. Lowering, however, causes the oil to become a mobile phase again. During the immobilization the oil is not able to migrate in the horizontal direction. Retardation in horizontal migration for both numerical and experimental results is obvious from Figures 3.5.a and 3.6.a and Figures 3.5.b and 3.6.b and from Table 3.3. Both numerically and experimentally, there is no spreading at all in the fluctuation case whereas in the reference case the maximum spreading is 13.1 cm (numerically) and 16.5 cm (experimentally).

Notation

A	the amplitude of the fluctuation
D	parameter determining finiteness of lens thickness
F_L	Land's factor
g	gravity [$\mathrm{m\,s^{-2}}$]
G	flux area [$\mathrm{m^2}$]
H	hydraulic head [m]
$h\,(\tilde{h})$	(scaled) similarity profile
K	absolute permeability [$\mathrm{m^2}$]
K_{hc}	hydraulic conductivity [m/s]
k_{ri}	phase i relative permeability
n, m	van Genuchten parameter
$P_i(p_i)$	(dimensionless) phase i pressure [Pa]
P_c	charateristic pressure [Pa]
P_{ik}	phases i, k capillary pressure [Pa]

Q_w	water flux [m^3/s]
S_i	phase i saturation
S_{of}	free oil saturation
S_{ot}	trapped oil saturation
S_{or}^{max}	maximum residual oil saturation
S_t	total fluid saturation
S_{wa}	apparent water saturation
S_w^{min}	minimum water saturation
$T(t)$	(dimensionless) time [h]
T_c	characteristic time [hours]
t_0	starting time of similarity solution
$\bar{t}$	time in similarity solution
U_i	phase i horizontal flow velocity [m s^{-1}]
V_i	phase i vertical flow velocity [m s^{-1}]
V_1	initial oil volume [m^3]
w_f	dimensionless free oil volume per unit lateral area [m]
$X(x)$	(dimensionless) horizontal coordinate [m]
X_c	characteristic horizontal length [m]
$Z(z)$	(dimensionless) vertical coordinate [m]
Z_c	characteristic vertical length [m]
$Z_{ao}(z_{ao})$	(dimensionless) elevation beyond which air is present [m]
$Z_{ow}(z_{ow})$	(dimensionless) elevation beyond which oil is present [m]
α	van Genuchten parameter [m^{-1}]
β_{ao}, β_{ow}	ratios of air-oil and oil-water to air-water surface tensions
γ	dimensionless parameter in nonlinear diffusion equation
η	similarity variable
μ, ν	powers in similarity solution
μ_i	phase i viscosity [Pa s]
ρ_i	phase i density [kg m^{-3}]
τ	part of the actual simulated time in which the LNAPL can spread horizontally: flow time
ϕ	porosity
ω	angular velocity of the fluctuation

Chapter 4

An application of three phase percolation theory to describe the behavior of an LNAPL spill*

4.1 Introduction

Light Non Aqueous Phase Liquids (LNAPL) can flow into the subsurface and contaminate an aquifer in such a way, that it will be a threat to the quality of drinking water supplies. A large amount of the contamination can be removed from the soil by pumping, except for the immobile oil that is entrapped by the water phase. This small amount of contamination can still pollute large amounts of drinking water and consequently forms a threat to our drinking water supplies. An important issue in remediation of such a contaminated aquifer, is to obtain knowledge about the amount of entrapped LNAPL. Physical phenomena such as a fluctuating groundwater level or rainfall infiltration have a large impact on the entrapment of LNAPL in the water phase: oil can be trapped as immobile droplets into the water phase in a porous medium predominantly saturated with water. Through the relative permeabilities of the present phases, it is possible to predict the mobility and thus the amount of entrapment of the LNAPL. Henceforth, we use the term oil as a comprehensive term for LNAPL.

In earlier work, Stauffer [41], Sahimi [39], Heiba [13] and Yortsos et al. [54] used percolation theory to describe the relative permeabilities of two immiscible fluids in a porous medium. Sahimi [39] concluded that percolation theory has given a much deeper understanding of two-phase flow in porous media and especially of the macroscopic connectivity of a fluid phase. Heiba [13] presented an extensive explanation of how this specific pore-network theory works and how it can be adapted to a porous
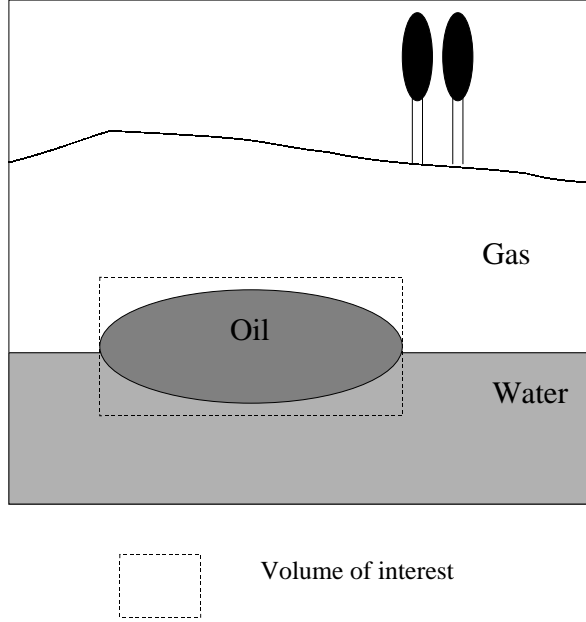
Figure 4.1: The three phase system that is considered. The dashed square shows the volume of interest for this work. The subdomains represent the areas where one phase dominates whereas all three phases are present in each subdomain.

medium like the subsurface. Bartelds [3][4] used percolation theory for a semi-three phase system, namely, water, oil and water with polymer gel. It is shown that percolation theory can describe the effects of drainage and imbibition on the relative permeabilities and that the theory is capable of predicting the experimentally and numerically observed trends in two-phase relative permeabilities of systems in which one phase is strongly wetting. For a more detailed description of the basic principles of percolation theory, we refer to Stauffer [41], Sahimi [39][38] and Heiba [13].

Since the oil is lighter than water and floats above the capillary fringe in the subsurface, we also deal with a three-phase problem that involves water, oil and air (see Figure 4.1). The volume of interest is shown in this Figure. The competition among these three phases for the individual segments of the porespace determines for instance the relative permeability. We assume that water is the wetting phase, gas is the non-wetting phase and oil is the intermediate wetting phase. This means that in the situation where three

phases are present, gas and water are everywhere shielded from each other by the oil phase. Mani and Mohanty [32] already investigated the situation where three phases are initially present. This model combines a description of pore space morphological features and three-phase displacement physics to model capillary controlled gas invasion into a water-wet medium containing oil and water. Heiba [13] also extended two-phase percolation theory to three-phase percolation theory. He studied two specific cases: 1. gas and water are displacing oil (imbibition where water displaces oil; drainage where gas displaces oil) and 2. water is displacing oil and oil is displacing gas (imbibition). He concluded that the theory for two-phases can be successfully extended to three phase flow for these two specific cases. In reality it is not common to have initially a three phase system and therefore it is necessary to simulate a three phase problem where contamination flows into the subsurface (two-phase system where water and gas coexist). This means that it is necessary to simulate iterative processes of drainage and imbibition (where oil enters the domain) to include all phases in the model.

In this work, we applied the ideas of Heiba for three-phase percolation theory and we simulate a succession of imbibition and drainage processes to obtain the complete range of compositions of a three phase system, where oil is the shielding phase between water and gas. How a three phase system can be used for complex situations where water will infiltrate from different directions into an oil lens will be left for future work. By expanding this theory to a three phase system, it is a useful instrument for predicting the relative permeabilities of oil contamination in the unsaturated zone. We build on the code that Heiba [13] developed for a two-phase system and we extend it to a three-phase system.

4.2 Elements of percolation theory

Percolation theory can be used to improve our understanding of relative permeability and capillary pressure curves in porous media. It enables us to assess whether a fluid is macroscopically connected or not. The macroscopic connectivity is of fundamental importance involving flow in porous media for recovery or remediation purposes. The basic concept of this theory is to statistically describe the probability that a porespace is accessible for a wetting or non-wetting fluid. Percolation theory is defined as the generation of a continuous path of connectedness, and thus of transport, through a
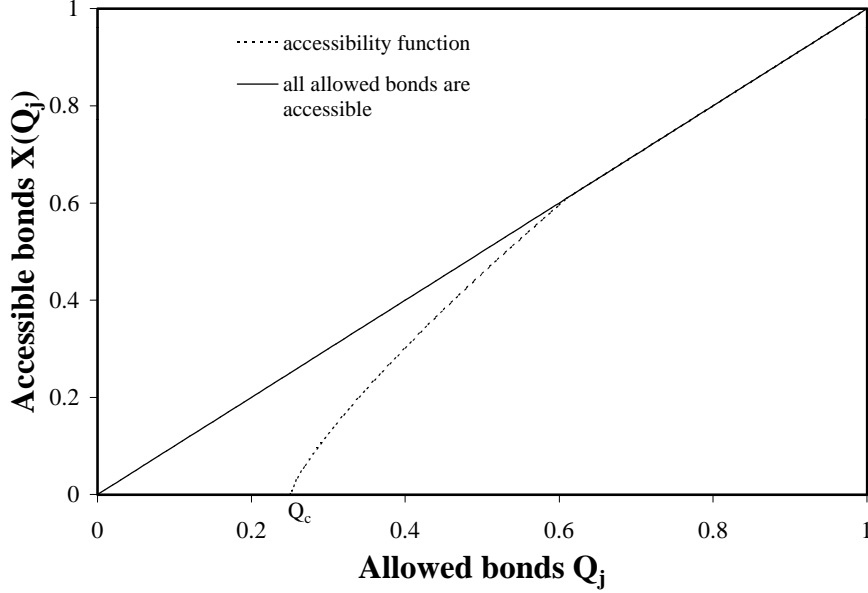
Figure 4.2: Example of accessibility function $X(Q_j)$ as a function of allowability Q_j for phase j. Q_c is the percolation threshold.

random set of different bonds and sites of a network. This network consist of bonds and nodes. Percolation theory simplifies the network by assuming that all the properties of the porespace are assigned to the bonds whereas the nodes are zero-dimensional markers for branching. The coordination number z is defined as the average number of bonds that originate from one node. The bonds are assumed to be capillary cylindrical tubes with various radii.

To treat the network in a statistical way, we represent all the bonds of the network by a number fraction function. The number fraction $\psi(R)$ of bonds with a radius in between R and $R + dR$ is described as a function of R. This can be for example a Rayleigh distribution or a Gamma distribution. Some definitions that are used in percolation theory are as follows: Bonds above a certain radius are *allowed* for oil due to the capillary effects. This means that a phase can enter a pore bond with radius R if the capillary pressure exceeds the accompanying capillary pressure of this bond: $P_c = \frac{2\sigma}{R}$, where σ is the interfacial tension. The *accessible* fraction is the fraction of bonds connected to some continuous path across the network,

i.e. accessible means that both the bonds are allowed by the phase, and the surrounding bonds will not inhibit the fluid to invade. *Occupied* means that the bonds are actually occupied by that phase. The *percolation threshold* is the largest fraction of allowed bonds below which the accessible fraction, and thus the equivalent conductivity, is zero. The *accessibility function* is the relation between the allowed fraction of bonds for a certain phase j and the fraction of bonds that is accessible to that phase. An example of a common accessibility function that will be used later in this chapter is shown in Figure 4.2. The horizontal axis shows the allowed pore fraction Q_j and the vertical axis shows the accessible fraction $X^A(Q_j)$. This figure reveals that the allowed fraction must be larger than the percolation threshold Q_c to become accessible for phase j:

$$X^A(Q_j) = \begin{cases} 0 & , Q_j \leq Q_c \\ Q_j & , if \ Q_j \to 1 \end{cases} \tag{4.1}$$

The straight line shows the accessibility function when all the allowed radii would be accessible. The model that corresponds with this straight line is also referred to as the capillary bundle model.

4.3 Model equations

The ultimate goal of this study is to investigate the effects of water infiltration into an oil lens that floats at the capillary fringe. To simulate this infiltration, a sequence of drainage and imbibition processes will be calculated and these processes will be described in this chapter in the following chronological order of appearance. The initial situation is a completely water saturated domain. During primary drainage, gas enters the domain and the unsaturated zone develops. If then a finite amount of oil enters the two-dimensional domain by displacing the gas phase (primary imbibition), a three phase system is obtained. Secondary imbibition occurs during water infiltration, where water displaces the oil phase. Finally, secondary drainage occurs where gas displaces water. The processes of drainage as well as the processes of imbibition continue until a connate saturation is reached where the phase that is receding has become immobile. This means that the whole range of pore radii that are enterable by one of the three phases is comprehended in this study. Furthermore this implies that only two of the three phases are above its connate saturation and thus only two phases are flowing. The connate wetting phase occupies the smallest pores,
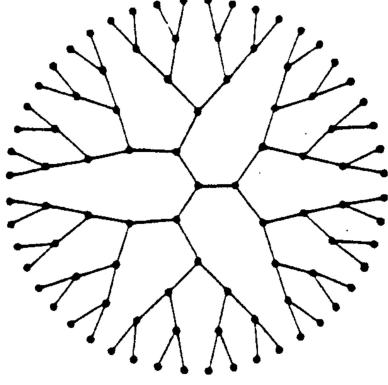
Figure 4.3: The Bethe tree.

the connate non-wetting phase occupies the largest pores and the connate intermediate wetting phase can occupy all the pores in between. Consequently, all three phases are never present in one pore throat at the same time. Because of their wettability, the water and gas phase are shielded from each other by the oil phase.

The pore space is represented by the Bethe tree (see Figure 4.3). This pore space is completely characterized by the variable local coordination number z, i.e. the number of bonds that join at each node. In previous research [40], it is shown that the Bethe tree remarkably well predicts the bond accessibility and equivalent conductivity of three-dimensional networks. Another advantage is that expressions have been worked out theoretically for the accessibility function X^A and for the effective network conductivity. The accessibility function for a Bethe tree with coordination number z according to Fisher and Essam [10] is given by:

$$X^A(Q_j) = \begin{cases} Q_j[1\text{-}(\frac{Q_j^*}{Q_j})^{\frac{2z\text{-}2}{z\text{-}2}}] & ,Q_c < Q_j \leq 1 \\ 0 & ,Q_j \leq Q_c \end{cases} \quad (4.2)$$

where Q_j^* is the non-trivial root of the equation:

$$Q_j^*(1\text{-}Q_j^*)^{z\text{-}2}\text{-}Q_j(1\text{-}Q_j)^{z\text{-}2} = 0 \quad (4.3)$$

Equation (4.2) is identical to Equation (4.1) for $\lim_{Q_j \to 1} X^A(Q_j)$

	Fraction	Number fraction function
Total		$\psi(R)$
Allowability	Q_j	
Accessibility	X_j^A	
Occupancy	X_j^O	$\psi_j^O(R)$

Table 4.1: The different statistics and notations used to describe the percolation theory.

$(\lim_{Q_j^* \to 0} X^A(Q_j^*))$. The percolation threshold Q_c for a Bethe tree is according to Fisher and Essam [10] and Stinchcombe [42]:

$$Q_c = \frac{1}{z\text{-}1} \tag{4.4}$$

We have chosen to use the Rayleigh distribution to describe the pore size distribution function of bonds since it describes the pore size distribution of a realistic porous medium appropriately. The Rayleigh distribution is given by [13]:

$$\psi(R) = 2Re^{-R^2} \tag{4.5}$$

In the following sections, the allowability and occupancy statistics for the three phases during the two drainage processes and the two imbibition processes will be described. See Table 4.1 for an overview of the different statistics and notations.

To derive the relative permeabilities for the three phases from the accessibility and allowability of the model that can describe the drainage and imbibition process model, it is necessary to calculate the accompanying conductivity. We have chosen to use the conductivity distribution as defined by Stinchcombe [42]:

$$G_j(g) = (1\text{-}Q_j)\delta(g) + Q_j\psi_j^a(R)\left|\frac{dR}{dg}\right| \tag{4.6}$$

where G_j is the phase conductivity function of phase j, $\delta(g)$ is Dirac delta function and g is the conductivity of a bond. To account for the percolation threshold, we replaced Q_j in Equation (4.6) by $X^A(Q_j)$ to account for the percolation threshold. Earlier work by Heiba [13] and Bartelds [3] included Q_j instead of $X^A(Q_j)$, so that the effect of the percolation threshold is neglected in the calculations of their relative permeabilities.

Using this conductivity equation and the allowability statistics, the relative permeability is calculated. The relative permeability is the ratio of the effective conductivity of a specific phase by the effective conductivity of all the bonds. The effective conductivity is, as defined by Stinchcombe [42]:

$$\theta_j = \text{-}zC'(0) \tag{4.7}$$

where $C(x)$ is a generating function, the Laplace transformation of which is defined by the nonlinear integral equation:

$$\int_0^\infty e^{\text{-}tx}C(x)dx = \int_0^\infty dgG_j(g) \cdot [\frac{1}{t+g}$$
$$+ \frac{g^2}{(t+g)^2}\int_0^\infty exp[\text{-}\frac{gtx}{g+t}[C(x)]^{z\text{-}1}dx] \tag{4.8}$$

subject to the boundary condition $C(0) = 1$. t is the Laplace transformation variable. For more details about the derivation of these conductivity and relative permeability equations, we refer to Heiba [13], Bartelds [3] and Stinchcombe [42]. In the next paragraphs the processes of primary drainage, primary imbibition, secondary imbibition and secondary drainage will be described.

4.3.1 Primary drainage

In the initial situation, the domain is completely saturated with the wetting fluid water, prior to migration of gas (air, the non-wetting 'fluid') into the domain. This is shown in Figure 4.4. $R_{\max}$ is the maximum radius in the network model and $R_{\min}$ is the minimum radius in the network model. For a Rayleigh distribution $R_{\max}$ is ∞ and $R_{\min}$ is 0. Initially all the bonds are allowed to and occupied by water:

$$Q_{w,d}^{ini} = X_{w,d}^{O,ini} = 1 \tag{4.9}$$

$$\psi_{w,d}^{O,ini}(R) = \psi(R) \tag{4.10}$$

where the subscripts d means drainage and w means water. X^O is the occupied pore fraction. The superscript ini means initial and O means occupied. Equation (4.9) and (4.10) imply that initially before the drainage
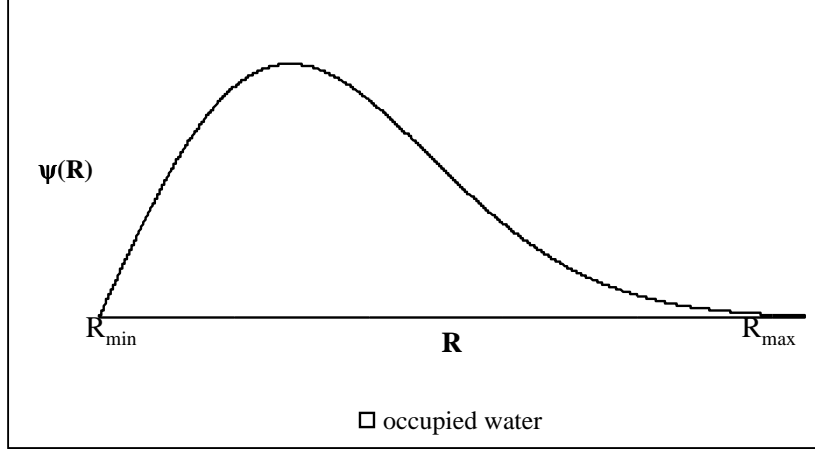
Figure 4.4: The total number fraction $\psi(R)$ as a function of the radius R where all the pore throats are filled with water.

process starts, all the pores are allowed and occupied by water. Equation (4.10) is graphically shown in Figure 4.4 where the complete number fraction function $\psi(R)$ is allowed for and occupied by water. For the gas phase, which is initially not present in the domain, (4.9) and (4.10) imply:

$$Q_{g,d}^{ini} = X_{g,d}^{O,ini} = 0 \tag{4.11}$$

$$\psi_{g,d}^{O,ini}(R) = 0 \tag{4.12}$$

where the subscript g means gas.

The key parameter characterizing this process is provided by the radius of the smallest bond that the invading gas can enter at a capillary pressure of $P_c = \frac{2\sigma_{wg}}{R}$, where σ_{wg} is the interfacial tension between water and gas: during drainage P_c increases and consequently R decreases (see Figure 4.5.a). The accompanying drainage radius is called R_d. All the bonds that are larger than R_d are potentially allowed for gas (see Figure 4.5.a). The resulting allowability equation for gas during drainage is as follows:

$$Q_{g,d} = \int_{R_d}^{R_{\max}} \psi(R)dR \tag{4.13}$$

where $Q_{g,d}$ is the number fraction of bonds allowed to the gas phase. As R_d decreases, more of the pore space becomes allowed and accessible for
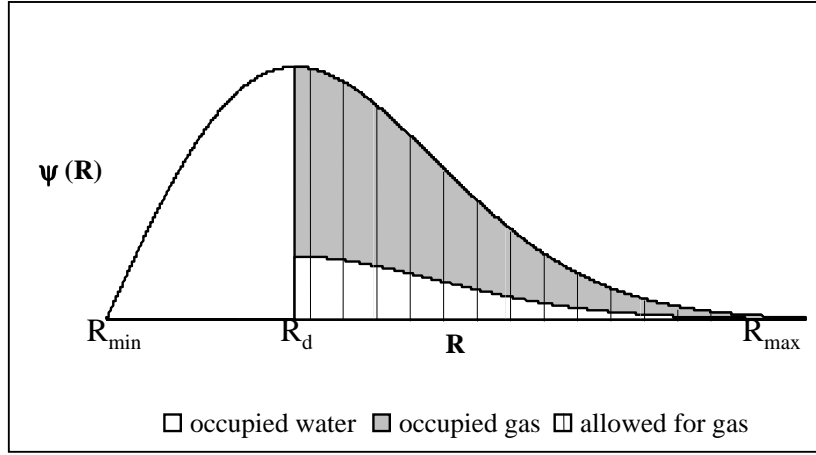
(a)
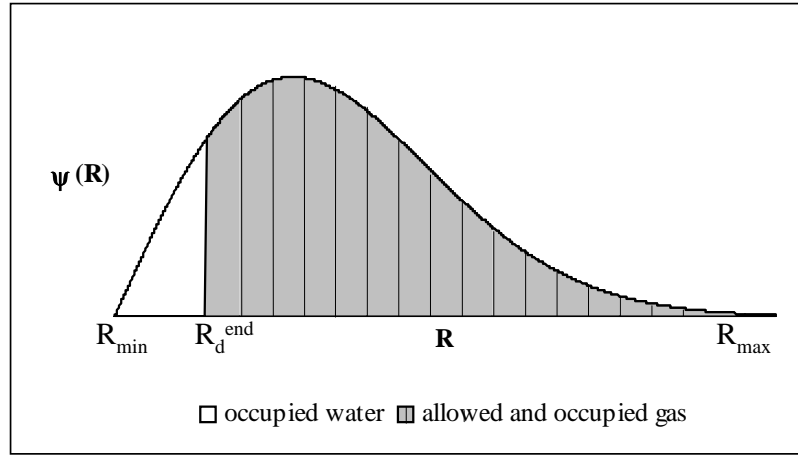
(b)

Figure 4.5: Number fraction functions of pore throat radii and the occupied and allowed fractions for gas and water described by the drainage radius R_d, R_d^{end} is the limiting pore radius. a. during primary drainage. b. at the end of the drainage process.

gas.

The fraction of bonds occupied by gas consists of one term that is proportional to the fraction of allowed bonds that are also accessible ($\frac{X^A(Q_{g,d})}{Q_{g,d}}$), where $X^A(Q_{g,d})$ is the accessible pore fraction, plus one term which contains the bond fraction previously containing gas (which is zero in this case). $\psi(R)$ is multiplied by $\frac{1}{X^O_{g,d}}$ to normalize the fraction number function. This means that the occupied and accessible fraction may overlap. Furthermore, in this case, the occupied pore-size distribution function is identical to the allowed pore-size distribution function. The occupancy equations (the fractions that will actually be filled by gas) are:

$$X^O_{g,d} = X^A(Q_{g,d}) \tag{4.14}$$

$$\psi^O_{g,d}(R) = \begin{cases} 0 & , R_{\min} \leq R < R_d \\ \psi(R)\frac{X^A_{g,d}}{Q_{g,d}}\frac{1}{X^O_{g,d}} = \frac{\psi(R)}{Q_{g,d}} & , R_d \leq R \leq R_{\max} \end{cases} \tag{4.15}$$

where $X^O_{g,d}$ is the number fraction of bonds that become occupied by gas during primary drainage and $\psi^O_{g,d}(R)$ is their distribution of radii. The allowability and occupancy equations for water are:

$$Q_{w,d} = X^O_{w,d} = 1\text{-}X^A(Q_{g,d}) \tag{4.16}$$

$$\psi^O_{w,d}(R) = \begin{cases} \frac{\psi(R)}{Q_{w,d}} & , R_{\min} \leq R < R_d \\ \frac{\psi(R)}{Q_{w,d}}[1\text{-}\frac{X^A(Q_{g,d})}{Q_{g,d}}] & , R_d \leq R \leq R_{\max} \end{cases} \tag{4.17}$$

where again $\psi(R)$ is divided by $Q_{w,d}$ for normalization purposes.

This process continues until R_d reaches the limiting value R^{end}_d (Figure 4.5.b), below which no further drainage can occur, since the connate water saturation is attained and no further flow of water is possible.

Comparing Figure 4.5.a and 4.5.b shows that at low capillary pressures, i.e. when the limiting pore radius R_d is large, the pores with $R \geq R_d$ that become occupied by gas form a comparatively small subset of all pores with $R \geq R_d$, whereas at high capillary pressures, i.e. when R_d is small, the gas phase comes to occupy nearly all pores with $R \geq R_d$. This is a consequence of the trend indicated in Equation (4.2) (Figure 4.2), where

we see that when $Q_{g,d}^{end}$ becomes much larger than Q_c, the accessible fraction $(X^A(Q_{g,d}^{end}))$ tends to the allowed fraction $(Q_{g,d}^{end})$.

The consequence of the increasing amount of the gas phase is a decrease of the amount of the water phase and eventually $Q_{w,d}$ becomes smaller than the percolation threshold Q_c. The accompanying radius R_d^{end} where $Q_{w,d}^{end} = Q_c$ can be calculated from:

$$Q_{w,d}^{end} = 1\text{-}X^A(Q_{g,d}^{end}) = 1\text{-}X^A(\int_{R_d^{end}}^{R_{\max}} \psi(R)dR) = Q_c \qquad (4.18)$$

where the superscript *end* denotes the end situation of this drainage process.

The resulting allowability and occupancy equations for gas are:

$$Q_{g,d}^{end} = X_{g,d}^{O,end} = \int_{R_d^{end}}^{R_{\max}} \psi(R)dR \qquad (4.19)$$

$$\psi_{g,d}^{O,end}(R) = \begin{cases} 0 & , R_{\min} \leq R < R_d^{end} \\ \frac{\psi(R)}{Q_{g,d}^{end}} & , R_d^{end} \leq R \leq R_{\max} \end{cases} \qquad (4.20)$$

where all the bonds that are allowed for gas are also accessible for gas and occupied by it. For water the final allowability and occupancy equations are Equation (4.18) and:

$$\psi_{w,d}^{O,end}(R) = \begin{cases} \frac{\psi(R)}{Q_{w,d}^{end}} & , R_{\min} \leq R < R_d^{end} \\ 0 & , R_d^{end} \leq R \leq R_{\max} \end{cases} \qquad (4.21)$$

The water saturation during this process is as follows related to the pore radius R_d:

$$S_w = 1\text{-}\frac{X^A(Q_{g,d})}{Q_{g,d}} \frac{\int_{R_d}^{R_{\max}} \psi(R)v(R)dR}{\int_{R_{\min}}^{R_{\max}} \psi(R)v(R)dR} \qquad (4.22)$$

where $v(R)$ is the volume of a bond as a function of the radius $(v(R) = R^n)$, $0 \leq n \leq 2$. At the end of the primary drainage process the connate water saturation is:

$$S_{wc} = \frac{\int_{R_{\min}}^{R_d^{end}} \psi(R)v(R)dR}{\int_{R_{\min}}^{R_{\max}} \psi(R)v(R)dR} \qquad (4.23)$$

The corresponding gas saturation S_g follows from $S_w + S_g = 1$. The saturation parameters are the input parameters in the code and are used to calculate the accompanying radii.

4.3.2 Primary imbibition

In the second process, the oil phase will enter the network model. Since oil is the non-wetting phase towards the water phase and the wetting phase towards the gas phase, it will displace the gas phase. Oil will enter in the radii that are bigger than the ones occupied by the water phase, but smaller than the ones occupied by the gas phase (see Figure 4.6.a). This process is called imbibition since oil (the wetting phase) displaces gas (the non-wetting phase). The displacement of gas instead of water can be explained by comparing the phase entry pressures between the situation where oil displaces water and the situation where oil displaces gas (see also Van Dijke et al. [45]).

When oil displaces water, the capillary pressure is:

$$P_{c,ow} = \frac{2\sigma_{ow}}{R} \tag{4.24}$$

so that the entry pressure for oil is:

$$P_o^{in} = P_w + P_{c,ow} = P_w + \frac{2\sigma_{ow}}{R} \tag{4.25}$$

When oil displaces gas, the capillary pressure is:

$$P_{c,go} = \frac{2\sigma_{go}cos\theta_{go}}{R} \tag{4.26}$$

where

$$cos\theta_{go} = \frac{\sigma_{gw}\text{-}\sigma_{ow}}{\sigma_{go}} \tag{4.27}$$

so that the entry pressure for oil is:

$$P_o^{in} = P_g\text{-}P_{c,go} = P_w + \frac{2\sigma_{gw}}{R_{gw}} + \frac{2(\sigma_{ow}\text{-}\sigma_{gw})}{R} \tag{4.28}$$

where R_{gw} is the radius that separates the water and gas phase at the beginning of the primary imbibition process and where the oil will enter (in this case $R_{gw} = R_d^{end}$). Comparing Equations (4.25) and (4.28) shows that
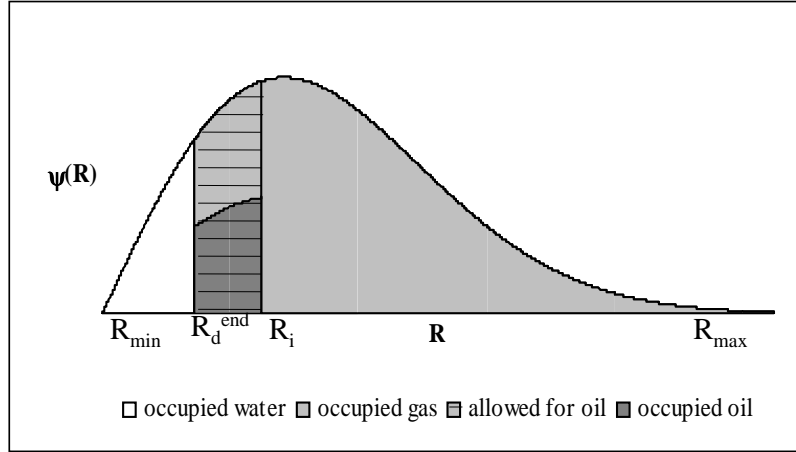
(a)
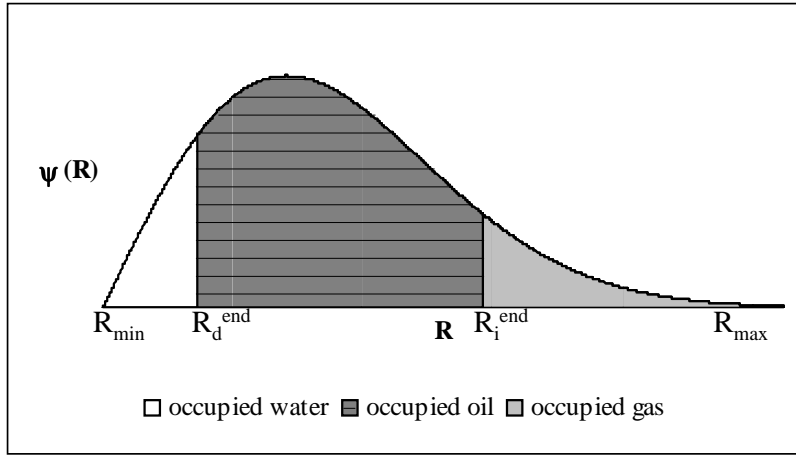
(b)

Figure 4.6: Number fraction functions of pore throat radii and the occupied and allowed fractions for gas and oil described by the imbibition radius R_i, R_i^{end} is the limiting pore radius for imbibition. a. during primary imbibition. b. at the end of the primary imbibition process.

oil will displace the gas phase and not the water phase: initially Equations (4.25) and (4.28) are identical. Next P_o^{in} where oil displaces gas will increase slower than P_o^{in} where oil displaces water and therefore oil will displace the gas phase.

The initial conditions for water remain the same as the water conditions at the end of the primary drainage process (see Equation (4.18) and Equation (4.21)). The accompanying imbibition radius is called R_i. All the bonds that are larger than R_d^{end} and smaller than R_i will be allowed for oil. The occupancy statistics for oil are obtained by defining the pores with $R_d^{end} \leq R < R_i$ that formerly contained gas, in the proportion $\frac{X^A(Q_{o,i})}{Q_{o,i}}$. The resulting allowability and occupancy equations for oil during imbibition are as follows:

$$Q_{o,i} = \int_{R_d^{end}}^{R_i} \psi(R)dR \tag{4.29}$$

$$X_{o,i}^O = X^A(Q_{o,i}) \tag{4.30}$$

$$\psi_{o,i}^O(R) = \begin{cases} 0 & , R_{\min} \leq R \leq R_d^{end} \\ \frac{\psi(R)}{X_{o,i}^O} \frac{X_{o,i}^A(Q_{o,i})}{Q_{o,i}} & , R_d^{end} < R \leq R_i \\ 0 & , R_i < R \leq R_{\max} \end{cases} \tag{4.31}$$

where the subscript o denotes the oil phase.

The gas phase previously filled the pore throats between R_d^{end} and $R_{\max}$, while the pore throats between R_d^{end} and R_i are now allowed to be filled by oil. The allowability and occupancy equations for gas are:

$$Q_{g,i} = X_{g,i}^O = \int_{R_d^{end}}^{R_{\max}} \psi(R)dR - \frac{X^A(Q_{o,i})}{Q_{0,i}} \int_{R_d^{end}}^{R_i^{end}} \psi(R)dR \tag{4.32}$$

$$\psi_{g,i}^O(R) = \begin{cases} 0 & , R_{\min} \leq R < R_d^{end} \\ \frac{\psi(R)}{Q_{g,i}}[1 - \frac{X^A(Q_{o,i})}{Q_{o,i}}] & , R_d^{end} \leq R < R_i \\ \frac{\psi(R)}{Q_{g,i}} & , R_i \leq R \leq R_{\max} \end{cases} \tag{4.33}$$

The occupancy equations for gas are the allowability equations for gas, since this is the displaced phase. The area that was occupied by gas after primary drainage minus the pore throats that are filled with oil during this

primary imbibition process are allowed for gas and occupied by gas. This process continues until the connate gas saturation and the accompanying radius R_i^{end}(see Figure 4.6.b) is reached. This radius can be calculated from:

$$Q_{g,i}^{end} = \int_{R_d^{end}}^{R_{\max}} \psi(R)dR - \frac{X^A(Q_{o,i})}{Q_{0,i}} \int_{R_d^{end}}^{R_i^{end}} \psi(R)dR = Q_c \qquad (4.34)$$

We assume that $Q_{o,i}^{end}$ is so much larger than Q_c, that the accessible fraction $(X^A(Q_{o,i}^{end}))$ becomes equal to the allowable fraction $(Q_{o,i}^{end})$(see Figure 4.2). Therefore the resulting final allowability and occupancy equations for water, oil and gas at the end of primary imbibition (see Figure 4.6.b) are:

$$Q_{w,i}^{end} = X_{w,i}^{O,end} = \int_{R_{\min}}^{R_d^{end}} \psi(R)dR \qquad (4.35)$$

$$\psi_{w,i}^{O,end}(R) = \begin{cases} \frac{\psi(R)}{Q_{w,i}^{end}} & , R_{\min} \leq R < R_d^{end} \\ 0 & , R_d^{end} \leq R \leq R_{\max} \end{cases} \qquad (4.36)$$

$$Q_{o,i}^{end} = X_{o,i}^{O,end} = \int_{R_d^{end}}^{R_i^{end}} \psi(R)dR \qquad (4.37)$$

$$\psi_{o,i}^{O,end}(R) = \begin{cases} 0 & , R_{\min} \leq R < R_d^{end} \\ \frac{\psi(R)}{Q_{o,i}^{end}} & , R_i^{end} > R \geq R_d^{end} \\ 0 & , R_i^{end} < R \leq R_{\max} \end{cases} \qquad (4.38)$$

$$Q_{g,i}^{end} = X_{g,i}^{O,end} = \int_{R_i^{end}}^{R_{\max}} \psi(R)dR \qquad (4.39)$$

$$\psi_{g,i}^{O,end}(R) = \begin{cases} 0 & , R_{\min} \leq R < R_i^{end} \\ \frac{\psi(R)}{Q_{g,i}^{end}} & , R_i^{end} \leq R \leq R_{\max} \end{cases} \qquad (4.40)$$

where we see that both the water and gas phase have lost their conductivity and have become immobile phases.

The oil saturation during this process is as follows related to the pore radius R_i:

$$S_o = \frac{X^A(Q_{o,i})}{Q_{o,i}} \frac{\int_{R_d^{end}}^{R_i} \psi(R)v(R)dR}{\int_{R_{\min}}^{R_{\max}} \psi(R)v(R)dR} \qquad (4.41)$$

The corresponding gas saturation is as follows: $S_g = 1\text{-}S_o\text{-}S_{wc}$.

4.3.3 Secondary imbibition

During secondary imbibition, water displaces oil (Figure 4.7.a). Since we assume that the connate gas saturation was reached at the end of the primary imbibition process, the secondary imbibition consists solely of water displacing oil. The radius that controls the imbibition of water displacing oil is called R_{i2}. We are describing controlled imbibition, which implies that water enters pores of increasing radius. The allowability equation for water is:

$$Q_{w,i2} = \int_{R_{\min}}^{R_{i2}} \psi(R)dR \qquad (4.42)$$

Water is allowed to all the pore-segments occupied by water at connate water saturation, i.e. all radii between $R_{\min}$ and R_d^{end}, plus any pore-segment that is accessible between R_d^{end} and R_{i2}. The accompanying occupancy equations for water are:

$$X_{w,i2}^O = \int_{R_{\min}}^{R_d^{end}} \psi(R)dR + \frac{X^A(Q_{w,i2}, X_{w,d}^{O,end})}{Q_{w,i2}} \int_{R_d^{end}}^{R_{i2}} \psi(R)dR \qquad (4.43)$$

$$\psi_{w,i2}^O(R) = \begin{cases} \frac{\psi(R)}{X_{w,i2}^O} & , R_{\min} \leq R < R_d^{end} \\ \frac{\psi(R)}{X_{w,i2}^O} \frac{X^A(Q_{w,i2}, X_{w,d}^{O,end})}{Q_{w,i2}} & , R_d^{end} \leq R < R_{i2} \\ 0 & , R_{i2} \leq R \leq R_{\max} \end{cases} \qquad (4.44)$$

Note that the accessibility for water depends both on the allowability for water and on the occupancy for water at the end of the primary drainage process ($X_{w,d}^{O,end}$). Consequently, the connate water at the end of the primary drainage process is taken into account for the calculation of the accessibility.

The radii that are allowed for oil are those radii that were allowed at the end of the primary imbibition, i.e. all the radii between R_d^{end} and R_i^{end}, minus the radii (between R_d^{end} and R_{i2}) that are enterable by water. The allowability and occupancy equations for oil are:
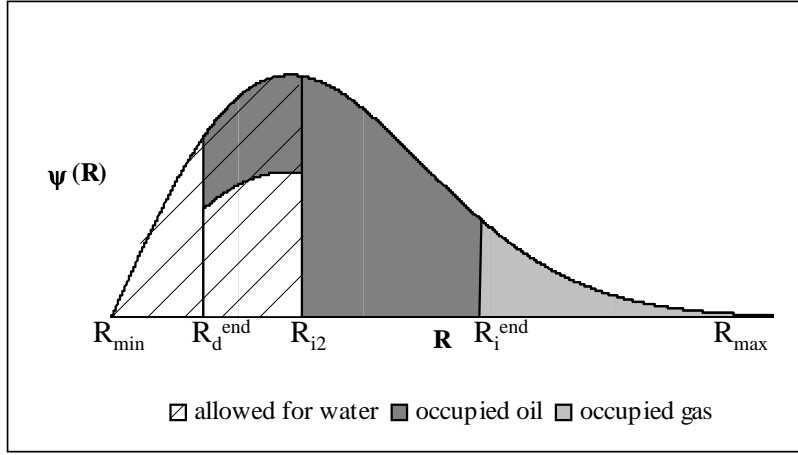
(a)
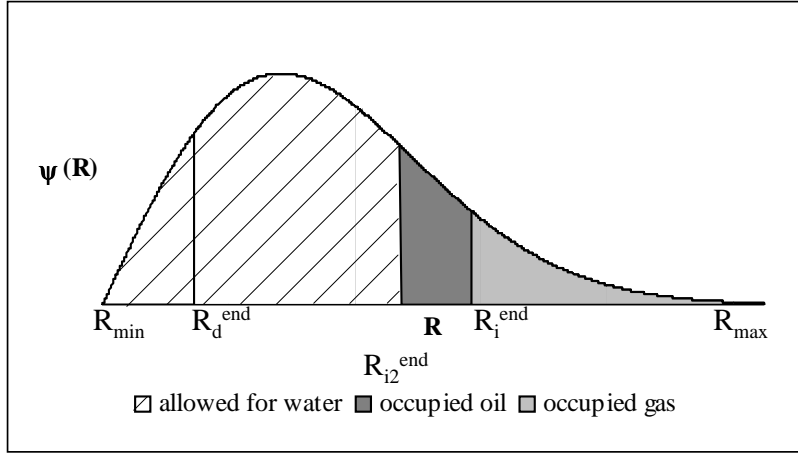
(b)

Figure 4.7: Number fraction functions of pore throat radii and the occupied and allowed fractions for oil and water described by the imbibition radius R_{i2}, R_{i2}^{end} is the limiting pore radius. a. during secondary imbibition. b. at the end of the secondary imbibition process.

$$Q_{o,i2} = X_{o,i2}^O = \int_{R_d^{end}}^{R_{i2}} \psi(R)dR[1\text{-}\frac{X^A(Q_{w,i2})}{Q_{w,i2}}] + \int_{R_{i2}}^{R_i^{end}} \psi(R)dR \quad (4.45)$$

$$\psi_{o,i2}^O(R) = \begin{cases} 0 & , R_{\min} \le R < R_d^{end} \\ \frac{\psi(R)}{Q_{o,i2}}[1\text{-}\frac{X^A(Q_{w,i2})}{Q_{w,i2}}] & , R_d^{end} \le R < R_{i2} \\ \frac{\psi(R)}{Q_{o,i2}} & , R_{i2} \le R < R_i^{end} \\ 0 & , R_i^{end} \le R \le R_{\max} \end{cases} \quad (4.46)$$

The occupancy equations for oil are the same as the allowability equations for oil since it is the displaced phase. The area that was occupied by oil after primary imbibition minus the radii that are filled with water during this secondary imbibition process are allowed for oil and occupied by oil. This process continues until the connate oil saturation is reached: R_{i2}^{end} (see Figure 4.7.b). This radius can be calculated from:

$$Q_{o,i2}^{end} = \int_{R_d^{end}}^{R_i^{end}} \psi(R)dR\text{-}\frac{X^A(Q_{w,i2})}{Q_{w,i2}} \int_{R_d^{end}}^{R_{i2}^{end}} \psi(R)dR = Q_c \quad (4.47)$$

Again we assume that $Q_{w,i2}^{end}$ is so much larger than Q_c so that the accessible fraction $(X^A(Q_{w,i2}^{end}))$ becomes equal to the allowable fraction $(Q_{w,i2}^{end})$(see Figure 4.2).The resulting final allowability and occupancy equations for water, oil and gas (see Figure 4.7.b) are:

$$Q_{w,i2}^{end} = X_{w,i2}^{O,end} = \int_{R_{\min}}^{R_{i2}^{end}} \psi(R)dR \quad (4.48)$$

$$\psi_{w,i2}^{O,end}(R) = \begin{cases} \frac{\psi(R)}{Q_{w,i2}^{end}} & , R_{\min} \le R \le R_{i2}^{end} \\ 0 & , R_{i2}^{end} < R \le R_{\max} \end{cases} \quad (4.49)$$

$$Q_{o,i2}^{end} = X_{o,i2}^{O,end} = \int_{R_{i2}^{end}}^{R_i^{end}} \psi(R)dR \quad (4.50)$$

$$\psi_{o,i2}^{O,end}(R) = \begin{cases} 0 & , R_{\min} \le R \le R_{i2}^{end} \\ \frac{\psi(R)}{Q_{o,i2}^{end}} & , R_{i2}^{end} < R \le R_i^{end} \\ 0 & , R_i^{end} < R \le R_{\max} \end{cases} \quad (4.51)$$

$$Q_{g,i2}^{end} = X_{g,i2}^{O,end} = \int_{R_i^{end}}^{R_{\max}} \psi(R)dR \qquad (4.52)$$

$$\psi_{g,i2}^{O,end} = \begin{cases} 0 & , R_{\min} \leq R \leq R_i^{end} \\ \frac{\psi(R)}{Q_{g,i2}^{end}} & , R_i^{end} < R \leq R_{\max} \end{cases} \qquad (4.53)$$

The water saturation during this process is as follows related to the pore radius R_{i2}:

$$S_w = \frac{\int_{R_{\min}}^{R_d^{end}} \psi(R)v(R)dR + \frac{X^A(Q_{w,i2})}{Q_{w,i2}} \int_{R_d^{end}}^{R_{i2}} \psi(R)v(R)dR}{\int_{R_{\min}}^{R_{\max}} \psi(R)v(R)dR} \qquad (4.54)$$

The corresponding oil saturation is as follows: $S_o = 1\text{-}S_w\text{-}S_{gc}$.
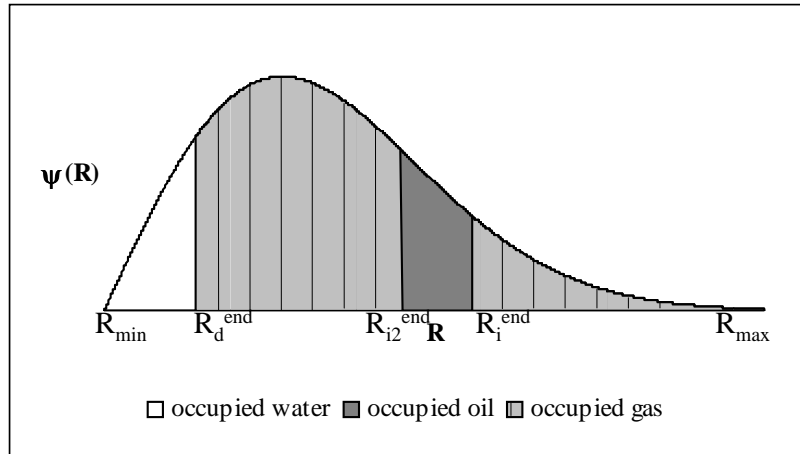
4.3.4 Secondary drainage

Since the water pressure at a chosen level underneath the oil lens is kept constant, the water will leave the model and is replaced by the gas phase, since the model has an open connection to air at the upper surface of the domain. This secondary drainage is controlled by the parameter R_{d2}. We assume that the water phase is solely displaced by gas and the oil remains at the residual oil saturation. Since the oil phase has no conductivity and is immobile, gas can not displace oil and enter at $R = R_i^{end}$. Therefore it will enter at the maximum radius that is enterable namely $R = R_{i2}^{end}$. This implies that the oil phase does not exist as an oil lens but that scattered pores are filled with oil and therefore the oil phase loses all its connectivity. The allowability equation for gas is determined by the radii that were filled with gas after secondary imbibition (between R_i^{end} and $R_{\max}$) plus the radii where gas will displace the water phase (between R_{d2} and R_{i2}^{end}) (Figure 4.8.a):

$$Q_{g,d2} = \int_{R_{d2}}^{R_{i2}^{end}} \psi(R)dR + \int_{R_i^{end}}^{R_{\max}} \psi(R)dR \qquad (4.55)$$

The occupancy equations for gas are the occupancy equations for gas after secondary imbibition (complete occupancy between R_i^{end} and $R_{\max}$) plus the part that becomes allowed (between R_{d2} and R_{i2}^{end}) times the accessibility fraction :
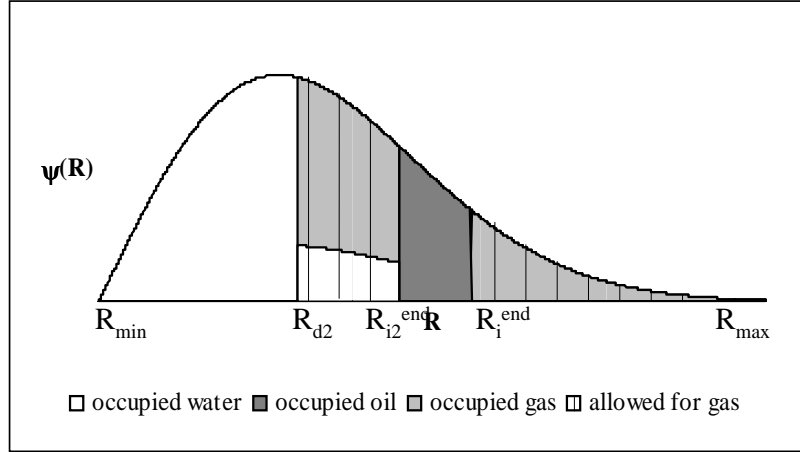
(a)

(b)

Figure 4.8: Number fraction functions of pore throat radii and the occupied and allowed fractions for gas and water described by the drainage radius R_{d2}. a. during secondary drainage. b. at the end of the secondary process.

$$X_{g,d2}^O = \int_{R_{d2}}^{R_{i2}^{end}} \psi(R)dR\left[\frac{X^A(Q_{g,d2}, X_{g,i2}^{O,end})}{Q_{g,d2}}\right] + \int_{R_i^{end}}^{R_{\max}} \psi(R)dR \quad (4.56)$$

$$\psi_{g,d2}^O(R) = \begin{cases} 0 & , R_{\min} \le R \le R_{d2} \\ \frac{\psi(R)}{X_{g,d2}^O}\left[1-\frac{X^A(Q_{g,d2},X_{g,i2}^{O,end})}{Q_{g,d2}}\right] & , R_{d2} < R \le R_{i2}^{end} \\ 0 & , R_{i2}^{end} < R \le R_i^{end} \\ \frac{\psi(R)}{X_{g,d2}^O} & , R_i^{end} < R \le R_{\max} \end{cases} \quad (4.57)$$

The allowability equations for water are the radii that were filled with water after secondary imbibition (between $R_{\min}$ and R_{i2}^{end}) minus the radii where water is displaced by gas (between R_{d2} and R_{i2}^{end}):

$$Q_{w,d2} = X_{w,d2}^O = \int_{R_{\min}}^{R_{d2}} \psi(R)dR + \int_{R_{d2}}^{R_{i2}^{end}} \psi(R)dR\left[1-\frac{X^A(Q_{g,d2})}{Q_{g,d2}}\right] \quad (4.58)$$

$$\psi_{w,d2}^O(R) = \begin{cases} \frac{\psi(R)}{Q_{w,d2}} & , R_{\min} \le R \le R_{d2} \\ \frac{\psi(R)}{Q_{w,d2}}\left[1-\frac{X^A(Q_{g,d2})}{Q_{g,d2}}\right] & , R_{d2} < R \le R_{i2}^{end} \\ 0 & , R_{i2}^{end} < R \le R_{\max} \end{cases} \quad (4.59)$$

The occupancy equations for water are the same as the allowability equations for water, since it is the displaced phase.

This secondary drainage process ends at R_d^{end}, determined by (R_d^{end} is identical to R_d^{end} calculated in Equation (4.18)):

$$Q_{w,d2}^{end} = \int_{R_{\min}}^{R_d^{end}} \psi(R)dR + \int_{R_d^{end}}^{R_{i2}^{end}} \psi(R)dR\left[1-\frac{X^A(Q_{g,d2})}{Q_{g,d2}}\right] = Q_c \quad (4.60)$$

When we assume that $Q_{g,d}^{end}$ is much larger than Q_c and therefore $X^A(Q_{g,d}^{end})$ = $Q_{g,d}^{end}$, the allowability and occupancy for the three phases are as follows (see Figure 4.8.b):

$$Q_{g,d2}^{end} = X_{g,d2}^{O,end} = \int_{R_d^{end}}^{R_{i2}^{end}} \psi(R)dR + \int_{R_i^{end}}^{R_{\max}} \psi(R)dR \quad (4.61)$$

$$\psi_{g,d2}^{O,end}(R) = \begin{cases} 0 & , R_{\min} \leq R \leq R_d^{end} \\ \frac{\psi(R)}{Q_{g,d2}^{end}} & , R_d^{end} < R \leq R_{i2}^{end} \\ 0 & , R_{i2}^{end} < R \leq R_i^{end} \\ \frac{\psi(R)}{Q_{g,d2}^{end}} & , R_i^{end} < R \leq R_{\max} \end{cases} \tag{4.62}$$

$$Q_{w,d2}^{end} = X_{w,d2}^{O,end} = \int_{R_{\min}}^{R_d^{end}} \psi(R)dR \tag{4.63}$$

$$\psi_{w,d2}^{O,end}(R) = \begin{cases} \frac{\psi(R)}{Q_{w,d2}} & , R_{\min} \leq R \leq R_d^{end} \\ 0 & , R_d^{end} < R \leq R_{\max} \end{cases} \tag{4.64}$$

$$Q_{o,d2}^{end} = X_{o,d2}^{O,end} = \int_{R_{i2}^{end}}^{R_i^{end}} \psi(R)dR \tag{4.65}$$

$$\psi_{o,d2}^{O,end} = \begin{cases} 0 & , R_{\min} \leq R \leq R_{i2}^{end} \\ \frac{\psi(R)}{Q_{o,d2}} & , R_{i2}^{end} < R \leq R_i^{end} \\ 0 & , R_i^{end} < R \leq R_{\max} \end{cases} \tag{4.66}$$

The gas saturation during this process is as follows related to the pore radius R_{d2}:

$$S_g = \frac{\frac{X^A(Q_{g,d2})}{Q_{g,d2}} \int_{R_{d2}}^{R_{i2}^{end}} \psi(R)v(R)dR + \int_{R_i^{end}}^{R_{\max}} \psi(R)v(R)dR}{\int_{R_{\min}}^{R_{\max}} \psi(R)v(R)dR} \tag{4.67}$$

The corresponding water saturation is as follows: $S_w = 1\text{-}S_g\text{-}S_{oc}$.

4.4   Model results

With the percolation model simulations we show the qualitative accuracy of the percolation theory for predicting the flow behavior of the three phases in a porous medium. We calculated the relative permeabilities of water, oil and air during the iterative processes of drainage and imbibition. We changed z (coordination number which is related to the percolation threshold Q_c, see Equation (4.1)) to investigate the influence of the threshold. For the calculations we use $R_{max} = 4$, where $\psi(R)$ is approximately zero.

In Figure 4.9 the relative permeabilities for water and gas
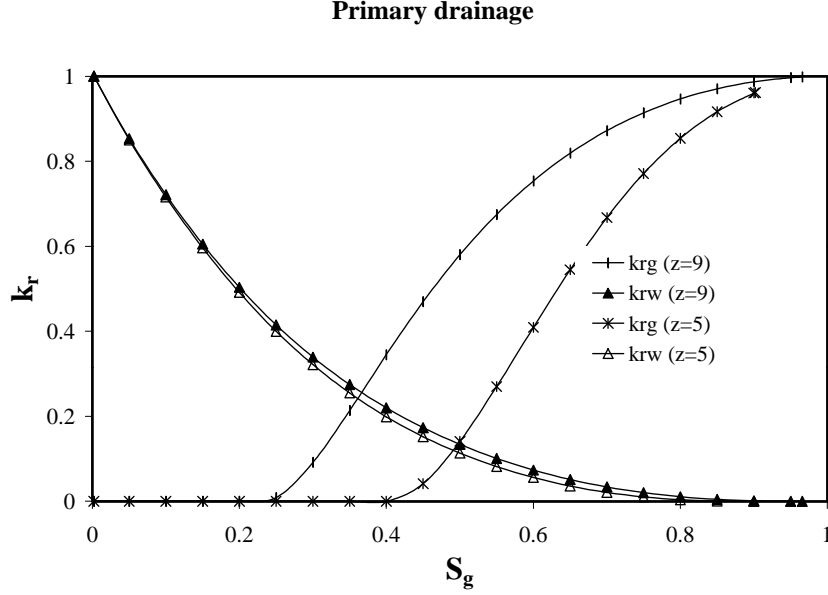
Primary drainage

Figure 4.9: Relative permeabilities for water and gas as a function of the gas saturation during primary drainage.

as a function of the gas saturation during primary drainage are shown for $z = 5$ ($Q_c = 0.25$) and $z = 9$ ($Q_c = 0.125$). We have chosen to show the relative permeability as a function of the gas saturation since the gas saturation is the advancing phase during primary drainage. This figure shows the well-known development of the relative permeabilities during primary drainage until the connate water saturation is reached. The effect of the percolation threshold is visible in the relative gas permeability curve, which becomes only larger than zero after exceeding the percolation threshold. We see that a smaller value for z (larger threshold value) reduces the relative permeability of the advancing phase (gas) significantly.

Simulation	S'_w	S'_g	S_{wc}	k'_{rw}	k'_{rg}
z=5	0.098	0.902	0.098	0	0.962
z=9	0.034	0.966	0.034	0	0.998

Table 4.2: The connate saturations, end point relative permeabilities and end-point saturations during primary drainage for z=5 and z=9.

Primary imbibition
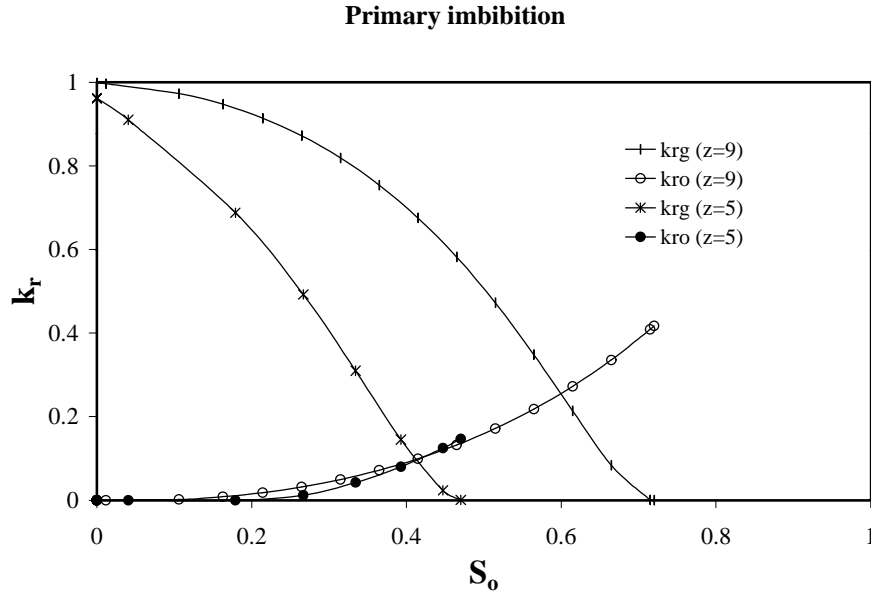
Figure 4.10: Relative permeabilities for gas and oil as a function of the oil saturation during primary imbibition.

The reason for that is that a larger threshold value results in a larger connate saturation and therefore the relative permeability will be smaller. The accompanying values for the endpoint relative permeability for water and gas (k') the endpoint saturations for water and gas (S') and the connate water saturation are shown in Table 4.2.

Figure 4.10 shows the relative permeabilities for gas and oil as a function of the oil saturation (the advancing phase) during primary imbibition, where water remains at the connate water saturation and oil displaces the gas phase until the connate gas saturation is reached. The continuation of the relative permeability for one phase from one process to the other (in

Simulation	S'_w	S'_g	S'_o	S_{wc}	S_{gc}	k'_{ro}	k'_{rg}
z=5	0.098	0.428	0.470	0.098	0.428	0.147	0
z=9	0.034	0.245	0.721	0.034	0.245	0.417	0

Table 4.3: The connate saturations, end point relative permeabilities and end point saturations during primary imbibition for z=5 and z=9.

Secondary imbibition
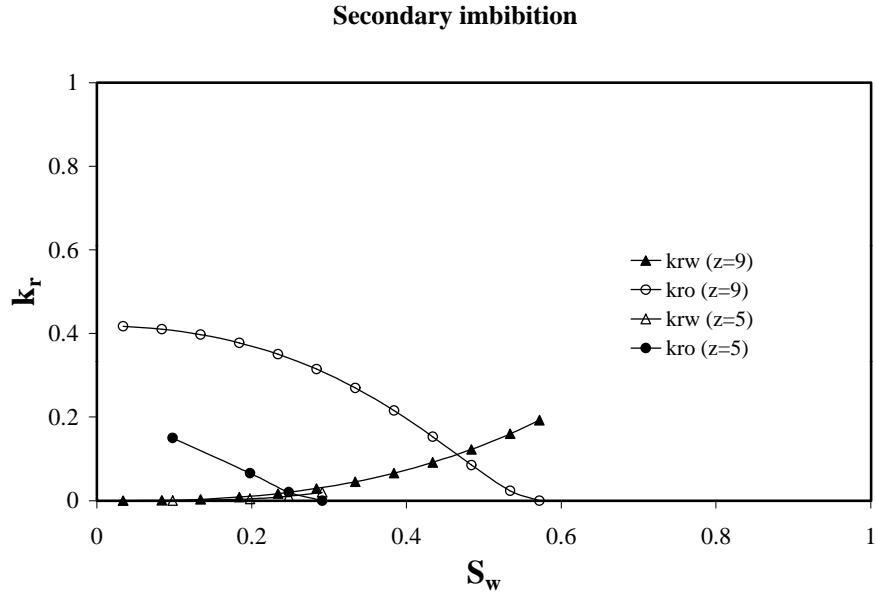
Figure 4.11: Relative permeabilities for water and oil as a function of the water saturation during secondary imbibition.

Simulation	S'_w	S'_g	S'_o	S_{wc}	S_{gc}	S_{or}	k'_{rw}	k'_{ro}
z=5	0.291	0.428	0.281	0.098	0.428	0.281	0.020	0
z=9	0.572	0.245	0.183	0.034	0.245	0.183	0.193	0

Table 4.4: The connate saturations, end point relative permeabilities and end point saturations during secondary imbibition for z=5 and z=9.

this case from primary drainage to primary imbibition) is preserved. This can be seen in Figure 4.10 where the starting points of the relative permeability for gas ($k_{rg} = 0.962$ ($z = 5$) and $k_{rg} = 0.998$ ($z = 9$) at $S_o = 0$) are identical to the end point relative permeabilities for gas in Figure 4.9 (at $S_g = 0.902$ and $S_g = 0.966$) (see also Table 4.2). Also the continuation of the saturation from one process to another is preserved. The end point gas saturation after primary drainage is 0.902 ($z = 5$). At the beginning of primary imbibition $S_o = 0$ and $S_g = 1-S_o-S_{wc} = 1-0-0.098 = 0.902$, which shows continuation. The same applies for S_o ($z = 9$). Furthermore it can be seen in Figure 4.10 that oil can continue to displace gas until the connate gas saturation and connate water saturation are reached. The final values for the oil saturation (S_o) are: for $z = 5$, $S_o = 1-0.098-0.428 = 0.470$, for $z = 9$, $S_o = 1-0.034-0.245 = 0.721$ (see Table 4.3). The end point relative permeabilities for oil and gas, the end point saturations for oil and gas and the connate water and gas saturations after primary imbibition are shown in Table 4.3. Next a cross over of relative permeabilities can be noticed for the two z values at $S_o \approx 0.4$. The reason for this cross over is the connate gas saturation which is larger for $z = 5$ ($S_{gc} = 0.428$) than for $z = 9$ ($S_{gc} = 0.245$) and therefore the relative gas permeability will decrease faster for a smaller z value. Consequently the relative oil permeability will increase faster for a smaller z value.

Figure 4.11 shows the relative permeabilities for water and oil as a function of the water saturation (the advancing phase) during secondary imbibition, where gas remains at the connate gas saturation and water displaces oil until the connate oil saturation is reached. Again we see that the continuation of the relative oil permeability is preserved: at the beginning of secondary imbibition the relative oil permeability ($k_{ro} = 0.265$ ($z = 5$) and $k_{ro} = 0.475$ ($z = 9$)) is identical to the endpoint relative oil permeability after primary imbibition. The end point relative permeabilities for oil and water, the end point saturations for oil and water and the residual oil and connate gas saturations after secondary imbibition are shown in Table 4.4. The connate water saturation is very small, while the residual oil saturation is very high. This is to be attributed to the fact that we disregard the existence of the volume of the pore bodies. At $S_w = 0.098$, the oil phase infiltrates which results in $S_o = 1-S_w-S_{gc} = 1-0.098-0.428 = 0.474$ (for $z = 5$). This is identical to the end point oil saturation after primary imbibition, which implies continuation of the oil saturation.

Figure 4.12 shows the relative permeabilities for water and gas as a func-

Secondary drainage
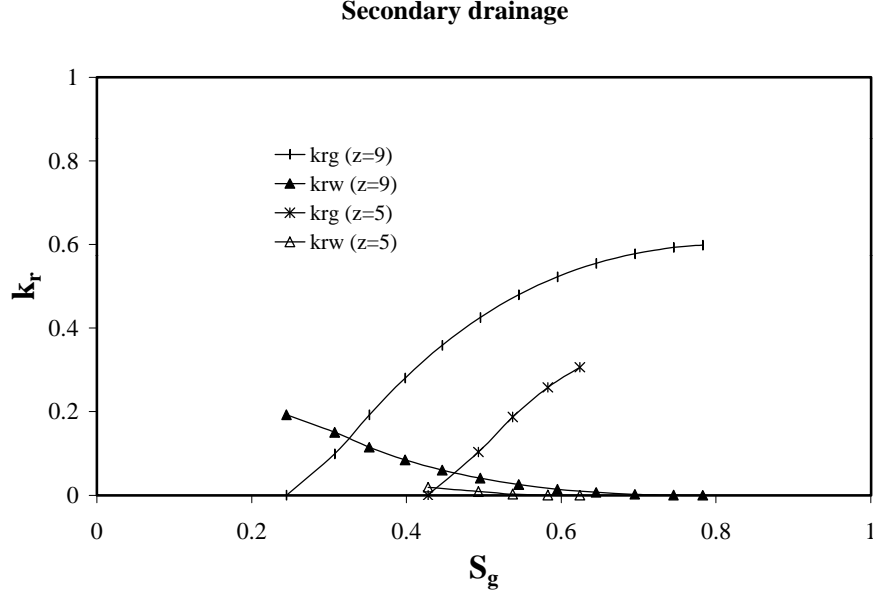
Figure 4.12: Relative permeabilities for gas and water as a function of the gas saturation during secopndary drainage.

tion of the gas saturation (the advancing phase) during secondary drainage, where oil remains at the connate oil saturation and gas displaces the water phase until the connate water saturation is reached. The continuation of the relative permeabilities is again preserved. Also the continuation of the water saturation is preserved. The relative water permeability starts at $S_g = 0.438$ (for $z = 5$), which implies that $S_w = 1\text{-}S_g\text{-}S_{or} = 1\text{-}0.438\text{-}0.281 = 0.281$, which is the endpoint water saturation at the end of secondary imbibition. The accompanying endpoint relative permeabilities and end point saturations are shown in Table 4.5.

An effect of an increasing coordination number z is the decrease of

Simulation	S_w'	S_g'	S_o'	S_{wc}	S_{gc}	S_{or}	k_{rw}'	k_{rg}'
z=5	0.098	0.621	0.281	0.098	0.428	0.281	0	0.306
z=9	0.034	0.783	0.183	0.034	0.245	0.183	0	0.599

Table 4.5: The connate saturations, end point relative permeabilities and end point saturations during secondary drainage for z=5 and z=9.

the predicted hydraulically irreducible saturations of all the phases. This explains the relative sensitivity to the coordination number.

4.5 Conclusion

We have found the relative permeabilities for a specific sequence of events for an oil spill, based on percolation theory. We extended the two-phase (water and oil) code that Heiba [13] developed to a three phase system (water, oil and gas). This system is based on the subsurface where an oil lens floats above the groundwater level. We started with a two phase system including water and gas and introduce the oil phase as the third phase (the infiltration of the oil lens). Furthermore we simulate water infiltration (water displaces oil) and subsequently drainage (gas displaces water) since we assume a constant water pressure below the oil lens. All these drainage and imbibition processes last until a connate saturation is reached where a phase becomes immobile. This implies that there is always one phase immobile and therefore only two phases are able to flow.

The relative permeabilities calculated using the percolation theory are in close qualitative agreement with data typical of three-phase systems where the same wettability order is assumed [5]. This means that this theory does adequately describe the qualitative behavior of iterations of drainage and imbibition processes for three phases including hysteresis. The relatively high residual oil saturation or small connate water saturation due to the cylindrical tubes, however, are a shortcoming of this theory. The main virtue of percolation theory in its present form is that it gives a good qualitative understanding of a three-phase system.

Notation

C	generating function employed by Stinchcombe
G_j	conductivity function
g	conductivity $[m/s]$
k_{ri}	relative permeability of phase i
k'_{ri}	end point relative permeability of phase i
n	exponent in the volume definition
P_c	capillary pressure $[Pa]$
Q_j	allowed fraction for phase j
Q_c	critical fraction= percolation threshold

R	radius of a bond $[m]$
S	saturation
t	Laplace transform in equation of Stinchcombe
v	volume of a bond $[m^2]$
X	fraction of the bonds that is accessible/occupied
x	variable of equation of Stinchcombe
z	average number of bonds that originate from one node
δ	Dirac delta function
θ	effective conductivity
σ	interfacial tension $[N/m^2]$
$\psi(R)$	number fraction function

Subscripts

d	drainage
$d2$	secondary drainage
g	gas
gc	connate gas
i	imbibition
$i2$	secondary imbibition
max	maximum
min	minimum
o	oil
or	residual oil
w	water
wc	connate water

Superscripts

a	allowed
A	accessible
end	end situation of a process
ini	initial
O	occupied

Chapter 5

Numerical and analytical analysis of water infiltration into an LNAPL spill*

5.1   Introduction

Contamination in the subsurface by Light Non Aqueous Phase Liquids (LNAPL) forms a serious threat to our drinking water supplies. Modern technologies supply numerous techniques to clean up the LNAPL. It is very important to obtain as much knowledge about the behavior of LNAPL to choose a technique that will effectively remove the contamination. In this case, we want to obtain more knowledge about the amount of entrapped LNAPL into the water phase and more specific about the influence of water infiltration on the entrapment. Henceforth, we use the term oil as a comprehensive term for LNAPL.

Petroleum engineers already use water infiltration and gas infiltration as a technique to reduce capillary entrapment of oil in small scale reservoir heterogeneities. This is called WAG (water-alternate-gas injection) or SWAG (simultaneous-water-and-gas injection). Examples of this method are described by Larsen et al. [21] and van Lingen [50]. Entrapped oil contamination in the subsurface is a similar problem to oil in small scale reservoir heterogeneities and therefore it could be a useful tool for environmental sciences. The basic principle and the optimization of WAG and SWAG is based on experimental and empirical results and no theoretical background is available yet.

Heiba [13] and Chapter 4 of this thesis have shown how percolation theory can be used for a three phase system, where drainage and imbibition processes take place. These processes continued until a connate saturation

---

*by A. Marsman and G.A. Bartelds
submitted to Transport in Porous Media

was reached for one of the three phases, i.e. water, gas or oil is immobile. This means that during these processes two phases are flowing. Furthermore they assume that water and gas are always shielded from each other by the oil phase, since the order of wettability is: water is the most wetting phase, oil is the intermediate wetting phase and gas is the non-wetting phase.

In this study, we expand this three phase model to an application where we will compare two situations where water infiltrates into an oil lens that floats above the groundwater level. In the first situation water is injected at the upper surface of the domain and infiltrates downwards into the oil lens. In the second situation the water pressure at a certain level beneath the oil lens is increased so that water infiltrates upwards. After the water infiltration, the water pressure beneath the oil lens returns to its initial value for both situations so that drainage occurs. The accompanying drainage and imbition processes do not necessarily continue until a connate saturation is reached and therefore more complicated situations can arise where three phases can flow. These two situations are calculated numerically and percolation theory is used to obtain more insight into the phenomena that take place.

5.2   Problem description

The first case that will be investigated is Case A where water infiltrates downwards into the oil lens. This is shown in Figure 5.1. The history of the oil lens before the water infiltration is as follows: 1. Initially the domain is water saturated. 2. Drainage takes place where gas displaces water and the unsaturated zone in the subsurface is developed. 3. Oil floats downwards into the domain, which in this case is called imbibition since oil displaces gas. 4. Water infiltrates into the oil lens. 5. Water flows through the oil lens and leaves at the bottom of the domain: gas displaces water. These 5 processes must be simulated to accomplish the correct hysteresis.

In Case B (see Figure 5.1) water infiltrates upwards. In this case the hysteresis is as follows: 1. The domain is water saturated. 2. Drainage takes place where gas displaces the water phase (in Case B only a small amount of gas displaces the water phase so that this is still called the saturated zone). 3. Oil floats downwards into the domain and displaces the water phase: drainage occurs. 4. Water infiltrates upwards into the oil lens: fluctuating groundwater level (water displaces oil). 5. Water leaves
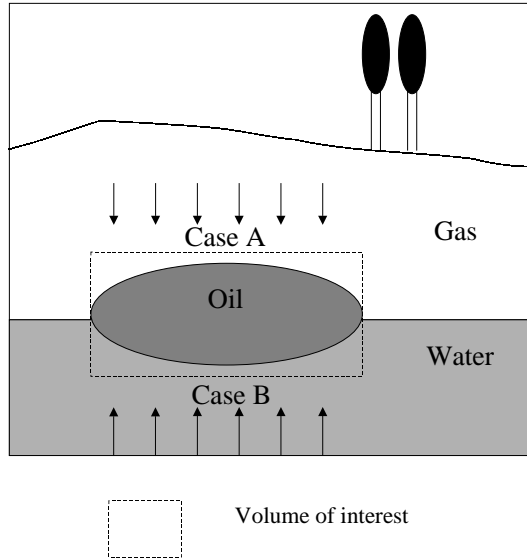
Figure 5.1: The three phase system that is considered. The dashed square shows the volume of interest for this work. The arrows represent the downwards water infiltration (Case A) and the upwards water infiltration (Case B). The subdomains represent the areas where one phase dominates whereas all three phases are present in each subdomain.

the domain (the groundwater level lowers and oil displaces water).

5.3 Numerical model

5.3.1 Case A: downwards water infiltration

The multiphase flow code STOMP, developed by White et al. [51] was used to model this two-dimensional numerical experiment. This numerical model we use is based on the mixed form of the Richard's Equation. The governing flow and transport equations are solved numerically by following an integrated finite difference method. Spatial discretization of the computational domain with the integrated finite difference method is limited to orthogonal systems. The algebraic forms of the nonlinear governing equations are solved with a multi-variable residual-based Newton-Rapson iteration technique. The parameter values that are used in this experiment are given in Table 5.1. The height (70 cm) is discretized by 36 nodes

Property	Value
Irreducible water saturation S_{wc}	0.20
Air-water scaling factor β_{aw}	1.00
Air-NAPL scaling factor β_{ao}	2.25
NAPL-water scaling factor β_{ow}	1.80
Intrinsic permeability K	$2.14{\times}10^{-11}[m^2]$
Porosity ϕ	0.40
NAPL density ρ_o	830 $[kg/m^3]$
NAPL viscosity μ_o	$2.046{\times}10^{-3}[Pas]$
Length of column	70 $[cm]$
Width of column	200 $[cm]$
Van Genuchten parameter α	1 $[m^{-1}]$
Van Genuchten parameter n	3.16
Initial oil volume V_1	$6.9{\times}10^{-4}[m]$
Maximum residual oil saturation $S_{or}^{\max}$	0.395

Table 5.1: Parameters and characteristic lengths and times used in the computations.

and the width (200 cm) is discretized by 40 nodes. For symmetry reasons we only model half the domain and therefore the left boundary conditions present the vertical symmetry axis. The initial timestep was 10 s and the maximum allowable timestep was 10 Min.

The initial conditions for this experiment are as follows: the 2-D domain is homogeneously filled with sand. At the lower boundary of the domain a water pressure is applied that results in a completely water saturated domain. The initial oil pressure at the bottom of the domain is equal to the water pressure so that an imaginary amount of oil is situated above the domain. The boundary conditions are: 1. Zero flux Neumann conditions at the left boundary of the domain in view of the vertical symmetry axis. 2. Lowering of the groundwater level was simulated by a step-wise linearly declining Dirichlet boundary condition for water pressure at the bottom of the domain to accomplish a groundwater level of 10 cm. 3. A flux on top of the symmetry axis and the 3 nearest nodal points in the horizontal direction are the Neumann boundary condition that describes the oil infiltration of 0.7 l from $t = 12.2$ h until $t = 12.3$ h. Due to gravity and capillary forces the oil spreads along the groundwater level. Here we distinguish between two different situations: one where the groundwater level remains stable at 10 cm from the bottom of the domain. This situation is referred to as the

reference case to compare with the effects of the more complex infiltration model. The infiltration of the rainwater is simulated by imposing a water flux at the upper surface of the domain. The flux is imposed for 109 minutes (from $t = 17.4$ h until $t = 19.2$ h) and the magnitude is 1.6055×10^{-7} m^3/s. That means that approximately $1.05 \times 10^{-3} m^3$ water is added to this domain. The water pressure at the bottom of the domain remains constant so that the water level eventually will not increase.

5.3.2　Case B: upwards water infiltration

The same numerical model is used for this simulation as in section 5.3.1. Also the used parameter values (Table 5.1) and the boundary conditions are the same as in section 5.3.1. Solely the imposed water flux at the upper surface is not incorporated in this simulation and instead a changing water pressure at the bottom of the domain is imposed to simulate upwards water infiltration. The water pressure at the bottom is initially 686 Pa at $t = 17.4$ h (groundwater level is approximately 7 cm) and it is increased until 4114 Pa at $t = 19.2$ h (42 cm). This means that similar to Case A approximately $1.05 \times 10^{-3} m^3$ water is added to the domain. Subsequently the water pressure at the bottom will be diminished until the original values are reached so that water will move downwards. More details of this fluctuating water level simulation can be found in Chapter 2.

5.4　Numerical results

To enable a comparison, we use a reference case where no water infiltration takes place and the parameter values used are the same as in Table 5.1. The oil can spread above the capillary fringe without being disturbed by infiltration processes. The results of this experiment are shown in Figure 5.2, where the vertically integrated free oil saturations ($W_f = \phi \int S_{of}$ $(T)dz$, where S_{of} is the free oil saturation) are plotted as a function of the horizontal dimension x at two moments in time. The development of W_f in the reference case is as follows: the integrated free oil in the middle of the lens decreases and the horizontal dimension of the lens increases. This is a consequence of the spreading above the capillary fringe.

　　Figure 5.3 shows W_f at the same moments in time for Case A where downwards water infiltration takes place. At $t = 17.4$ h, before the infiltration starts, there is no difference between Case A and the reference case. Since the water pressure at the bottom is constant, the water floats down-

reference
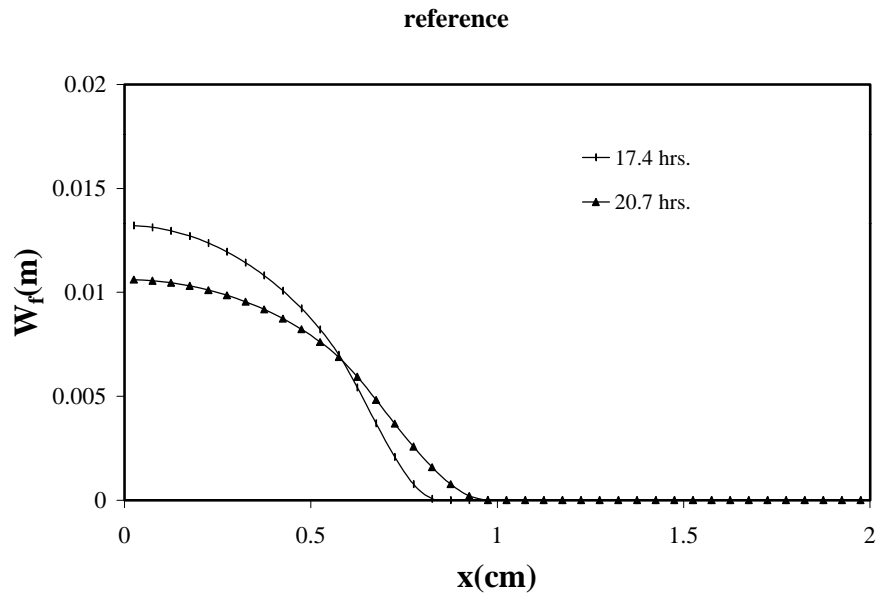
Figure 5.2: Reference situation where no water infiltration takes place: the integrated free oil volume as function of the horizontal coordinate at two moments in time.

downwards water infiltration
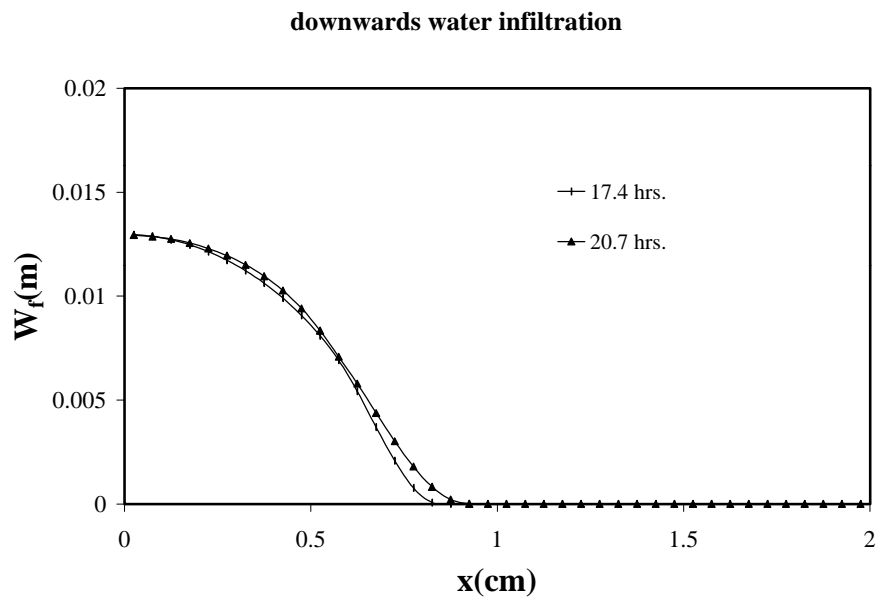
Figure 5.3: Case A where water infiltrates downwards into the oil lens. The integrated free oil volume is plotted as a function of the horizontal coordinate before (t=17.4 h) and after (t=20.7 h) the infiltration.

upwards water infiltration
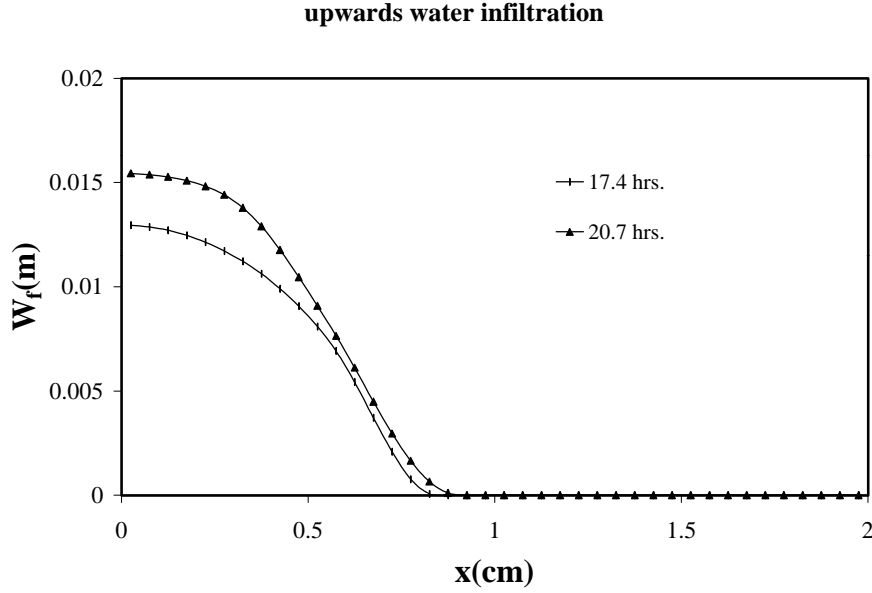
Figure 5.4: Case B where water infiltrates upwards into the oil lens. The integrated free oil volume is plotted as a function of the horizontal coordinate before (t=17.4 h) and after (t=20.7 h) the infiltration.

wards through the bottom surface of the model and at $t = 20.7$ h the oil has become more mobile than before the water infiltration, which is shown in Figure 5.3.

The same is done for Case B and the results are shown in Figure 5.4. The most important feature of this Figure is the free oil at $t = 20.7$ h after the water level has returned to its original position. We see that the mobility of the oil lens has increased after the upwards water infiltration like in Case A. To obtain more insight into this infiltration phenomenon and to understand the differences between the two cases, we use percolation theory to investigate the water infiltration qualitatively and on the pore scale.

5.5   Percolation theory

Percolation theory is a statistical method that describes, on the pore scale, the probability that a pore space is accessible for a wetting or non-wetting fluid. It can be used to improve our understanding of relative permeabilities

and capillary pressure curves in porous media. The theory pertains to network models that consist of bonds and nodes. We will briefly define some definitions of percolation theory in this section. The *coordination number* Z is defined as the average number of bonds that join at each node. Bonds with a radius bigger than a certain radius are due to capillary effects *allowed* for a phase (Q_j). The *accessible* fraction ($X^A(Q_j)$) is the fraction of bonds connected to some continuous path across the network, i.e. accessible means that both the bonds are allowed by the phase, and the surrounding bonds do not inhibit the fluid to invade. *Occupied* ($X^O(Q_j)$) means that the bonds are actually occupied by that phase. The *percolation threshold* (Q_c) is the largest fraction of allowed bonds below which the accessible fraction and thus the equivalent conductivity, is zero. Furthermore we have chosen to use the Bethe tree to represent the pore space and the Rayleigh distribution to represent the pore size distribution as a function of the radius $\psi(R)$. For more details and background information we refer to Heiba [13], Stauffer [41], Sahimi [39][38] and also Chapter 4 of this thesis.

In the next paragraphs the processes of primary drainage, primary imbibition, secondary imbibition and secondary drainage will be described with the aid of percolation theory. During primary drainage, gas displaces the water phase until it reaches a water saturation comparable to the numerical values. Primary imbibition means that oil displaces the gas phase until a fixed oil saturation is reached. Water infiltration into the oil lens is simulated by secondary imbibition, where water displaces the oil phase. This process is followed up by secondary drainage, where gas again displaces the water phase.

5.5.1 Primary drainage

Initially the situation is completely water saturated (water is the wetting fluid) prior to migration of gas (air, the non-wetting 'fluid') into the domain. This is shown in Figure 5.5. $R_{\max}$ is the maximum radius in the network model and $R_{\min}$ is the minimum radius in the network model. All the bonds are allowed to and occupied by water. Figures 5.6.a and 5.6.b show the number fraction function during the primary drainage process and at the end of the primary drainage process, where all the bonds larger than R_d are allowable for gas. We refer to Chapter 4 for a more detailed description of this process. The process continues until R_d reaches R_d^{end}, which is the connate water radius.
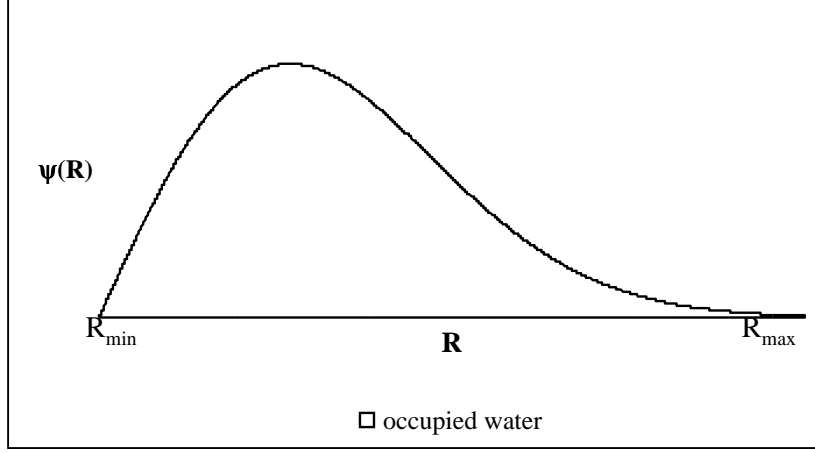
Figure 5.5: The number fraction $\psi(R)$ as a function of the radius R where all the radii are filled with water.

5.5.2   Primary imbibition

During the second process, the oil phase enters the network model. Since oil is the non-wetting phase compared with the water phase and the wetting phase compared with the gas phase, it will enter in the radii that separate the water and gas phase (see Figure 5.7.a). This process is called imbibition since oil (the wetting phase) displaces gas (the non-wetting phase). For a more detailed explanation of this displacement, we refer to Chapter 4. The initial conditions for water remain the same as the water conditions at the end of the primary drainage process since water has reached the connate water saturation. The accompanying imbibition radius is called R_i. All the bonds that are larger than R_d^{end} and smaller than R_i will be allowed for oil. The resulting allowability equations ($Q_{o,i}$, $\psi_{o,i}^a(R)$, $Q_{g,i}$ and $\psi_{g,i}^a(R)$) and occupancy equations ($X_{o,i}$, $\psi_{o,i}^O(R)$, $X_{g,i}$ and $\psi_{g,i}^O(R)$) for oil and gas during imbibition are described in the Appendix.

We see at the end of this process (Figure 5.7.b) that only the water phase has lost its conductivity and is still an immobile phase. The main difference between this case and the general case as described in Chapter 4 is that the oil imbibition does not continue until the gas becomes immobile ($R = R_i^{end}$), which results in an end situation where both oil and gas can exist between R_d^{end} and R_i^*(the radius where the process stops, is denoted by $*$).
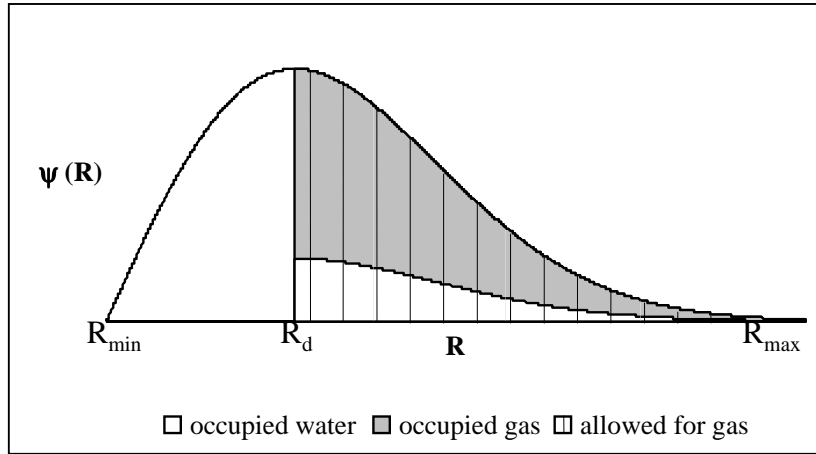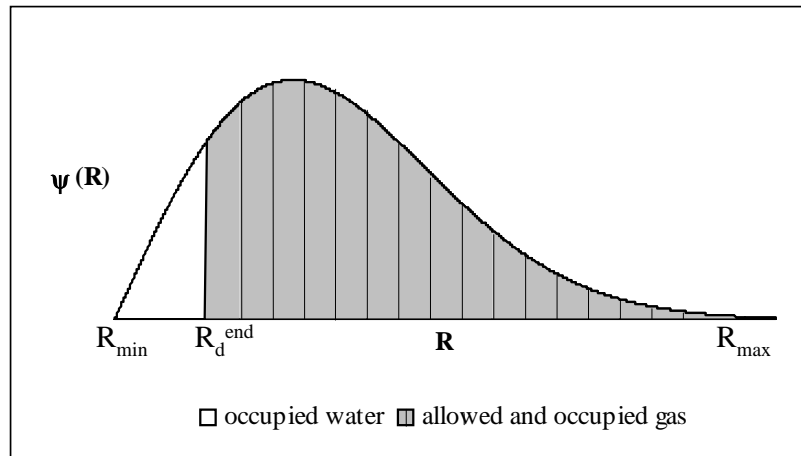
Figure 5.6: Number fraction functions of pore throat radii and the occupied and allowed fractions for gas and water described by the drainage radius R_d, R_d^{end} is the limiting pore radius. a. during primary drainage. b. at the end of the drainage process.
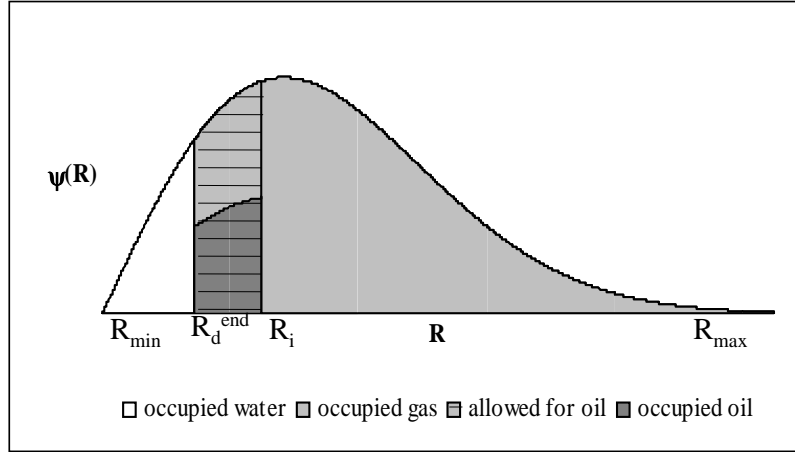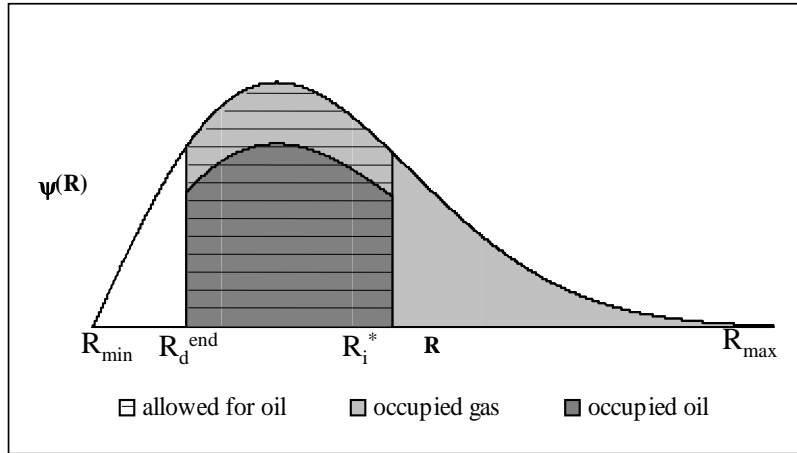
(a)

(b)

Figure 5.7: Number fraction functions of pore throat radii and the occupied and allowed fractions for gas and oil described by the imbibition radius R_i. This process continues until R_i^*. R_i^{end} is the limiting connate gas pore radius for imbibition. a. during primary imbibition. b. at the end of the primary imbibition process.
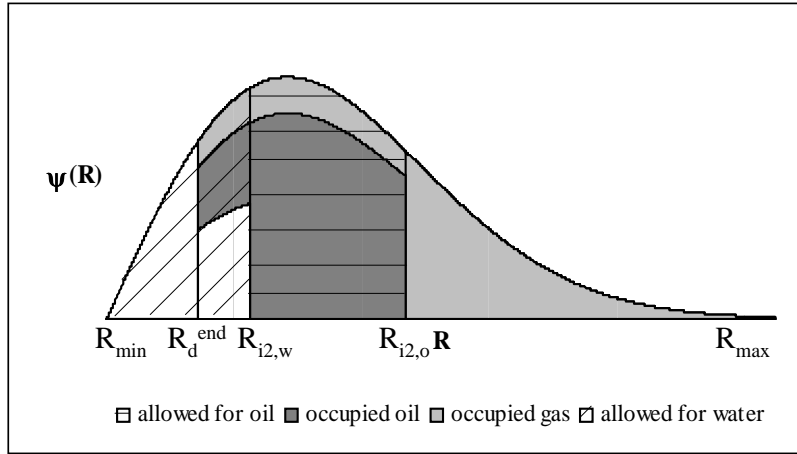
5.5.3 Secondary imbibition

During secondary imbibition, water displaces oil and oil displaces gas (Figure 5.8.a). Since we assume that solely the connate water saturation was reached at the end of the primary imbibition process, the secondary imbibition consists of both water displacing oil as well as oil displacing gas. Four regions in the radii distribution will exist: the region where water is the only phase present (connate water), a region where water, oil and gas can exist as a consequence of water imbibition, a region where both oil and gas exist and a region where gas occupies all the pores. Since two imbibition processes take place: water displaces oil and oil displaces gas, two radii must be defined: a radius that controls the imbibition process of water displacing oil is called $R_{i2,w}$ and the radius of oil displacing gas is called $R_{i2,o}$. This process continues until a chosen water saturation is reached. The accompanying radii are called $R_{i2,w}^*$ and $R_{i2,o}^*$ (see Figure 5.8.b). The allowability and occupancy equations for water, oil and gas are described in the Appendix.

Water is allowed to all the pore-segments it occupied at connate water saturation, i.e. all radii between $R_{\min}$ and R_d^{end}, plus any pore-segment that it could enter between R_d^{end} and $R_{i2,w}^*$. The accompanying occupancy equations for water are however different from the equations where gas is at its connate saturation, since water will displace both the oil and the gas phase.

5.5.4 Secondary drainage

Since the water pressure at a chosen level underneath the oil lens is kept constant, the water will leave the model and is replaced by the gas phase. This is possible since the model has an open connection to air at the upper surface of the domain. This secondary drainage is controlled by the parameters $R_{d2,o}$ and $R_{d2,g}$. We assume that the water phase is displaced by the oil phase and the oil phase is replaced by the gas phase. Six regions in the radii distribution can exist (see Figure 5.9) : the region where connate water is the only phase present ($R_{\min}$-R_d^{end}), a region where water, oil and gas can exist as a consequence of the previous water imbibition (R_d^{end}-$R_{d2,o}$), a region where water, oil and gas exist ($R_{d2,o}$-$R_{i2,w}^*$), a region where oil and gas exist ($R_{i2,w}^*$-$R_{d2,g}$), a region where gas displaces oil ($R_{d2,g}$-$R_{i2,o}$) and a region where gas occupies all the pores ($R_{i2,o}$-$R_{\max}$). The allowability equations for gas are the radii that were filled with gas after secondary
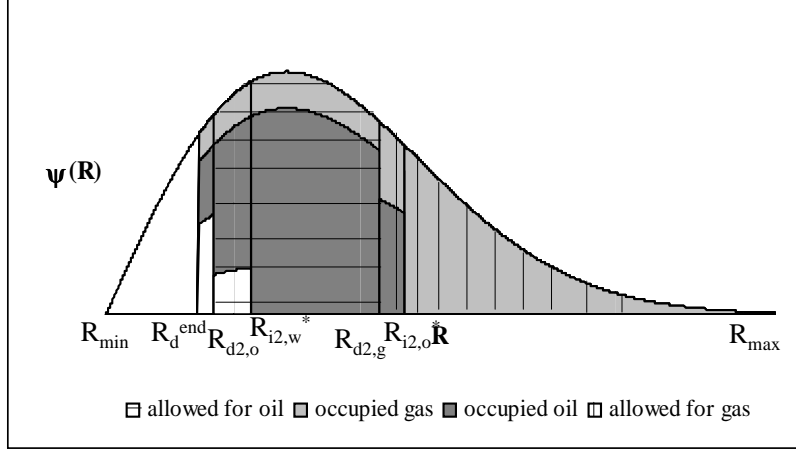
(a)
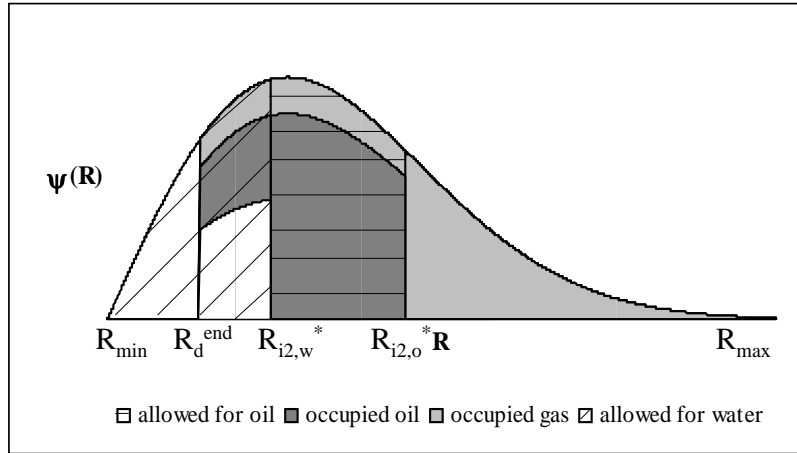
(b)

Figure 5.8: Number fraction functions of pore throat radii and the occupied and allowed fractions during secondary imbibition described by $R_{i2,w}$ (water displaces oil) and $R_{i2,o}$ (oil displaces gas). This process continues until $R^*_{i2,w}$ and $R^*_{i2,o}$. a. during secondary imbibition. b. at the end of the secondary imbibition process.

Figure 5.9: Number fraction functions of pore throat radii and the allowed fractions during secondary drainage described by $R_{d2,o}$ (oil displaces water) and $R_{d2,g}$ (gas displaces oil).

imbibition (between R_d^{end} and R_{max}) plus the radii where gas will displace the oil phase (between $R_{d2,g}$ and $R_{i2,o}^{end}$). All the allowability and occupancy equations are described in the Appendix. The main feature is that, after the secondary drainage, the radii between R_d^{end} and $R_{i2,o}^*$ contain oil, which means that in total, more bonds are filled with oil which leads to an increase of mobility. Figure 5.7.b can be used as a reference case where no water infiltration has taken place. Comparing Figure 5.9 and Figure 5.7.b shows that the oil occupies more bonds after the water infiltration.

5.6 Analytical results

The percolation model simulations show the qualitative behavior of the oil lens during water infiltration. We calculated the relative permeabilities of water, oil and air during the iterative processes of drainage and imbibition. We have chosen to use the coordination number $Z = 9$ since these results agree best with the numerical results.

Figure 5.10 shows the relative permeabilities for water and gas as a function of the gas saturation (the advancing phase) during primary drainage. This process continues until the connate water saturation is reached. The accompanying values for the endpoint relative permeability for water and gas (k'), the endpoint saturations for water and gas (S') and the connate
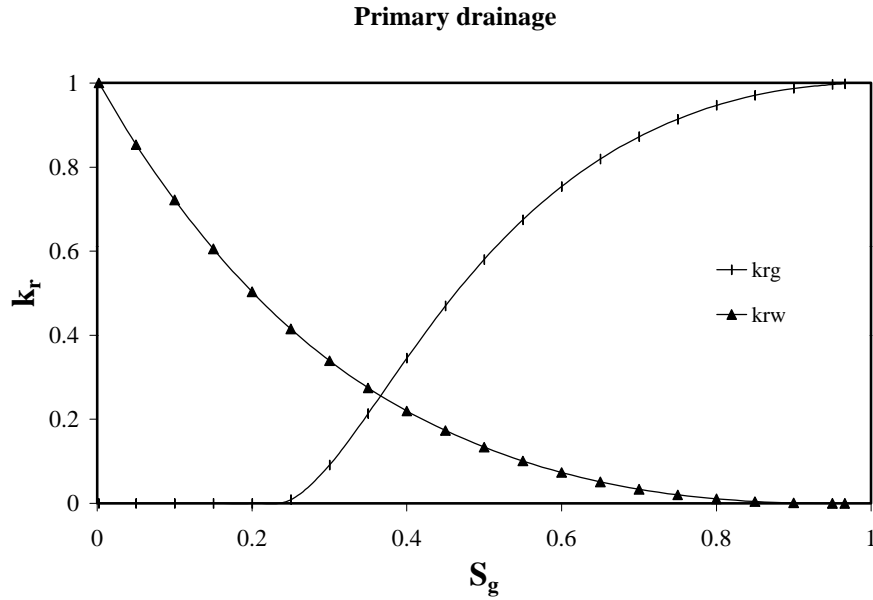
Primary drainage

Figure 5.10: Relative permeabilities for water and gas as a function of the gas saturation during primary drainage.

water saturation are shown in Table 5.2. These results are similar to the primary drainage results in Chapter 4 where the process similarly continues until the connate water saturation is reached.

Figure 5.11 shows the relative permeabilities for gas and oil as a function of the oil saturation (the advancing phase) during primary imbibition, where water remains at the connate water saturation (and consequently the relative water permeability remains zero) and oil displaces gas until the oil saturation has reached a chosen value: $S_o = 0.3$. This is the point where we deviate from Chapter 4, since the imbibition does not continue until the connate gas saturation is reached. The continuation of the relative permeability for one phase from one process to the other (in this case from

S'_w	S'_g	S_{wc}	k'_{rw}	k'_{rg}
0.034	0.966	0.034	0	0.998

Table 5.2: The connate saturations, end point relative permeabilities and end-point saturations during primary drainage.
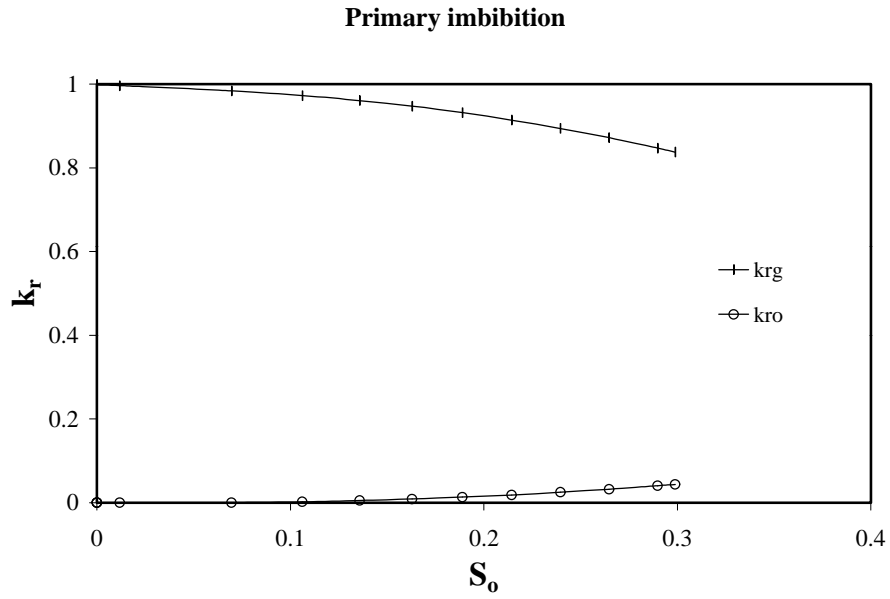
Figure 5.11: Relative permeabilities for gas and oil as a function of the oil saturation during primary imbibition.

S'_w	S'_q	S'_o	S_{wc}	S_{gc}	k'_{ro}	k'_{rg}
0.034	0.666	0.3	0.034	0.245	0.044	0.837

Table 5.3: The connate saturations, end point relative permeabilities and end point saturations during primary imbibition.

Secondary imbibition
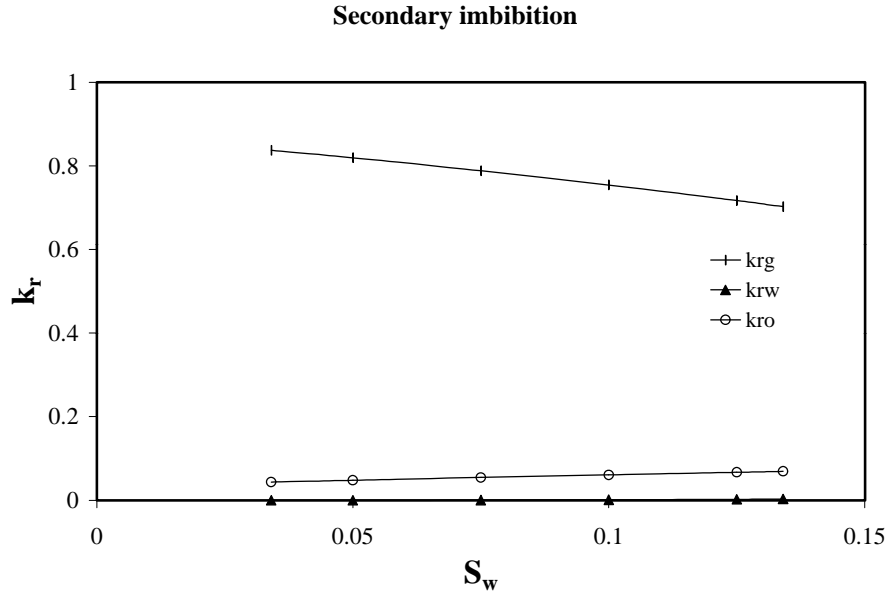
Figure 5.12: Relative permeabilities for water and oil as a function of the water saturation during secondary imbibition.

primary drainage to primary imbibition) is preserved. This follows from the endpoint relative permeabilities after primary drainage ($k'_{rg} = 0.998$) and the starting points in Figure 5.11 ($k_{rg} = 0.998$). The same accounts for the continuation of saturations: the end point saturations after primary drainage ($S'_w = 0.034$ and $S'_g = 0.966$) which are identical to the starting points in Figure 5.11 ($S_g = 1$-S_o-$S_{wc} = 1$-0-$0.034 = 0.966$). Since the imbibition of oil does not continue until the connate gas saturation is reached, the endpoint relative permeability for gas is not zero. The end point relative permeabilities for oil and gas, the end point saturations for water, oil and gas and the connate saturations for water and gas are shown in Table 5.3.

S'_w	S'_g	S'_o	S_{wc}	S_{gc}	S_{or}	k'_{rw}	k'_{ro}	k'_{rg}
0.134	0.566	0.3	0.034	0.245	0.183	0.003	0.069	0.703

Table 5.4: The connate saturations, end point relative permeabilities and end point saturations during secondary imbibition.
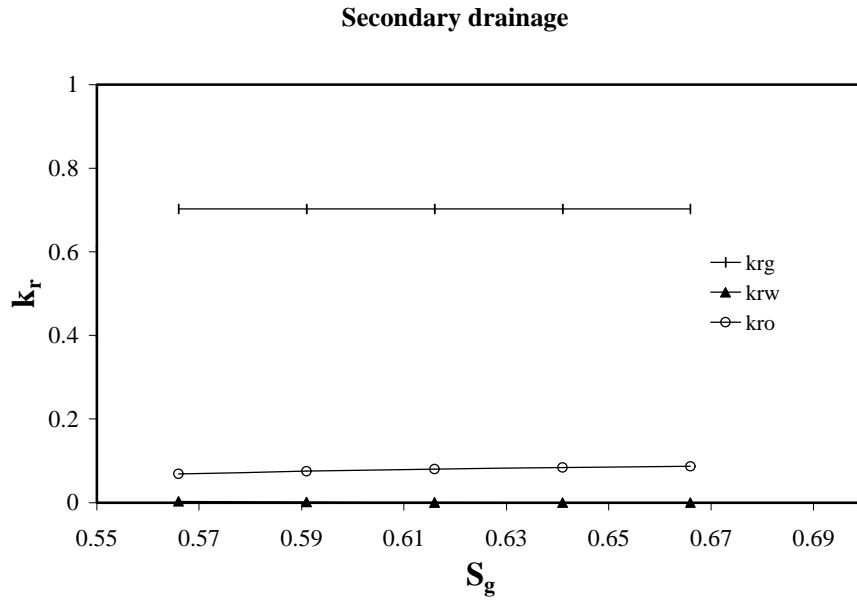
Secondary drainage

Figure 5.13: Relative permeabilities for gas and water as a function of the gas saturation during secondary drainage.

S'_w	S'_q	S'_o	S_{wc}	S_{gc}	S_{or}	k'_{rw}	k'_{ro}	k'_{rq}
0.034	0.666	0.3	0.034	0.245	0.183	0	0.087	0.703

Table 5.5: The connate saturations, end point relative permeabilities and end point saturations during secondary drainage.

Figure 5.12 shows the relative permeabilities for water, oil and gas as a function of the water saturation (the advancing phase) during secondary imbibition, where water displaces oil and oil displaces gas. Table 5.4 shows the accompanying endpoint relative permeabilities, end point saturations and connate saturations. The continuation of the relative permeabilities and saturations is preserved. The oil saturation remains constant at $S_o = 0.3$, the water saturation increases from $S_w = 0.034$ to $S_w = 0.134$, which results in a decrease of the gas saturation from $S_g = 0.666$ to $S_g = 0.566$. Consequently the relative gas permeability decreases and the relative water permeability increases. The relative oil permeability, however, increases while the oil saturation remains constant. This is due to the fact that the oil is moved by the water to the larger pore radii and to the fact that the oil is pressed together (the range of pore radii filled by oil is smaller). This is shown in Figure 5.8.

Figure 5.13 shows the relative permeabilities for water, oil and gas as a function of the gas phase (the advancing phase) during secondary drainage, where gas displaces the oil phase and the oil phase displaces the water phase. The water saturation decreases until its previous value (from $S_w = 0.134$ until $S_w = 0.034$), the oil saturation remains 0.3 and the gas saturation increases from $S_g = 0.566$ until $S_g = 0.666$. The accompanying endpoint relative permeabilities, endpoint saturations and connate saturations are shown in Table 5.5. Once more, continuation of the relative permeabilities and saturations is preserved. As a consequence of secondary drainage, the relative water permeability decreases until zero (since the connate water saturation is reached) and the relative gas permeability increases by such a small amount that it is not visible in Figure 5.13, nor can it be seen in the three decimals in Table 5.5. The relative oil permeability, however, increases again. Due to the secondary drainage and secondary imbibition process, the oil is situated into a smaller range of pore radii and the accessible fraction in these pores has increased (see Figure 5.8 and 5.9). This is in agreement with the increasing mobility found in the numerical experiments (see Figure 5.3 and 5.4).

These results are valid for this specific iteration with these specific saturations, which are comparable with the conditions in the numerical experiments. Figure 5.8 and 5.9 and the accompanying relative permeabilities would be significantly different if for example the increase of the water saturation during secondary imbibition would be much higher. In this case, we have chosen to start the water infiltration from a situation where water

is at the connate water saturation (see Figure 5.8). Increasing this initial water saturation gives the same results for the relative oil permeability, since the oil will again be displaced to larger pore radii and will be pressed together.

5.7 Conclusions

Numerical experiments have shown that temporary water infiltration into an oil lens increases the mobility of the oil. Both upwards and downwards water infiltration reveal this effect. To obtain more insight into this feature, we used percolation theory to describe the problem qualitatively. From the comparison between these two techniques we can conclude the following: both numerically and analytically the mobility of oil increases after temporary water infiltration. Furthermore, percolation theory shows that the oil is divided over a broader pore size range. More pores where oil is present will enhance the continuous path and therefore the mobility.

    Upwards water infiltration increase the mobility even more than downwards water infiltration. Since percolation theory calculates the average permeabilities for a chosen volume of interest, it is not possible to explain the difference between these two types of water infiltration. This should be found in the gravitational forces.

Appendix 5A

Equations used for the analytical solution

For the primary drainage equations, we refer to Chapter 4

Primary imbibition (see Figure 5.7.a and Figure 5.7.b)

The main characterization is now to include all pores with $R_d^{end} < R < R_i$ by oil, where R_i is always smaller than the connate gas radius R_{gc}. The allowability ($Q_{o,i}$ and $\psi_{o,i}^a(R)$) and occupancy equations ($X_{o,i}$ and $\psi_{o,i}^O(R)$) for oil during imbibition are:

$$Q_{o,i} = \int_{R_d^{end}}^{R_i} \psi(R)dR \tag{5.1}$$

$$X_{o,i}^O = X^A(Q_{o,i}) \tag{5.2}$$

$$\psi_{o,i}^O(R) = \begin{cases} 0 & , R_{\min} < R \leqslant R_d^{end} \\ \dfrac{\psi(R)}{X_{o,i}^A} \dfrac{X_{o,i}^A(Q_{o,i})}{Q_{o,i}} & , R_d^{end} < R \leqslant R_i \\ 0 & , R_i < R < R_{\max} \end{cases} \qquad (5.3)$$

where the subscript o denotes the oil phase. The occupancy statistics for oil are obtained by defining the pores with $R_d^{end} \leqslant R < R_i$ that formerly contained gas, in the proportion $\dfrac{X^A(Q_{o,i})}{Q_{o,i}}$ that they come to be occupied by oil.

The gas phase previously filled the radii between R_d^{end} and $R_{\max}$, while the radii between R_d^{end} and R_i are now allowed to be filled by oil. The allowability and occupancy equations for gas are:

$$Q_{g,i} = X_{g,i}^O = \int_{R_d^{end}}^{R_{\max}} \psi(R)dR - \frac{X^A(Q_{o,i})}{Q_{o,i}} \int_{R_d^{end}}^{R_i} \psi(R)dR \qquad (5.4)$$

$$\psi_{g,i}^O(R) = \begin{cases} 0 & , R_{\min} < R < R_d^{end} \\ \dfrac{\psi(R)}{X_{g,i}^O}\left[1 - \dfrac{X^A(Q_{o,i})}{Q_{o,i}}\right] & , R_d^{end} \leqslant R < R_i \\ \dfrac{\psi(R)}{X_{g,i}^O} & , R_i \leqslant R < R_{\max} \end{cases} \qquad (5.5)$$

This process can continue until the oil displacement stops at $R = R_i^*$ (see Figure 5.7.b), where R_i^* is smaller than the connate gas radius R_i^{end}. This radius is determined from the oil saturation (S_o) that we have chosen to enter the domain:

$$S_o = \frac{\dfrac{X^A(Q_{o,i})}{Q_{o,i}} \int_{R_d^{end}}^{R_i^*} \psi(R)v(R)dR}{\int_{R_{\min}}^{R_{\max}} \psi(R)v(R)dR} \qquad (5.6)$$

Secondary imbibition (see Figure 5.8.a and Figure 5.8.b)

The allowability equation for water is:

$$Q_{w,i2} = \int_{R_{\min}}^{R_{i2,w}} \psi(R)dR \qquad (5.7)$$

The occupancy equations for water are:

$$X_{w,i2}^O = \int_{R_{\min}}^{R_d^{end}} \psi(R)dR + \frac{X^A(Q_{w,i2}, X_{w,d}^{O,end})}{Q_{w,i2}} \int_{R_d^{end}}^{R_{i2,w}} \psi(R)dR \qquad (5.8)$$

$$\psi_{w,i2}^O(R) = \begin{cases} \frac{\psi(R)}{X_{w,i2}^O} & , R_{\min} < R < R_d^{end} \\ \frac{\psi(R)}{X_{w,i2}^O} \frac{X^A(Q_{w,i2}, X_{w,d}^{O,end})}{Q_{w,i2}} & , R_d^{end} \leqslant R < R_{i2,w} \\ 0 & , R_{i2,w} < R < R_{\max} \end{cases} \quad (5.9)$$

The radii that are allowed for oil are those radii that were occupied at the end of the primary imbibition, i.e. part of the radii between R_d^{end} and R_i^*, minus the radii (between R_d^{end} and R_{i2}) that have become allowed for water. The allowability and occupancy equations for oil are:

$$\begin{aligned} Q_{o,i2} &= \int_{R_d^{end}}^{R_{i2,w}} \psi(R) dR [1 - \frac{X^A(Q_{w,i2})}{Q_{w,i2}}] \\ &\quad + \int_{R_{i2,w}}^{R_{i2,o}} \psi(R) dR \end{aligned} \quad (5.10)$$

$$\begin{aligned} X_{o,i2}^O &= \frac{X^A(Q_{o,i2})}{Q_{o,i2}} \int_{R_d^{end}}^{R_{i2,w}} \psi(R) dR [1 - \frac{X^A(Q_{w,i2})}{Q_{w,i2}}] \\ &\quad + \frac{X^A(Q_{o,i2})}{Q_{o,i2}} \int_{R_{i2,w}}^{R_{i2,o}} \psi(R) dR \end{aligned} \quad (5.11)$$

$$\psi_{o,i2}^O(R) = \begin{cases} 0 & , R_{\min} < R < R_d^{end} \\ \frac{\psi(R)}{Q_{o,i2}} \frac{X^A(Q_{o,i2})}{Q_{o,i2}} [1 - \frac{X^A(Q_{w,i2})}{Q_{w,i2}}] & , R_d^{end} \leqslant R < R_{i2,w} \\ \frac{\psi(R)}{Q_{o,i2}} \frac{X^A(Q_{o,i2})}{Q_{o,i2}} & , R_{i2,w} < R < R_{i2,o} \\ 0 & , R_{i2,o} < R < R_{\max} \end{cases} \quad (5.12)$$

Since gas is not immobile during primary imbibition, the allowability and occupancy equations for gas must be added to the equations that describe the primary imbibition process. In the pores where three phases are present (between R_d^{end} and $R_{i2,w}$) we add the water and oil phase to be the wetting phase that displaces the gas phase. In the radii between $R_{i2,w}$ and $R_{i2,o}$ the oil phase solely displaces the gas phase.

$$Q_{g,i2} \;=\; X_{g,i2}^{O} = \int_{R_d^{end}}^{R_{i2,w}} \psi(R)dR[1\text{-}\frac{X^A(Q_{w,i2}+Q_{o,i2})}{Q_{w,i2}+Q_{o,i2}}]$$

$$+ \int_{R_{i2,w}}^{R_{i2,o}} \psi(R)dR[1\text{-}\frac{X^A(Q_{o,i2})}{Q_{o,i2}}] + \int_{R_{i2,o}}^{R_{max}} \psi(R)dR \quad (5.13)$$

$$\psi_{g,i2}^{O} = \begin{cases} 0 & , R_{min} < R \leqslant R_d^{end} \\ \frac{\psi(R)}{Q_{g,i2}}[1\text{-}\frac{X^A(Q_{w,i2}+Q_{o,i2})}{Q_{w,i2}+Q_{o,i2}}] & , R_d^{end} < R \leqslant R_{i2,w} \\ \frac{\psi(R)}{Q_{g,i2}}[1\text{-}\frac{X^A(Q_{o,i2})}{Q_{o,i2}}] & , R_{i2,w} < R \leqslant R_{i2,o} \\ \frac{\psi(R)}{Q_{g,i2}} & , R_{i2,o} < R < R_{max} \end{cases} \quad (5.14)$$

This process continues until a certain water saturation has entered the domain at $R_{i2,w}^{*}$ (see Figure 5.8). The values for $R_{i2,w}^{*}$ and $R_{i2,o}^{*}$ can be calculated from the water saturation (S_w) and the oil saturation (S_o):

$$S_w = \frac{\int_{R_{min}}^{R_d^{end}} \psi(R)v(R)dR + \frac{X^A(Q_{w,i2})}{Q_{w,i2}} \int_{R_d^{end}}^{R_{iw,o}^{*}} \psi(R)v(R)dR}{\int_{R_{min}}^{R_{max}} \psi(R)v(R)dR} \quad (5.15)$$

$$S_o = \frac{\int_{R_{min}}^{R_d^{end}} \psi(R)v(R)dR + \frac{X^A(Q_{w,i2})}{Q_{w,i2}} \int_{R_d^{end}}^{R_{i2,o}^{*}} \psi(R)v(R)dR}{\int_{R_{min}}^{R_{max}} \psi(R)v(R)dR}\text{-}S_w \quad (5.16)$$

The water saturation consists of the volume that is occupied by water ($X_{w,i2}^{O}$) divided by the total volume. Furthermore the oil saturation is calculated by dividing the volume occupied by water and oil by the total volume and substracting the known value for the water saturation. From these equations the radii $R_{i2,w}^{*}$ and $R_{i2,o}^{*}$ can be calculated.

Secondary drainage (see Figure 5.9)

The allowability equation for gas is:

$$Q_{g,d2} \;=\; \int_{R_d^{end}}^{R_{i2,w}^{*}} \psi(R)dR[1\text{-}\frac{X^A(Q_{w,i2}^{end}+Q_{o,i2}^{end})}{Q_{w,i2}^{end}+Q_{o,i2}^{end}}] +$$

$$\int_{R_{i2,w}^{*}}^{R_{d2,g}} \psi(R)dR[1\text{-}\frac{X^A(Q_{o,i2}^{end})}{Q_{o,i2}^{end}}] + \int_{R_{d2,g}}^{R_{max}} \psi(R)dR \quad (5.17)$$

The occupancy equations for gas are the occupancy equations for gas after secondary imbibition plus the part that becomes allowed (between $R_{d2,o}$ and $R^*_{i2,o}$) times the accessibility fraction.

$$
\begin{aligned}
X^O_{g,d2} &= \int_{R^{end}_d}^{R^*_{i2,w}} \psi(R)dR[1\text{-}\frac{X^A(Q^{end}_{w,i2}+Q^{end}_{o,i2})}{Q^{end}_{w,i2}+Q^{end}_{o,i2}}] + \int_{R^*_{i2,w}}^{R_{d2,g}} \psi(R)dR \\
&\quad \cdot[1\text{-}\frac{X^A(Q^{end}_{o,i2})}{Q^{end}_{o,i2}}] + \frac{X^A(Q_{g,d2})}{Q_{g,d2}} \int_{R_{d2,g}}^{R^*_{i2,o}} \psi(R)dR \\
&\quad + \int_{R^*_{i2,o}}^{R_{\max}} \psi(R)dR
\end{aligned}
\tag{5.18}
$$

$$
\psi^O_{g,d2}(R) = \begin{cases}
0 & , R_{\min} < R \leqslant R^{end}_d \\
\frac{\psi(R)}{Q_{g,d2}}[1\text{-}\frac{X^A(Q^{end}_{w,i2}+Q^{end}_{o,i2})}{Q^{end}_{w,i2}+Q^{end}_{o,i2}}] & , R^{end}_d < R \leqslant R^*_{i2,w} \\
\frac{\psi(R)}{Q_{g,d2}}[1\text{-}\frac{X^A(Q^{end}_{o,i2})}{Q^{end}_{o,i2}}] & , R^*_{i2,w} < R \leqslant R_{d2,g} \\
\frac{\psi(R)}{Q_{g,d2}} \frac{X^A(Q_{g,d2})}{Q_{g,d2}} & , R_{d2,g} \leqslant R < R^*_{i2,o} \\
\frac{\psi(R)}{Q_{g,d2}} & , R^*_{i2,o} \leqslant R < R_{\max}
\end{cases}
\tag{5.19}
$$

The allowability equations for oil consist of the part that was occupied by oil after secondary imbibition plus the part where oil is displacing water (between $R_{d2,w}$ and $R^*_{i2,w}$) minus the part where gas is displacing oil (between $R_{d2,o}$ and $R^*_{i2,o}$).

$$
\begin{aligned}
Q_{o,d2} &= \frac{X^A(Q^{end}_{o,i2})}{Q^{end}_{o,i2}} \int_{R^{end}_d}^{R_{d2,o}} \psi(R)dR[1\text{-}\frac{X^A(Q^{end}_{w,i2})}{Q^{end}_{w,i2}}] + \int_{R_{d2,o}}^{R^*_{i2,w}} \psi(R)dR \\
&\quad + \frac{X^A(Q^{end}_{o,i2})}{Q^{end}_{o,i2}} \int_{R^*_{i2,w}}^{R_{d2,g}} \psi(R)dR \\
&\quad + \int_{R_{d2,o}}^{R^*_{i2,o}} \psi(R)dR[1\text{-}\frac{X^A(Q_{g,d2})}{Q_{g,d2}}]
\end{aligned}
\tag{5.20}
$$

Since $Q_{o,d2}$ and $Q_{g,d2}$ contain linking formulations ($Q_{o,d2}$ uses $Q_{g,d2}$ in its calculation and vice versa), we use the mass balance of the domain to calculate $\frac{X^A(Q_{g,d2})}{Q_{g,d2}}$ in a different way. The decrease of S_w is identical to the increase of S_g since S_o remains constant:

$$\Delta S_w = \frac{X^A(Q_{w,i2}^{end})}{Q_{w,i2}^{end}} \frac{\int_{R_{d2,o}}^{R_{i2,w}^*} \psi(R)v(R)dR}{\int_{R_{\min}}^{R_{\max}} \psi(R)v(R)dR} \tag{5.21}$$

$$\Delta S_g = [\frac{X^A(Q_{o,i2}^{end})}{Q_{o,i2}^{end}} \frac{X^A(Q_{g,d2})}{Q_{g,d2}}] \frac{\int_{R_{d2,g}}^{R_{i2,o}^*} \psi(R)v(R)dR}{\int_{R_{\min}}^{R_{\max}} \psi(R)v(R)dR} \tag{5.22}$$

From these two equations we can calculate:

$$\frac{X^A(Q_{g,d2})}{Q_{g,d2}} = [\frac{X^A(Q_{w,i2}^{end})}{Q_{w,i2}^{end}} \frac{Q_{o,i2}^{end}}{X^A(Q_{o,i2}^{end})}] \frac{\int_{R_{d2,o}}^{R_{i2,w}^*} \psi(R)v(R)dR}{\int_{R_{d2,g}}^{R_{i2,o}^*} \psi(R)v(R)dR} \tag{5.23}$$

which can be used in Equation 5.20 to calculate $Q_{o,d2}$ and subsequently Equation 5.17 can be calculated.

$$\begin{aligned}
X_{o,d2}^O &= \frac{X^A(Q_{o,i2}^{end})}{Q_{o,i2}^{end}} \int_{R_d^{end}}^{R_{d2,o}} \psi(R)dR[1\text{-}\frac{X^A(Q_{w,i2}^{end})}{Q_{w,i2}^{end}}] + \\
&\quad \frac{X^A(Q_{o,d2})}{Q_{o,d2}} \int_{R_{d2,o}}^{R_{i2,w}^*} \psi(R)dR + \frac{X^A(Q_{o,i2}^{end})}{Q_{o,i2}^{end}} \int_{R_{i2,w}^*}^{R_{d2,g}} \psi(R)dR + \\
&\quad \int_{R_{d2,o}}^{R_{i2,o}^*} \psi(R)dR[1\text{-}\frac{X^A(Q_{g,d2})}{Q_{g,d2}}]
\end{aligned} \tag{5.24}$$

$$\psi_{o,d2}^O(R) = \begin{cases} 0 & , R_{\min} < R \leqslant R_d^{end} \\ \frac{\psi(R)}{Q_{o,d2}} \frac{X^A(Q_{o,i2}^{end})}{Q_{o,i2}^{end}}[1\text{-}\frac{X^A(Q_{w,i2}^{end})}{Q_{w,i2}^{end}}] & , R_d^{end} < R \leqslant R_{d2,o} \\ \frac{\psi(R)}{Q_{o,d2}} \frac{X^A(Q_{o,d2})}{Q_{o,d2}} & , R_{d2,o} < R \leqslant R_{i2,w}^* \\ \frac{\psi(R)}{Q_{o,d2}} \frac{X^A(Q_{o,i2}^{end})}{Q_{o,i2}^{end}} & , R_{i2,w}^* < R \leqslant R_{d2,g} \\ \frac{\psi(R)}{Q_{o,d2}}[1\text{-}\frac{X^A(Q_{g,d2})}{Q_{g,d2}}] & , R_{d2,g} < R \leqslant R_{i2,o}^* \\ 0 & , R_{i2,o}^* \leqslant R < R_{\max} \end{cases} \tag{5.25}$$

The allowability equations for water are the radii that were filled with water after secondary imbibition (between $R_{\min}$ and $R_{i2,w}^*$) minus the radii where water is displaced by gas (between $R_{d2,w}$ and $R_{i2,w}^*$):

$$Q_{w,d2} = X_{w,d2}^O = \int_{R_{\min}}^{R_d^{end}} \psi(R)dR + \frac{X^A(Q_{w,i2}^{end})}{Q_{w,i2}^{end}} \int_{R_d^{end}}^{R_{d2,o}} \psi(R)dR$$

$$+ \frac{X^A(Q_{w,i2}^{end})}{Q_{w,i2}^{end}} \int_{R_{d2,o}}^{R_{i2,w}^*} \psi(R)dR(1 - \frac{X^A(Q_{o,d2})}{Q_{o,d2}}) \tag{5.26}$$

$$\psi_{w,d2}^O(R) = \begin{cases} \frac{\psi(R)}{Q_{w,d2}} & , R_{\min} < R \leqslant R_d^{end} \\ \frac{\psi(R)}{Q_{w,d2}} \frac{X^A(Q_{w,i2}^{end})}{Q_{w,i2}^{end}} & , R_d^{end} < R \leqslant R_{d2,o} \\ \frac{\psi(R)}{Q_{w,d2}} \frac{X^A(Q_{w,i2}^{end})}{Q_{w,i2}^{end}}(1 - \frac{X^A(Q_{o,d2})}{Q_{o,d2}}) & , R_{d2,o} < R \leqslant R_{i2,w}^* \\ 0 & , R_{i2,w}^* < R < R_{\max} \end{cases} \tag{5.27}$$

This process continues until the water saturation is decreased until a certain level and from this water saturation and from the gas saturation we can calculate the accompanying radii $R_{d2,o}^*$ and $R_{d2,g}^*$:

$$S_w = \{\int_{R_{\min}}^{R_d^{end}} \psi(R)v(R)dR + \frac{X^A(Q_{w,i2}^{end})}{Q_{w,i2}^{end}} \int_{R_d^{end}}^{R_{d2,o}^*} \psi(R)v(R)dR +$$

$$\frac{X^A(Q_{w,i2}^{end})}{Q_{w,i2}^{end}} \int_{R_{d2,o}^*}^{R_{i2,w}^*} \psi(R)dR(1 - \frac{X^A(Q_{o,d2})}{Q_{o,d2}})\}$$

$$/ \int_{R_{\min}}^{R_{\max}} \psi(R)v(R)dR \tag{5.28}$$

$$S_g = ([1 - (\frac{X^A(Q_{o,i2}^{end}) + X^A(Q_{w,i2}^{end})}{Q_{o,i2}^{end} + Q_{w,i2}^{end})})] \int_{R_d^{end}}^{R_{d2,g}^*} \psi(R)v(R)dR +$$

$$\{[1 - (\frac{X^A(Q_{o,i2}^{end}) + X^A(Q_{w,i2}^{end})}{Q_{o,i2}^{end} + Q_{w,i2}^{end})})] \frac{X^A(Q_{g,d2})}{Q_{g,d2}}\} \int_{R_{d2,g}^*}^{R_{i2,o}^*} \psi(R)v(R)dR)$$

$$/ \int_{R_{\min}}^{R_{\max}} \psi(R)v(R)dR \tag{5.29}$$

Notation

k_{ri} relative permeability of phase i

k'_{ri} end point relative permeability of phase i
Q_j allowed fraction for phase j
Q_c critical fraction= percolation threshold
R radius of a bond $[m]$
S saturation
t time (hrs)
v volume of a bond $[m^2]$
W_f free oil volume per unit lateral area [m]
X fraction of the bonds that is accessible/occupied
x horizontal coordinate [cm]
Z average number of bonds that originate from one node
z vertical coordinate [cm]
ϕ porosity
$\psi(R)$ number fraction function

Subscripts

d drainage
$d2$ secondary drainage
g gas
gc connate gas
i imbibition
$i2$ secondary imbibition
max maximum
min minimum
o oil
of free oil
or residual oil
w water
wc connate water

Superscripts

$*$ end situation of a process
A accessible
end limiting end situation of a process
ini initial
O occupied

Samenvatting

Sinds de jaren zeventig in de vorige eeuw zijn er in Nederland op grote schaal NAPL verontreinigingen in de bodem aangetroffen die het gevolg zijn van onzorgvuldig handelen of onwetendheid. NAPL's (Non-Aqueous Phase Liquids) zijn organische vloeistoffen die nauwelijks mengen met water. Dit type verontreiniging wordt ook wel 'olie' verontreiniging genoemd. De effecten van NAPL's op de drinkwater kwaliteit en dus op de gezondheid van de mens zijn van dien aard dat deze verontreinigingen zo efficiënt mogelijk opgeruimd dienen te worden. De impact van een NAPL op drinkwaterkwaliteit blijkt uit het feit dat 1 liter olie 100.000 liter grondwater dat bedoeld is voor de bereiding van drinkwater zodanig kan vervuilen dat het vanwege gezondheidsredenen niet meer gebruikt kan worden.

Wij hebben ons gericht op olieverontreiniging die lichter is dan water en dus op het freatische vlak blijft drijven. Dit type olie wordt L(ight)NAPL genoemd. De uitgangssituatie waar LNAPL zich boven een statisch freatisch vlak bevindt, is uitgebreid onderzocht en deze situatie kunnen we inmiddels vrij goed begrijpen en modelleren. Echter, in werkelijkheid is het freatisch niveau niet statisch en veroorzaken fysische verschijnselen zoals seizoensfluctuaties in grondwater standen, het afpompen van grondwater en regenval een fluctuerend freatisch vlak. Tot op heden is er weinig bekend over de gevolgen van deze verschijnselen op het fysische gedrag van LNAPL in de bodem. Wij vestigen de aandacht op dergelijke fysische processen en hun invloed op zowel de geometrie van de olielens als de verdeling van water, olie en lucht in de poriën van de bodem. In het vervolg gebruiken we de term 'olie' in plaats van 'LNAPL'.

Olie kan als kleine druppeltjes worden ingesloten in de waterfase, zodat de oliefase immobiel wordt. Mobiele olie kan vrij eenvoudig verwijderd worden uit de bodem door middel van afpompen; het immobiele gedeelte van de olie blijft echter achter en kan nog steeds een bedreiging vormen voor het milieu doordat het verdampt of doordat het oplost in het grondwater.

Teneinde deze immobiele olie te verwijderen, worden andere zogenaamde
'in situ' sanerings technieken gebruikt. Om deze technieken zo efficient mo-
gelijk te gebruiken, is het noodzakelijk om onze kennis over de immobiliteit
van olie en de kwantificering ervan te vergroten.

Wij hebben twee situaties bekeken waarbij water infiltreert in de olielens
waarbij een dynamisch freatisch vlak wordt gecreëerd: 1. Een fluctuerend
waterniveau, waarbij de waterdruk op een bepaald niveau onder de olie-
lens een sinusoïdale functie heeft, zodat water van onderaf infiltreert in de
olielens. Dit zou in de realiteit veroorzaakt kunnen worden door seizoens-
fluctuaties in grondwater standen. 2. Waterinfiltratie van bovenaf, waarbij
water aan de bovenkant van het domein wordt geïnjecteerd. De waterdruk
op een bepaald niveau onder de olielens blijft constant zodat het water
door de lens zal gaan. Dit zou in de realiteit regenwater kunnen zijn, dat
infiltreert in de bodem.

Hoofdstuk 2 en 3 beschrijven het gedrag van olie onder invloed van een
fluctuerend waterniveau. Numerieke berekeningen in een homogeen twee-
dimensionaal domein tonen aan, dat een fluctuerend waterniveau resulteert
in vertraging van de horizontale spreiding van de olie op het freatische vlak.
Stijging van het waterniveau immobiliseert de olie en daardoor kan de olie
niet meer horizontaal spreiden. Bij de daarop volgende verlaging van het
water niveau mobiliseert de olie weer zodat de horizontale spreiding van
olie weer kan continueren. Deze vertraging is verdisconteerd door een 'stro-
mingstijd' te definiëren die aangeeft gedurende welk deel van de totale tijd
de olie daadwerkelijk mobiel is en kan spreiden. Een bestaande analytische
oplossing voor olie spreiding op een statisch freatisch vlak kan door ge-
bruik van deze stromingstijd ook gebruikt worden voor een fluctuerend wa-
terniveau, wat aanzienlijk minder computer rekentijd kost dan numerieke
berekeningen. Aanvullend zijn er tweedimensionale experimenten in het
laboratorium uitgevoerd, waaruit bleek dat het vrijwel onmogelijk is om
een homogeen domein te creëeren. De ontstane heterogeniteiten vormen
een capillaire barriére waarboven water accumuleert. Ter compensatie van
deze waterlenzen in de onverzadigde zone, is in de numerieke berekenin-
gen de waterdruk aan de onderkant van het domein verhoogd. Vervolgens
bleek na vergelijking met de experimentele resultaten, dat de numerieke en
analytische oplossingen de belangrijkste verschijnselen accuraat weergeven.

Hoofdstuk 4 en 5 beschrijven het effect van waterpercolatie op de verde-
ling van de verschillende fasen in de poriën. De methode die daarvoor ge-
bruikt wordt is de percolatie theorie. De effecten van percolatie van wa-

ter door de olielens op de mobiliteit van olie zijn eerst numeriek bekeken, waaruit bleek dat na de waterpercolatie, op het moment dat de situatie stabiel is geworden, de mobiliteit van de olie is toegenomen. Beide types water infiltratie (van bovenaf en onderaf) vertonen dit effect. Om meer inzicht te krijgen in de processen die zich afspelen tijdens de waterpercolatie hebben we percolatie theorie gebruikt. Deze theorie beschrijft op porieschaal de verbindbaarheid van de vloeistoffen/gassen die aanwezig zijn. Statistisch wordt de kans beschreven dat een porie toegankelijk is voor een bepaalde vloeistof. Tot nu toe werd deze theorie hoofdzakelijk voor 2-fasen systemen (olie en water) gebruikt en was de uitwerking naar een 3-fasen systeem (olie, water en lucht) nog beperkt. Wij hebben de percolatie theorie voor een 3-fasen systeem uitgewerkt en toegepast op de twee types waterpercolatie. De analytische resultaten bevestigen de numerieke resultaten dat de mobilisatie van olie toeneemt na waterinfiltratie van beide types. De reden hiervoor is, dat de olie gedurende water infiltratie verplaatst wordt naar een groter aantal poriën, wat de connectiviteit bevordert. Met deze kennis is het nu mogelijk om een olielens met behulp van waterinfiltratie zodanig te manipuleren dat de mobiliteit wordt bevorderd.

130

Nawoord

Op deze plaats wil ik een aantal mensen bedanken wiens hulp, inspiratie en steun hebben bijgedragen aan het tot stand komen van dit proefschrift. In de eerste plaats wil ik mijn promotor en dagelijks begeleider Sjoerd van der Zee bedanken voor zijn ondersteuning en voor de enorme hulp bij het schrijven van mijn artikelen. Ik wil Alies Bartelds bedanken voor haar hulp bij de hoofdstukken over percolatie theorie. Alies, jij was meteen enthousiast over mijn idee deze theorie te gebruiken en je positieve reacties waren in moeilijke tijden een enorme steun voor mij. Via e-mail, fax en telefoon bleek de communicatie uitstekend te gaan. Hans Bruining bracht mij op het idee om met percolatie theorie aan het werk te gaan. Hans, bedankt voor je enthousiasme, bemoedigende woorden en het corrigeren van mijn werk. Rink van Dijke, bedankt voor je waardevolle commentaar op de hoofdstukken over percolatie theorie. Mart Oostrom wil ik bedanken voor het beschikbaar stellen van de code van het numerieke programma STOMP waar een groot deel van mijn werk mee berekend is en voor het opsturen van de updates en nieuwe handleidingen. Bob Lenhard, thank you for sending me the fluctuation data. Ik bedank Gijs Breedveld en Marianne Ness voor de samenwerking waarvan het experimentele werk het resultaat is.

Ik heb het enorm naar mijn zin gehad in Wageningen en daarom wil ik al mijn collega's van de sectie bodemkwaliteit bedanken. Vooral de collega's in de kelder zijn altijd een motivatie geweest om elke dag van Utrecht naar Wageningen te rijden: bedankt voor de gezellige lunches, koffiepauzes, zeilweekenden, borrels etc.. Twee personen wil ik nog speciaal noemen. Ten eerste Louise Wipfler. Bijna 5 jaar lang hebben we een kamer gedeeld, een paar jaar gecarpooled, reisjes naar Italië, Oslo, Boston en New York gemaakt. Ik heb dat als zeer prettig ervaren: je was altijd aanwezig voor inhoudelijke vragen, om te brainstormen, om mijn hart te luchten en natuurlijk voor de gezelligheid. Ten tweede Anke Wolthoorn: bedankt

132

voor je steun, de gezelligheid en voor het corrigeren van mijn nederlandse teksten. Ik hoop dat we elkaar ook in de toekomst vaak blijven zien!

Op deze plaats wil ik Dr. Hené bedanken omdat hij voor mij de medische wetenschap vertegenwoordigt, die het voor mij mogelijk heeft gemaakt om dit te kunnen bereiken. Bovendien was het ook heel erg motiverend dat hij altijd bijzonder veel belangstelling voor mijn studie en later voor mijn promotie heeft getoond.

Nelleke, Cor en Matthijs: bedankt voor jullie belangstelling en vriendschap! Tenslotte wil ik mijn zus Ester bedanken voor het vele lezen en corrigeren van mijn teksten en voor het plezier in het samen cursussen volgen. Mijn vader en moeder bedank ik voor hun altijd aanwezige steun en belangstelling. Ernst, dankjewel voor je enorme steun en voor je kritische vragen die mij altijd weer met twee benen op de grond zetten.

Annemieke

Curriculum Vitae

Annemieke Marsman werd op 25 augustus 1972 geboren te Amsterdam. In 1990 behaalde zij het gymnasium β diploma aan het Mill Hill College te Goirle. Van 1990 tot 1997 volgde zij de studie geofysica aan de faculteit Aardwetenschappen van de Universiteit Utrecht. De specialisaties waren tektonofysica en theoretische geofysica, het keuzeblok was seismologie. Tijdens haar afstuderen deed zij onderzoek naar methoden om de doorbuiging van de lithosfeer te simuleren. In 1997 studeerde zij af bij de vakgroep tektonofysica.

Van 1997 tot 2002 was zij als assistent in opleiding werkzaam aan Wageningen Universiteit bij de sectie Bodemkwaliteit. Hier deed zij onderzoek naar het effect van fysische verschijnselen op het gedrag van olie verontreinigingen. De belangrijkste resultaten staan in dit proefschrift beschreven.

Bibliography

[1] Abriola L.M. and Pinder G.F.: 1986, 'A multiphase approach to the modeling of porous media contamination by organic compounds, 1. equation development'. *Water Resour. Res.* **21**, 11–18.

[2] Barenblatt G.I.: 1985, *Similarity, self-similarity and intermediate asymptotics.* Consultants Bureau-New York and London.

[3] Bartelds G.A.: 1998, 'The influence of inaccessible and excluded pore volume on polymer flooding'. Ph.D. thesis, Technical University of Delft.

[4] Bartelds G.A., Bruining J. and Molenaar J.: 1997, 'The modeling of velocity enhancement in polymer flooding'. *Transport in Porous Media* **26**, 75–88.

[5] Bear J.: 1972, *Dynamics of fluids in porous media.* Elsevier.

[6] Brooks R.H. and Corey A.T.: 1966, 'Properties of porous media affecting fluid flow'. *J. of Irrigation and Drainage Division* **93(3)**, 61–88.

[7] Cary J.W., McBride J.F. and Simmons C.S.: 1989, 'Observation of water and oil infiltration into soil: Some simulation challenges'. *Water Resour. Res.* **25(1)**, 73–80.

[8] Eckberg D.K. and Sunada D.K.: 1984, 'Nonsteady three-phase immiscible fluid distribution in porous media'. *Water Resour. Res.* **20(2)**, 1891–1897.

[9] Essaid H.I., Herkelrath W.N. and Hess K.M.: 1993, 'Simulation of fluid distributions observed at a crude oil spill site incorporating hysteresis, oil entrapment, and spatial variability of hydraulic properties'. *Water Resour. Res.* **29(6)**, 1753–1770.

[10] Fisher M.E. and Essam J.W.: 1961, 'Some cluster size and percolation problems'. *J. of Math. Phys.* **2**, 609–619.

[11] Glass R.J., Steenhuis T.S. and Parlange J-Y.: 1989, 'Wetting front instability 2. experimental determination of relationships between system parameters and two-dimensional unstable flow field behavior in initially dry porous media'. *Water Resour. Res.* **25(6)**, 1195–1207.

[12] Hamby D.M.: 1996, 'Site remediation technique supporting environmental restoration activities - a review'. *Sci. Total Environ.* **191**, 203–224.

[13] Heiba A.A.: 1985, 'Porous Media: Fluid distributions and transport with applications to Petroleum recovery'. Ph.D. thesis, University of Minnesota.

[14] Heiba A.A., Davis H.T. and Scriven L.E.: 1984, 'Statistical network theory of three-phase relative permeabilities'. *SPE* **12690**, 121–129.

[15] Heiba A.A., Sahimi M., Scriven L.E. and Davis H.T.: 1992, 'Percolation theory of two-phase relative permeability'. *SPE* **11015**, 123–132.

[16] Host-Madsen J. and Jensen H.K.: 1992, 'Laboratory and numerical investigations of immiscible flow in soil'. *J. Hydrol.* **135**, 13–52.

[17] Hulshof J. and Vazquez J.L.: 1994, 'Self-similar solutions of the second kind for the modified porous medium equation'. *Euro. Jnl. of Applied Mathematics* **5**, 391–403.

[18] Kaluarachchi J.J. and Parker J.C.: 1992, 'Multiphase flow with a simplified model for oil entrapment'. *Transport in Porous Media* **7**, 1–14.

[19] Kirkpatrick S.: 1973, 'Percolation and conduction'. *Rev. of Modern Physics.* **45(4)**, 574–588.

[20] Kool J.B., Parker J.C. and Van Genuchten M.Th.: 1985, 'Determining soil hydraulic properties from one-step outflow experiments by parameter estimation: I. Theory and numerical studies'. *Soil. Sci. Soc. Am. J.* **49**, 1348–1354.

[21] Larsen J.K., Bech N. and Winter A.: 2000, 'Three-phase immiscible WAG injection: micromodel experiments and network models'. *SPE* **59324**, 1–6.

[22] Larson R.G., Davis H.T. and Scriven L.E.: 1981, 'Displacement of residual nonwetting fluid from porous media'. *Chem. Eng. Sci.* **36**, 75–85.

[23] Larson R.G., Scriven L.E. and Davis H.T.: 1977. *Nature* **268**, 409.

[24] Lenhard R.J. and Parker J.C.: 1987a, 'A model for hysteretic constitutive relations governing multiphase flow, 2. permeability-saturation relations'. *Water Resour. Res.* **23**, 2197–2206.

[25] Lenhard R.J. and Parker J.C.: 1987b, 'Measurement and prediction of saturation-pressure relationships in three-phase porous media'. *J. Contam. Hydrol.* **1**, 407–424.

[26] Lenhard R.J. and Parker J.C.: 1988, 'Experimental validation of the theory of extending two-phase saturation-pressure relations to three-fluid phase systems for monotonic drainage paths'. *Water Resour.Res.* **24**, 373–380.

[27] Lenhard R.J., Dane J.H., Parker J.C. and Kaluarachchi J.J.: 1988, 'Measurement and simulation of one-dimensional transient three-phase flow for monotonic liquid drainage'. *Water Resour. Res.* **24(6)**, 853–863.

[28] Lenhard R.J., Johnson T.G. and Parker J.C.: 1993, 'Experimental observations of nonaqueous-phase liquid subsurface movement'. *J. Contam. Hydrol.* **12**, 79–101.

[29] Lenhard R.J., Oostrom M. and White M.D.: 1995, 'Modeling fluid flow and transport in variably saturated porous media with the STOMP simulator. 2. Verification and validation exercises'. *Adv. Water Resources* **18(6)**, 365–373.

[30] Lenhard R.J., Parker J.C. and Kaluarachchi J.J.: 1989, 'A model for hysteretic constitutive relations governing multiphase flow 3. Refinements and numerical simulations'. *Water Resour. Res.* **25**, 1727–1736.

[31] Lenhard R.J., Parker J.C. and Kaluarachchi J.J.: 1991, 'Comparing simulated and experimental hysteretic two-phase transient fluid flow phenomena'. *Water Resour. Res.* **27(8)**, 2113–2124.

[32] Mani V. and Mohanty K.K.: 1998, 'Pore-level network modeling of three-phase capillary pressure and relative permeability curves'. *SPE* **50942**, 238–248.

[33] Pantazidou M. and Sitar N.: 1993, 'Emplacement of nonaqueous liquids in the vadose zone'. *Water Resour. Res.* **29(3)**, 705–722.

[34] Parker J.C. and Lenhard R.J.: 1987, 'A model for hysteretic constitutive relations governing multiphase flow. 1. Saturation-pressure relations'. *Water Resour. Res.* **23**, 2187–2196.

[35] Parker J.C. and Lenhard R.J.: 1990, 'Determining three-phase permeability-saturation-pressure relations from two phase system measurements'. *J. of Petroleum Science and Engineering* **4**, 57–65.

[36] Parker J.C., Lenhard R.J. and Kuppusamy T.: 1987, 'A parametric model for constitutive properties governing multiphase flow in porous media'. *Water Resour. Res.* **23**, 618–624.

[37] Ross B.: 1990, 'The diversion capacity of capillary barriers'. *Water Resour. Res.* **26(10)**, 2625–2629.

[38] Sahimi M.: 1993, 'Flow phenomena in rocks: from continuum models to fractels, percolation, cellular automata, and simulated annealing'. *Rev. of Modern Physics* **65(4)**, 1393–1534.

[39] Sahimi M.: 1994, *Applications of percolation theory.* Taylor & Francis.

[40] Sahimi M., Gavalas G.R. and Tsotsis T.T.: 1990, 'Statistical and continuum models of fluid-solid reactions in porous media'. *Chem. Eng. Sci.* **45**, 1443–1502.

[41] Stauffer D. and Aharony A.: 1985, *Introduction to percolation theory.* Taylor & Francis, second edition.

[42] Stinchcombe R.B.: 1974, 'Conductivity and spin-wave stiffness in disordered systems-an exactly soluble model'. *J. Phys. C: Solid State Phys.* **7**, 179–201.

[43] Van Dam J.C., Stricker J.N.M. and Droogers P.: 1994, 'Inverse method to determine soil hydraulic functions from multistep outflow experiments'. *Soil Sci. Soc. Am. J.* **56**, 1042–1050.

[44] Van Dijke M.I.J. and Van der Zee S.E.A.T.M.: 1997, 'A similarity solution for oil lens redistribution including capillary forces and oil entrapment'. *Transport in Porous Media* **29**, 99–125.

[45] Van Dijke M.I.J., Sorbie K.S. and McDougall S.R.: 2001, 'Saturation-dependencies of three-phase relative permeabilties in mixed-wet and fractionally wet systems'. *Adv. Water Resour.* **24**, 365–384.

[46] Van Geel P.J. and Sykes J.F.: 1994a, 'Laboratory and model simulations of an LNAPL spill in a variably-saturated sand, 1. Laboratory experiment and image analysis techniques'. *J. of Contam. Hydrol.* **17**, 1–25.

[47] Van Geel P.J. and Sykes J.F.: 1994b, 'Laboratory and model simulations of an LNAPL spill in a variably-saturated sand, 2. Comparison of laboratory and model results'. *J. of Contam. Hydrol.* **17**, 27–53.

[48] Van Geel P.J. and Sykes J.F.: 1997, 'The importance of fluid entrapment, saturation hysteresis and residual saturations on the distribution of a lighter-than-water non-aqueous phase liquid in a variably saturated sand medium'. *J. Contam. Hydrol.* **25**, 249–270.

[49] Van Genuchten M.T.: 1980, 'A closed form equation for predicting the hydraulic conductivity of unsaturated soils'. *Soil. Sci. Soc. Am. J.* **44**, 892–898.

[50] Van Lingen P.P., Barzanji O.H.M. and van Kruijsdijk C.P.J.W.: 1996, 'WAG injection to reduce capillary entrapment in small-scale heterogeneities'. *SPE* **36662**, 771–777.

[51] White M.D., Oostrom M. and Lenhard R.J.: 1995, 'Modeling fluid flow and transport in variably saturated porous media with the STOMP simulator.1. Nonvolatile three-phase model description'. *Adv. Water Resour.* **18**, 353–364.

[52] Wipfler E.L. and S.E.A.T.M. van der Zee: 2001, 'A set of constitutive relationships accounting for residual NAPL in the unsaturated zone'. *J. Contam. Hydrol.* **50**, 53–77.

[53] Wipfler E.L, Ness M., Breedveld G.D., Marsman A. and Van der Zee S.E.A.T.M., 'Infiltration and redistribution of LNAPL in unsaturated layered porous media'. *J. Contam. Hydrol.* accepted.

[54] Yortsos Y.C., Satik C., Bacri J.C. and Salin D.: 1993, 'Large-scale percolation theory of drainage'. *Transport in Porous Media* **10**, 171–195.